SANDIA REPORT
SAND2011-6939
Unlimited Release
Printed October, 2011

Rapid Hydrogen Gas Generation Using Reactive Thermal Decomposition of Uranium Hydride

Andrew D. Shugard, George M. Buffleben, Michael P. Kanouff, Scott C. James, David B. Robinson, Bernice E. Mills, Patricia E. Gharagozloo, Peter Van Blarigan

Prepared by
Sandia National Laboratories
Albuquerque, New Mexico 87185 and Livermore, California 94550

Sandia National Laboratories is a multi-program laboratory managed and operated by Sandia Corporation, a wholly owned subsidiary of Lockheed Martin Corporation, for the U.S. Department of Energy's National Nuclear Security Administration under contract DE-AC04-94AL85000.

Approved for public release; further dissemination unlimited.

Sandia National Laboratories

Issued by Sandia National Laboratories, operated for the United States Department of Energy by Sandia Corporation.

NOTICE: This report was prepared as an account of work sponsored by an agency of the United States Government. Neither the United States Government, nor any agency thereof, nor any of their employees, nor any of their contractors, subcontractors, or their employees, make any warranty, express or implied, or assume any legal liability or responsibility for the accuracy, completeness, or usefulness of any information, apparatus, product, or process disclosed, or represent that its use would not infringe privately owned rights. Reference herein to any specific commercial product, process, or service by trade name, trademark, manufacturer, or otherwise, does not necessarily constitute or imply its endorsement, recommendation, or favoring by the United States Government, any agency thereof, or any of their contractors or subcontractors. The views and opinions expressed herein do not necessarily state or reflect those of the United States Government, any agency thereof, or any of their contractors.

Printed in the United States of America. This report has been reproduced directly from the best available copy.

Available to DOE and DOE contractors from
U.S. Department of Energy
Office of Scientific and Technical Information
P.O. Box 62
Oak Ridge, TN 37831

Telephone: (865) 576-8401
Facsimile: (865) 576-5728
E-Mail: reports@adonis.osti.gov
Online ordering: http://www.osti.gov/bridge

Available to the public from
U.S. Department of Commerce
National Technical Information Service
5285 Port Royal Rd.
Springfield, VA 22161

Telephone: (800) 553-6847
Facsimile: (703) 605-6900
E-Mail: orders@ntis.fedworld.gov
Online order: http://www.ntis.gov/help/ordermethods.asp?loc=7-4-0#online

SAND2011-6939
Unlimited Release
Printed October, 2011

Rapid Hydrogen Gas Generation Using Reactive Thermal Decomposition of Uranium Hydride

Andrew D. Shugard
George M. Buffleben
Michael P. Kanouff
Scott C. James
David B. Robinson
Bernice E. Mills
Patricia E. Gharagozloo
Peter Van Blarigan

Sandia National Laboratories
P.O. Box 969
Livermore, California 94551

Abstract

Oxygen gas injection has been studied as one method for rapidly generating hydrogen gas from a uranium hydride storage system. Small scale reactors, 2.9 g UH_3, were used to study the process experimentally. Complimentary numerical simulations were used to better characterize and understand the strongly coupled chemical and thermal transport processes controlling hydrogen gas liberation. The results indicate that UH_3 and O_2 are sufficiently reactive to enable a well designed system to release gram quantities of hydrogen in ~ 2 seconds over a broad temperature range. The major system-design challenge appears to be heat management. In addition to the oxidation tests, H/D isotope exchange experiments were performed. The rate limiting step in the overall gas-to-particle exchange process was found to be hydrogen diffusion in the ~0.5 μm hydride particles. The experiments generated a set of high quality experimental data; from which effective intra-particle diffusion coefficients can be inferred.

ACKNOWLEDGMENTS

Ken Stewart (08222) graciously gave us the RGA system used for this work.

David Shimizu (08132) performed or assisted with the radiograph imaging shown in this work

Toff Garcia and Albert Sandoval (08517, radiation protection) were crucial to the completion of this work. They provided feedback on procedures and radiation control measures. In addition, they performed radiation/contamination surveys as requested or required.

This work was supported by the Laboratory Directed Research and Development (LDRD) and Advanced Simulation and Computing – Physics and Engineering Models (ASC-PEM) programs at Sandia National Laboratories.

CONTENTS

Acknowledgments 4

Contents 5

Figures 6

Tables 9

Nomenclature 10
- Variable 10
- Greek symbols 10
- Subscripts 10
- Superscripts 10

1 Introduction 11

2 Reactant selection and experimental apparatus design 13
- 2.1 Thermodynamic considerations 13
- 2.2 Prior work on the reactivity of UH_3 15
- 2.3 Reactant selection 16
- 2.4 Reactor and apparatus design 16
  - 2.4.1 Reactor 16
  - 2.4.2 Experiment apparatus 18

3 Numerical Simulations 27
- 3.1 Motivation 27
- 3.2 Model description 27
  - 3.2.1 Governing transport equations 27
  - 3.2.2 Chemical reactions 28
  - 3.2.3 Properties 31
  - 3.2.4 Permeability 31
  - 3.2.5 The finite element model 33

4 Experimental Results and Discussion 37
- 4.1 Experimental plan 37
- 4.2 Reactor #1 – slow O_2 injection 38
  - 4.2.1 Bed preparation 38
  - 4.2.2 O_2 injection-1 54
  - 4.2.3 O_2 injection-2 66
  - 4.2.4 O_2 injection-3 73
  - 4.2.5 Conclusions from reactor #1 81
- 4.3 Reactor #2 – fast O_2 injection at 30 °C 82
  - 4.3.1 Hydride/dehydride cycles 82
  - 4.3.2 O_2 injection-1 83
- 4.4 Reactor #3 – Fast O_2 injection at −80°C 87
  - 4.4.1 O_2 injection-1 88
- 4.5 Reactor #4 – HD exchange experiments 93
  - 4.5.1 Reactor #4 preparation 93

4.5.2 RGA calibration 93
4.5.3 Isotope exchange tests at 25, 100, 250°C. 95
5 Summary 101
6 References 103
Distribution 106

FIGURES

Figure 1: CAD model of the reactor. The bed is ϕ0.316 × 0.50 in^2 (0.803 × 1.27 cm^2) and contains about 2.9 g of UD_3. The void fraction is approximately 0.60. 17
Figure 2: An end-on view of reactor spacer showing the flow distribution pattern. 17
Figure 3: A reactor assembly. The AE F250C caps are replaced with Teledyne Taber pressure transducers when the reactor is connected to the experiment apparatus. 18
Figure 4: Experiment apparatus. The reactor is at the center of the system. The piston-driver is on the left and the product collection tank (receiver) is on the right. Volumes are listed in blue and pressure transducers, "P," are identified in green. The "T" symbol is a ϕ0.010 inch thermocouple that extends into the receiver tank. 18
Figure 5: A picture of the experiment manifold; before the residual gas analyzer system was added. 19
Figure 6: Cold-chamber in operation; the reactor temperature is about −40°C. 20
Figure 7: Cross-section view of the gas pre-conditioner. 20
Figure 8: Schematic of the crimped capillary interface. 21
Figure 9: RGA response times for H_2, D_2, and O_2. 22
Figure 10: Initial system configuration for reactor gas-mixing test. 23
Figure 11: RGA-derived mole fractions and receiver fill rate. The pink line indicates the time required to flush the He overpressure assuming perfect plug-flow in the reactor plumbing. 24
Figure 12: RGA-derived mole fractions during the back-mixing test. 25
Figure 13: An axisymmetric finite element model of the reactor. 34
Figure 14: Uranium pieces 30 minutes after cutting (left) and after 20 days of storage in a dry box (right). In the right photo, the pieces are inside a plastic bag. The pieces in the right photo weigh 2.84 g and were used in Reactor #1. The material's dark color is due to the surface oxide. 39
Figure 15: Reactor temperature and RGA partial pressures during Reactor 3 activation. 40
Figure 16: Hydride reaction progression for Reactor 1. The uranium reached D/U = 3 in approximately 1.2 hours. 41
Figure 17: Flow test data and DGM parameter plot for Reactor #1 after the initial hydride. The DGM parameter is calculated using the frit-corrected pressures just upstream and downstream from the porous bed. 43
Figure 18: Radiographs of reactors during processing. (a) Reactor #2 filled with two chunks of uranium metal. (b) Reactor #1 after the first hydride cycle. (c) Reactor #2 after dehydriding (between hydrides 6 and 7). (d) Reactor #1 after the second hydride cycle. 44
Figure 19: Effective DGM flow parameters for Reactors #1−4. Measured/predicted ratios of effective permeability (log-scale), molecular flow coefficient, and porosity/tortuosity ratio are shown. 47

Figure 20: RGA partial pressures and reactor temperature during the second dehydride cycle of Reactor #2. These data are representative of all dehydride cycles in all experiments..... 48
Figure 21: Hydride reaction progression for Reactor #1 during the second hydride; the uranium reached D/U = 2.96 in approximately 2 minutes. 49
Figure 22: SEM micrograph of 0.8 m^2/g uranium powder [14]. The specific surface area indicates that the sample likely underwent two hydride/dehydride cycles..... 50
Figure 23: SEM image of uranium hydride powder [5]. 51
Figure 24: SEM images of UT_3 powders [41]. Samples began as ~ 20-μm spherical uranium particles. Each row is at an equal magnification. The left column is UT_3 powder after 5 hydride/dehydride cycles; the right column is UT_3 powder after a single hydride cycle. 52
Figure 25: U and UH_3 BET surface area vs. hydride/dehydride cycles..... 53
Figure 26: Surface-mount thermocouple locations for injection 1. The orange square indicates the position of the UD_3 bed inside the reactor tube. The tube OD and ID are 1.43 and 0.8 cm, respectively. 54
Figure 27: System pressures during injection 1. 55
Figure 28: RGA partial pressure signals during injection 1. 56
Figure 29: Surface-mount thermocouple signals during injection 1. 57
Figure 30: Reactor control volume schematic. 57
Figure 31: Receiver contents and fill rate for injection 1. The black curve is computed from PVT data; red curve is computed by numerically integrating the fill rate. Good agreement between these curves confirms that the numerical differencing scheme is appropriate. 58
Figure 32: Receiver vessel contents; D_2 is the only significant gas present. 59
Figure 33: Oxygen mole balance. 59
Figure 34: Total reactor oxygen inflow and deuterium outflow during injection 1. 60
Figure 35: Reactor mole-balance derived D_2 evolution per O_2 consumption. The black curve is the computed data. The green band estimates error. Theoretical values for two possible oxidation reactions are indicated on the ordinate..... 61
Figure 36: DGM flow parameters vs. average bed pressure before oxidation and after injection-1. Assuming the oxidation product is U_3O_8, injection 1 oxidized 10 mole-% of the bed. Measured data are dots. Least-squares regression lines are included for reference. 62
Figure 37: The UD_3 oxidation reaction front predicted by the model at various times for the first oxygen injection experiment. Color is used here only to distinguish between large and small reaction rates at each time state. The actual maximum reaction rate decreases with increasing time. 63
Figure 38: Predictions for the (a) temperature and (b) deuterium distributions in the vicinity of the bed, early in the first oxygen injection experiment, and the (c) final UD_3 distribution at the end of the experiment..... 64
Figure 39: The pressure decay in the gas source vessel (a) during the first oxygen injection experiment, and (b) during the subsequent flow-through test. 64
Figure 40: (a) The calculated temperature profiles in the bed on axis at various times, and (b) a comparison of calculated and measured temperatures at the locations of the thermocouples..... 65
Figure 41: The calculated (a) UD_3 and (b) oxygen mole fraction profiles on axis near the leading edge of the bed at various times..... 66
Figure 42: Pressure data from injection-2..... 67
Figure 43: RGA data from injection-2..... 67

Figure 44: Reactor mole-balance derived D_2 evolution per O_2 consumption. The black curve is the computed data. The green band estimates error. Theoretical values for two possible oxidation reactions are indicated on the ordinate. 68
Figure 45: The UD_3 (a) oxidation and (b) decomposition fronts, and the (c) U oxidation front, early (t = 30s) in the simulation of the second oxygen injection experiment. 69
Figure 46: Predictions for the (a) temperature (with flow streamlines), (b) U and (c) UD_3 distributions in the vicinity of the bed, early in the second oxygen injection experiment, and (d) the final UD_3 distribution at the end of the experiment. 70
Figure 47: The pressure decay in the gas source vessel (a) during the second oxygen injection experiment, and (b) during the flow-through test that followed it. 71
Figure 48: (a) The calculated temperature profiles in the bed on axis at various times, and (b) a comparison of calculated and measured temperatures at the locations of the thermocouples. 71
Figure 49: The calculated results for (a) the reaction rates on axis in the bed, and (b) the integral of the reaction rates over the entire bed as functions of time. 72
Figure 50: The calculated (a) UD_3 and (b) U profiles on axis near the leading edge of the bed at various times. 72
Figure 51: Pressures during injection-3. 73
Figure 52: RGA signals during injection-3. The data are shown on linear (top) and log (bottom) scales. 74
Figure 53: Cumulative D_2 evolved and O_2 consumed during injection-3. 76
Figure 54: Reactor surface-temperatures during injection-3. 77
Figure 55: Predictions for the (a) temperature, (b) UD_3 oxidation, (c) UD_3 decomposition, (d) U oxidation, (e) UD_3, and (f) U distributions in the vicinity of the bed, early (t = 44 s) in the third oxygen injection experiment. 78
Figure 56: The pressure decay in the gas source vessel (a) during the third oxygen injection experiment, and (b) during the flow-through test that followed it. 79
Figure 57: (a) The calculated temperature profiles in the bed on axis at various times, and (b) a comparison of calculated and measured temperatures at the locations of the thermocouples for the third oxygen injection. 79
Figure 58: The calculated results for (a) the reaction rates on axis in the bed, and (b) the integral of the reaction rates over the entire bed as functions of time for the third oxygen injection. 80
Figure 59: The gas composition exiting the reactor for the third oxygen injection. (a) Results presented using as-measured and as-calculated time scales. (b) Results presented after shifting the calculated time scale to better align with the measured results. 81
Figure 60: Ultimate D/U vs. hydride cycle number for Reactor #2. 82
Figure 61: Reactor #2 thermocouple locations (dimensions in inches). 83
Figure 62: Pressure data from injection-1. The bottom plot shows only the injection portion of the gas transfer (28 to 45 s). 84
Figure 63: Radiograph of Reactor #2 after injection-1. Flow direction is from left to right. 85
Figure 64: A detail-view of injection-1 pressure data. 86
Figure 65: Reactor #3, the mini-conflat design. 88
Figure 66: Estimated gas temperature at the bed inlet during injection-1. 89
Figure 67: Pressures during Reactor #3 injection-1. 90
Figure 68: Reactor #3 after injection-1. Flow direction is right to left. 91
Figure 69: Detail view of pressures during injection-1. 92
Figure 70: Measured relative sensitivity factors and best-fit curves. 94

Figure 71: Sensitivity factor validation test 95
Figure 72: Reactor #4 exchange test-1. Beyond 80 seconds back-mixing affects the RGA data. 96
Figure 73: Isotope exchange results. Plots are arranged by temperature (columns) and exchange-direction (rows). Test-1's (UD_3 + H_2) initial temperature was 26°C while test-6's initial temperature was 39°C. In the other cases, the initial temperatures match to within 2°C. 97
Figure 74: Conceptual picture of gas-to-solid isotope exchange 98
Figure 75: Effluent composition and flow rate during the mixed gas test. 100

TABLES

Table 1: Reactor bed parameters 45
Table 2: RGA channel configuration 55
Table 3: Reactor #2 injection-1 LLNL gas analysis results 86
Table 4: Reactor #4 injection-1 gas analysis 92

NOMENCLATURE

Variable

c	oxygen mass concentration (g/cm^3)
c_p	specific heat, mass based (J/g-K)
C	specific heat, molar based (J/mol-K)
D	diffusivity (cm^2/s)
D_2	deuterium mass concentration (g/cm^3)
d	bed diameter (cm)
d_p	pore size (cm)
d_m	molecular diameter (cm)
F	fraction of the bed that is oxidized
ΔH	enthalpy of reaction (J/mol)
K	permeability (cm^2)
Kn	Knudsen number
k	thermal conductivity (W/cm-K)
k_{ox}	oxidation rate constant (mol/cm^{3}s)
k_{UD3}	decomposition rate constant (mol/cm^3-s)
M	molecular weight (g/mol)
n	molar density (mol/cm^3)
n'	molecular density (#/cm^3)
O_2	oxygen mass concentration (g/cm^3)
p	gas pressure (g/s^{2}cm)
Q	energy source term (W/cm^3)
R	mass source term for gas (g/cm^3) or for solid species (mol/cm^3)
T	temperature (C) or (K)
V	gas velocity vector (cm/s)
ΔV	solid volume increase upon changing from hydride to oxide

Greek symbols

ϕ	porosity
λ	mean free path (cm)
μ	gas viscosity (g/cm s)
ρ	total mass density of gas (g/cm^3)
τ	tortuosity

Subscripts

c	oxygen term
eq	equilibrium
5,6,7	reactions described by Equations 5,6,7

Superscripts

0	initial value, or all hydride phase
1	all oxide phase

1 INTRODUCTION

A method is sought for rapidly generating hydrogen gas from a metal hydride storage system. The goal is to release gram quantities of hydrogen from the storage material in ~2 seconds and to be able to do this over a broad temperature range (i.e. between −60 and 80°C). To enable this, we propose mixing an externally-stored fluid reactant with a metal hydride at gas-generation time.

Uranium hydride was selected as the hydrogen storage material because it: has favorable pressure-composition-temperature characteristics [1]; is highly reactive with many compounds [2-13]; and is easily made into a fine, ~ 1 m^2/g, powder [14-15].

To implement this concept one must identify a suitable reactant to introduce into the hydride bed at function time. This project, focused on the reactant and uranium hydride reactor, seeks to determine what reactant is most appropriate.

Considerations of reaction thermodynamics, reactant form, safety, chemical stability, and reactivity with UH_3 and U suggest O_2 gas, Cl_2 gas, and HCl gas as leading candidates. For reasons given in Section 2, we elected to begin our study with oxygen gas using sub-scale (2.9 grams UH_3) fixed-bed reactors.

From numerical simulations and experiments, described in Sections 0 and 0 respectively, it was found that:

- UD_3 powder beds can be prepared precisely enough to make valid reactor-to-reactor comparisons. After conditioning the bed with 3 hydride/dehydride cycles, the bed has uniform density and the UD_3 particles may be approximated as ~ 0.5-μm spheres.
- The UD_3+O_2 reaction is significantly faster than the U+O_2 reaction near room temperature (30–40 °C).
- UD_3 reacts completely with no passivation, forming, under these experimental conditions, U_3O_8 as the major product.
- Under all conditions studied, very little water exits the reactor. Therefore, if the UD_3 + O_2 reaction produces water, it is likely a relatively short-lived intermediate species.
- As a UD_3 bed is oxidized to U_3O_8, $UD_3 \rightarrow U_3O_8$ particle expansion drastically alters the bed properties (porosity and permeability).
- Rapid oxygen injection leads to rapid local heating which, for this bed configuration, leads to local bed sintering and flow channeling.
- The UD_3 + O_2 reaction is still prompt at an initial reactor temperature of −80°C; the promptness is comparable to 30°C initial temperature.

All of these findings encourage continued development of a reactive thermal decomposition system. The major challenge for this concept appears to be heat management. Alternate reactors, which are designed to manage the significant internal heat generated by the exothermic oxidation reaction, are proposed for testing in future work.

In addition to oxygen injection experiments, we performed a set of hydrogen isotope exchange tests on one of the reactors. The intent of these tests was to measure uranium hydride H/D isotope exchange kinetics. Hydrogen isotope separation systems based on uranium hydride beds have been proposed by others [16]. Systems have been proposed largely because hydrogen isotope separation factors are reasonably well established, [16-17], and because the separation factors are different enough from unity to make such systems thermodynamically attractive. However, very little isotope exchange kinetic data is available and therefore it is impossible to design an optimal separation system. The intent of the isotope exchange tests was to generate a data set from which isotope exchange rates could be inferred, similar to what was done by Foltz and Melius, [18], for palladium hydride.

The experiments described in Section 4.5 indicate that, while isotope exchange appears significantly slower in uranium hydride than in palladium hydride, the exchange kinetics are likely fast enough for isotope separation applications if the uranium hydride bed is heated to temperatures near 250°C. In the one reactor studied thus far, which contains ~ 0.5 μm diameter uranium hydride particles, it was found that hydrogen diffusion in the hydride particles is the rate limiting step in the overall gas-to-particle exchange process; for both $UD_3 + H_2$ and $UH_3 + D_2$ exchange, at temperatures between 25 and 250°C.

The isotope exchange results need to be confirmed with other reactors; and, in addition, a system-level exchange and transport model should be used to identify intra-particle diffusion coefficients. These are valuable directions for future work.

2 REACTANT SELECTION AND EXPERIMENTAL APPARATUS DESIGN

2.1 Thermodynamic considerations

The main chemical reaction of interest is

$$2\,\mathrm{UH_3} \rightarrow 2\,\mathrm{U} + 3\,\mathrm{H_2}. \tag{1}$$

This reaction is endothermic, requiring 127.2 kJ/mol reactant. Thermodynamic data here are from the CRC Handbook and NIST-JANAF thermochemical tables, and we assume all H isotopes have the same thermodynamic parameters. We wish to identify chemical reactions that are at least as exothermic to provide this energy. An example is

$$\mathrm{U} + \mathrm{O_2} \rightarrow \mathrm{UO_2}, \tag{2}$$

which provides 1085 kJ/mol. From that, about 0.12 mol O_2 would be able to decompose 1 mol UH_3, assuming all reactions go to completion and nothing becomes warmer during reaction. More O_2 would be needed if the products or surroundings became warmer; because additional energy is required to heat the reactants and products to temperatures required for UH_3 decomposition. The heat capacity of the products makes a contribution that may be significant because the UH_3 decomposition reaction must be heated to about 425 C to proceed rapidly. Heat capacities are about 30 J/mol K for U, and approximately 30 J/mol K times the number of atoms minus 1 for other products. If x is the fraction of uranium consumed exothermically, and the initial temperature is 25 C (for a 400 C change), an energy balance in kJ/mol can be written as

$$\Delta H_{\mathrm{UH_3}} + \Delta T\left[c_{\mathrm{H_2}} \cdot \frac{\mathrm{mol\,H_2}}{\mathrm{mol\,U}} + c_{\mathrm{U}}\left(1-x\right) + c_{\mathrm{U(IV)}}x\right] = x\,\Delta H_{\mathrm{U(IV)}}, \tag{3}$$

where the first term is the enthalpy of UH_3 decomposition, the terms in brackets are for heating of H_2, U, and UO_2, respectively, and the right-hand side term is the enthalpy of UO_2 formation.

Plugging in values as mentioned above:

$$127.2 + 400\left[0.03\cdot 1.5 + 0.03\left(1-x\right) + 0.06x\right] = 1085x. \tag{4}$$

This evaluates to x = 0.15.

This oxidation can proceed farther, to U(VI):

$$2\,\mathrm{U} + 3\,\mathrm{O_2} \rightarrow 2\,\mathrm{UO_3}, \tag{5}$$

which provides 1224 kJ/mol U, but only 816 kJ/mol O_2. If all oxidation occurs according to this reaction, about 0.16 mol O_2 would be needed; with heating, this is about 0.2 mol.

Water may be a byproduct of this process, according to

$$4\,UH_3 + 3\,O_2 \rightarrow 4\,U + 6\,H_2O. \tag{6}$$

However, this reaction is likely to proceed farther, [19],:

$$U + 2\,H_2O \rightarrow UO_2 + 2\,H_2. \tag{7}$$

The heat of formation of gas-phase water is −242 kJ/mol, and two moles are needed, so the net enthalpy is 601 kJ/mol U. Not only is the uranium likely to react with any water byproducts, water itself is potentially useful as the oxidizer. About 0.42 mol water could provide the energy to decompose 1 mol UH_3. It furthermore adds 0.42 mol hydrogen to the 1.5 mol from the uranium. The additional moles of products in this case compared to the first case requires a larger excess of the oxidant to account for heat capacity. Calculating as above:

$$127.2 + 400\left[0.03\cdot\left(1.5+2x\right)+0.03\left(1-x\right)+0.06x\right] = 601x, \tag{8}$$

so about 0.55 mol reactant is needed to both drive the reaction and heat the products. The U(VI) version of this is

$$U + 3\,H_2O \rightarrow UO_3 + 3\,H_2, \tag{9}$$

which gives 498 kJ/mol U, and requires about 0.77 mol water to react 1 mol UH_3. This becomes 1.1 mol water for reaction with heating.

While the thermodynamics are favorable, both oxygen and water have potential drawbacks as reactants. At the outset of this investigation it was postulated that oxygen may form a passive oxide shell on a uranium or uranium hydride particle, preventing the reaction from going to completion. In addition, pure water could condense or freeze during low-temperature storage, making mass transport difficult. Consequently other reactants were considered which may be able to overcome these potential problems, should they arise. It is believed that halogens or halides would be unlikely to result in passivation, and some of these reactants can remain as a gas, neat liquid, or aqueous solution over a wide temperature range.

For chlorine, the reactions are

$$U + 2\,Cl_2 \rightarrow UCl_4, \tag{10}$$

$$U + 3\,Cl_2 \rightarrow UCl_6. \tag{11}$$

These are nearly as exothermic per mol U as O_2, but require more moles of reactant. Reaching U(IV) provides 1020 kJ/mol U, and going to U(VI) gives 1092 kJ/mol U. This translates to 0.25 and 0.35 mol Cl_2 to decompose 1 mol UH_3, or 0.32 and 0.45 with heating. Chlorine is a gas above -34 C at 1 atm and it may be stored compactly as a compressed liquid. However, chlorine may present special safety and engineering challenges to our research because it can be incompatible with stainless steels, especially under suboptimal reaction conditions, where mixtures of hot water and chlorine may be present.

Just as water may be an intermediate when oxygen is used, HCl may be present in the chlorine reaction, and could be a reactant on its own. This reaction is

$$\mathrm{U} + 4\,\mathrm{HCl} \rightarrow \mathrm{UCl_4} + 2\,\mathrm{H_2}, \tag{12}$$

$$\mathrm{U} + 6\,\mathrm{HCl} \rightarrow \mathrm{UCl_6} + 3\,\mathrm{H_2}. \tag{13}$$

For U(IV), the reaction generates 650 kJ/mol U, requiring 0.78 mol HCl to react 1 mol UH_3. For U(VI), the reaction generates 538 kJ/mol U, requiring 1.4 mol HCl to react 1 mol UH_3. With heating, these values are 1.1 and 2.0 mol HCl for U(IV) and U(VI), respectively. Hydrogen chloride is a gas above −85°C at 1 atm. Near room temperature, it condenses at about 600 psi (4.136 MPa). It thus has advantages and disadvantages similar to chlorine.

Perhaps the most significant disadvantage of using pure halogen or halide reactants is that the product uranium compounds can be volatile. Uranium hexachloride can vaporize in the temperature and pressure ranges expected to be necessary for reaction. Fluorides also have favorable thermochemistry, although uranium hexafluoride also vaporizes at low temperatures. The main advantage of the halogens or halides is that they prevent passivation, and it may be that a relatively small mole fraction added along with oxygen would be sufficient to prevent this without generating volatile uranium species.

2.2 Prior work on the reactivity of UH_3

Others have used steam, [20], or aqueous HCl, [12], to liberate hydrogen from solid hydrides other than that of uranium. In the former case, excess steam was used, and condensed to separate it from the product.

The reaction of UH_3 with aqueous HCl has been studied by several groups. An early study, [9], examined the reaction of UH_3 with many liquid-phase oxidants. Water added slowly or to small quantities results in passivated material, but on larger scales with rapid mixing, the material became red hot. They report that aqueous HCl reacts more slowly with UH_3 than with U metal, even when boiling, but addition of hydrogen peroxide accelerated the reaction. Concentrated nitric acid reacted rapidly, as did 30% hydrogen peroxide. Glacial acetic acid did not, but did when HCl gas was bubbled through the solution. Silver nitrate is an effective oxidant, as are other obvious choices such as Ce(IV) or permanganate.

In gas-phase reactions, this group reported the use of elevated temperature except for HF, which apparently reacts at room temperature at a modest pace. HCl gas at 300 C forms only UCl_3.

Chlorine gas, on the other hand, reacts vigorously and proceeds to U(IV). Br_2 reacts similarly, except that its vapor is less conveniently mixed with the UH_3. Iodide products easily decomposed. Carbon dioxide reacts even at room temperature by oxidizing the uranium and producing carbon monoxide; in our case, an undesirable byproduct. Carbon tetrachloride reacts vigorously, producing carbide and chloride products.

A later study of the reaction of UH_3 with aqueous HCl, [10], showed an initially rapid reaction using 16M DCl in D_2O that liberates about 80% of the total gas, which itself is about 75% HD. The byproduct is a soluble U(III) species that slowly oxidizes to U(IV) with evolution of gas having a lower HD content. Slightly lower acid concentrations (11M) proceed much more slowly, generating much less HD, and produce solid oxide byproducts along with some soluble product. They attribute these results to formation of a passivating oxide layer in which oxide ions mediate the reaction, forming H_2 under this layer or D_2 at its surface. Use of strong oxidants such as Ce(IV), Fe(III), H_2O_2, an $AgNO_3$ resulted in very little mixed isotope [21]. Sulfuric acid was also used, and found to produce H_2S as a byproduct. Relatively dilute (1M) aqueous HF consumed most of the hydride within a few minutes, producing an amount of HD comparable to the H_2 and D_2 produced in that reaction.

The relatively unstable iodide products were studied in detail more recently, [22], where the utility of uranium iodides as intermediates in the study of uranium coordination chemistry has been recognized. In this work, iodine in diethyl ether reacts vigorously at room temperature to form $UI_4(OEt_2)_2$. Another approach includes preparation of the triflate, $U(OSO_2CF_3)_3$ [13]. When anhydrous triflic acid is used, formation of this from UH_3 proceeds at room temperature.

The variety of reactions described here illustrate the diverse range of reaction conditions that can be used to liberate hydrogen gas from UH_3. Passivation by an oxide layer slows the reaction in many cases, but this apparently does not inhibit the reaction of gaseous or aqueous HF, Cl_2, HCl in glacial acetic acid, 16 M aqueous HCl, I_2 in an aprotic solvent, or anhydrous triflic acid. These reactions can proceed at low temperature, but require a stoichiometric or excess amount of oxidant, and may produce volatile byproducts at elevated temperature unless methods are developed to prevent that. It is likely that HF and Cl_2 are able to corrode an oxide layer at low temperature, so coinjection of either of these may help to initiate or sustain a reaction by oxygen.

2.3 Reactant selection

Based on the above work pure-oxygen was selected as the first reactant to investigate. It was selected because it provides a desirable combination of: reaction energetics, low reaction-product volatility, and is compatible with simple storage and delivery methods. Should undesirable levels of surface-passivation hinder hydride-oxygen or uranium-oxygen reactivity, then halogens, Cl_2 or DCl, could be added as co-reactants.

2.4 Reactor and apparatus design

2.4.1 Reactor

An integral fixed-bed reactor configuration was selected for this investigation. Uranium hydride is radioactive and pyrophoric so the reactor was designed to minimize the quantity of material

needed while still allowing for precise gas-quantity measurements. Figure 1 shows a solid model of the reactor.

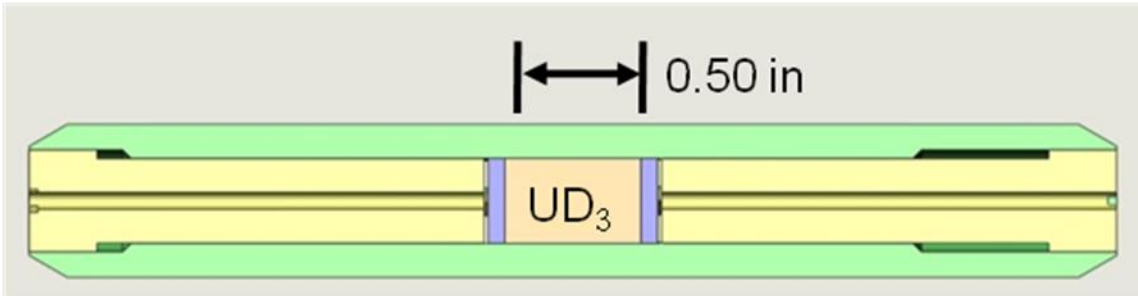

Figure 1: CAD model of the reactor. The bed is ϕ0.316 × 0.50 in^2 (0.803 × 1.27 cm^2) and contains about 2.9 g of UD_3. The void fraction is approximately 0.60.

A 4-inch-long (10.16 cm), 316SS, 9/16-inch Autoclave Engineers (AE) medium-pressure nipple was modified to make the reactor tube (green). The nipple is bored to 0.316 inch diameter and both ends are threaded, 3/8-24 UNF, to accept spacers (the long yellow parts, threads are on the outside ends). The 316 SS spacers lock the frits in place and occupy what would otherwise be empty space. The bed (orange) is in the center of the assembly, between Mott 0.317-0.062-1-A-OF frits (blue, 1 μm filtration rating). A star-shaped flow distribution pattern is machined into the spacers to distribute the gas from the ϕ0.062-inch (0.157 cm) thru-hole to the ϕ0.316-inch (0.903-cm) frit face. Figure 2 is a detail-view of the flow distribution pattern.

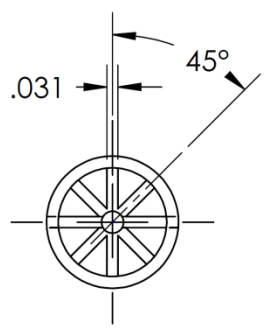

Figure 2: An end-on view of reactor spacer showing the flow distribution pattern.

The nipple assembly was mated to 9/16-inch-to-¼-inch high-pressure adapters that connect the nipple to AE 60VM-7047 valves. These three-port valves allow upstream and downstream pressure transducers to be closely mated to the nipple assembly.

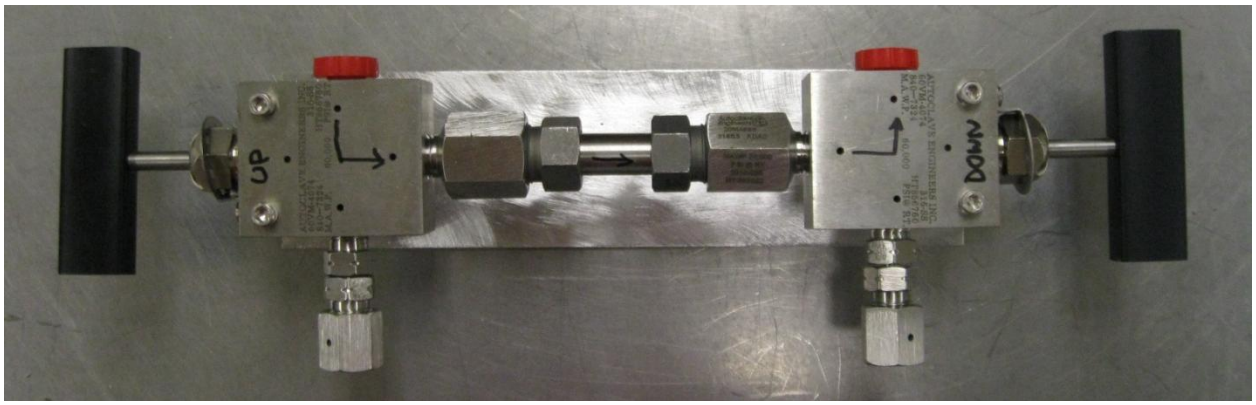

Figure 3: A reactor assembly. The AE F250C caps are replaced with Teledyne Taber pressure transducers when the reactor is connected to the experiment apparatus.

2.4.2 Experiment apparatus

The gas-handling apparatus was configured with a piston-driven injection volume to allow the injected quantity and injection rate to be varied independently. Figure 4 is a schematic of the apparatus.

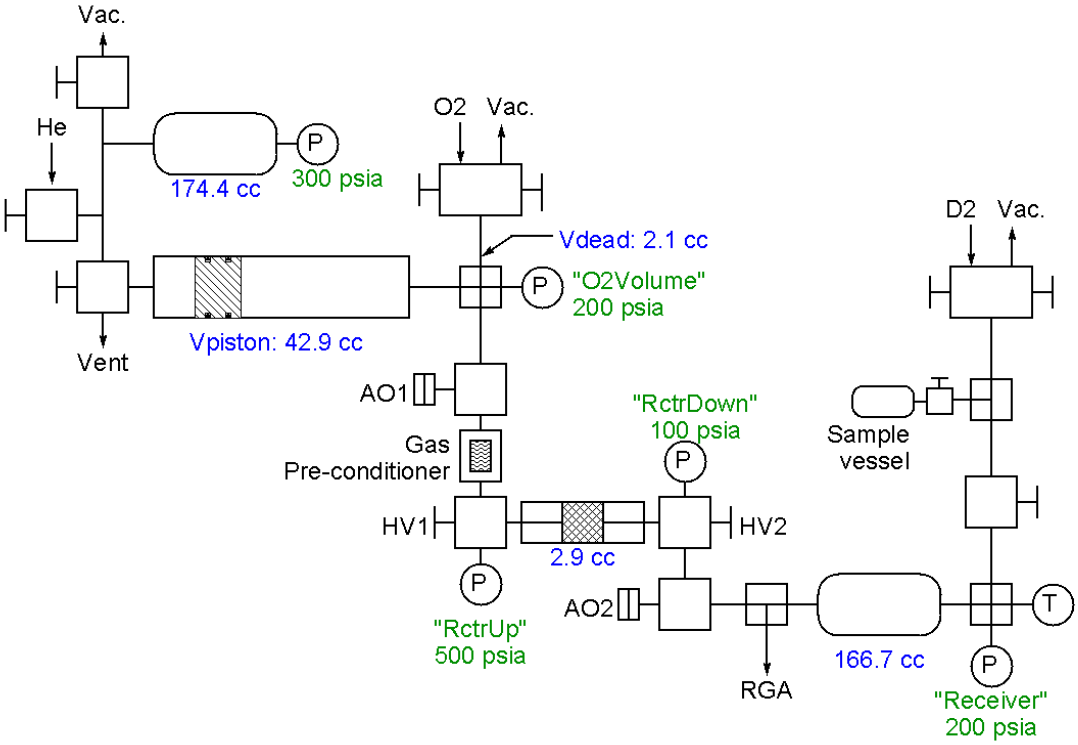

Figure 4: Experiment apparatus. The reactor is at the center of the system. The piston-driver is on the left and the product collection tank (receiver) is on the right. Volumes are listed in blue and pressure transducers, "P," are identified in green. The "T" symbol is a ϕ0.010 inch thermocouple that extends into the receiver tank.

Because gas quantities are small, great care was taken to minimize dead volume. The apparatus was assembled from commercially available components. The majority of the system was built from AE ¼-inch high-pressure tubing (0.083 inch bore) and components. Pressure transducers are all low-volume Teledyne-Taber models similar to the 2214; their internal wetted volumes are less than 0.2 cc.

The gasses, H_2, D_2, He, and O_2 come from 1A size cylinders supplied by Matheson Tri-Gas. The H_2, He, and O_2 are all UHP grade (>99.99% pure) and used without further purification. The D_2 is commercial purity (99.7% D) with 0.3 % H impurity. Non-hydrogen isotope impurities in the D_2 are ~100 ppm, similar to UHP grade gas. The cylinders were connected to the apparatus with standard SS tubing. During operations, care was taken to properly evacuate and purge the gas supply lines to maintain gas purity. The two He and O_2 cylinders can be seen in Figure 5.

Figure 5: A picture of the experiment manifold; before the residual gas analyzer system was added.

For non-ambient temperature tests, the reactor is heated or cooled using either electrical heating tape or a cold-chamber. The cold-chamber is a simple aluminum box that fits around the reactor; its temperature is regulated by injecting doses of boiling nitrogen into the box.

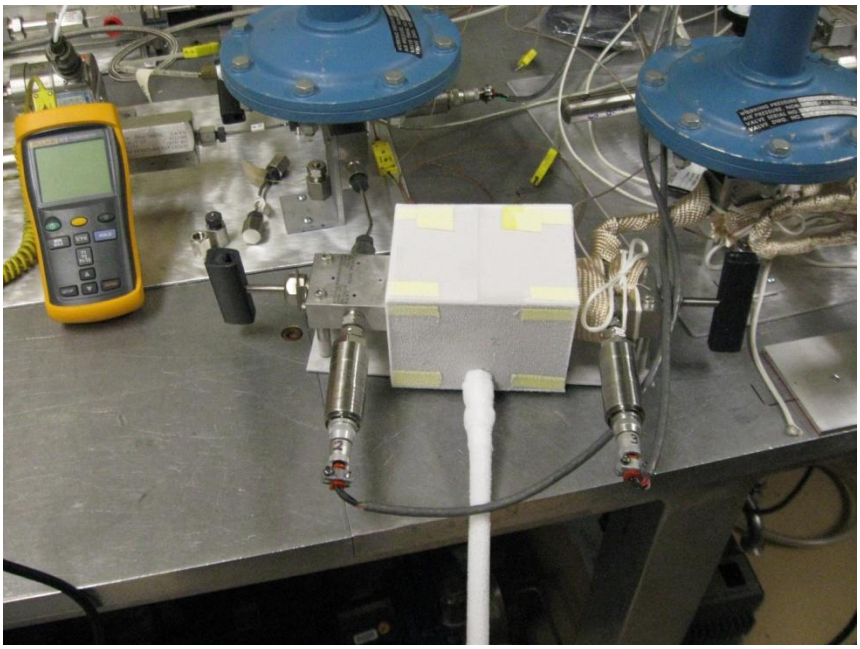

Figure 6: Cold-chamber in operation; the reactor temperature is about −40°C.

After testing Reactor #3, a custom gas pre-conditioner was added upstream of HV1 to pre-condition the gas to the reactor temperature. The gas pre-conditioner, shown in Figure 7, contains 8 EA 0.750-0.062-5-A-OF 316 SS Mott-supplied frits.

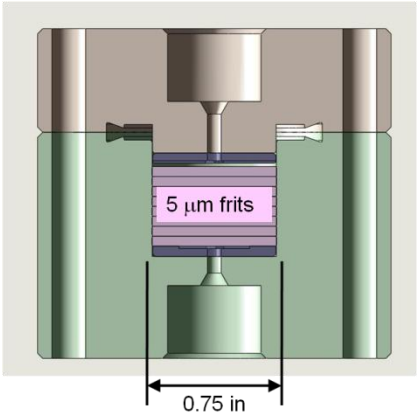

Figure 7: Cross-section view of the gas pre-conditioner.

The pre-conditioner temperature was maintained at the reactor temperature. As the injected gas passes through the frits, the gas and steel thermally equilibrate. The thermal mass of the frits and the gas-frit contact time are both sufficient so that the exiting gas is predicted to be at essentially the same temperature as the reactor. The hand-valve between the pre-conditioner and reactor was also temperature controlled to the reactor temperature (when possible due to valve operating-

temperature limits[1]). This arrangement allows the rest of the apparatus to be kept at ambient temperature; greatly simplifying system-design and operation.

The reactor effluent gas was monitored by a real time residual gas analyzer (RGA) in a high-vacuum system. The RGA system continuously sampled gas from the high-pressure manifold through a crimped capillary leak. The capillary reduces the pressure in the high-pressure manifold, ~10^3 torr, to a pressure compatible with the RGA, ~10^{-6} torr, in a single step. A turbomolecular pump, in series with an oil-sealed vane pump, continuously evacuates the RGA volume. This technology is well developed and understood [23-24].

The crimped capillary was located close to the reactor exit. Dead volume was minimized and the plumbing between the reactor and capillary was carefully designed to minimize gas mixing. In addition, the capillary interface, located between the reactor outlet and receiver volume inlet, was configured to minimize back-mixing between emerging reactor product gas and gas already in the receiver volume.

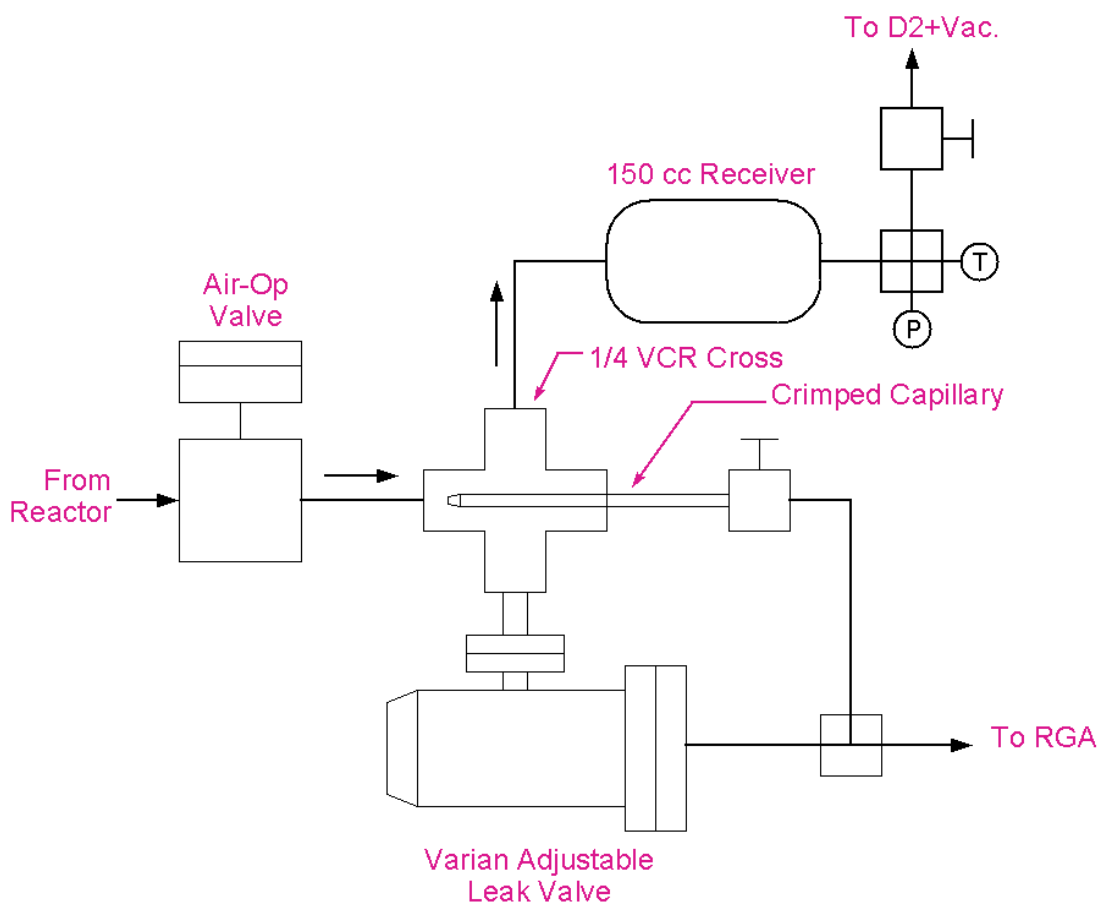

Figure 8: Schematic of the crimped capillary interface.

[1] The valve's operating range is −20 to 150°C; it therefore cannot be heated/cooled as aggressively as the reactor and pre-conditioner.

The capillary was placed in parallel with a Varian adjustable leak valve. This valve is used when sampling receiver gas that is above or below the capillary's working pressure-range (~1 to ~100 psia). It was not used the injection tests. The capillary was located inside a ¼-VCR cross such that the incoming gas impinges directly on the capillary inlet. This ensures that, when there is sufficient flow exiting the reactor, the capillary always sampled the most recent effluent gas.

The RGA-system response time was measured by applying a pressure step-change upstream of the capillary and recording the RGA response. The receiver pressure was recorded using a Nicolet Odyssey operating at a 100 Hz sampling rate. The RGA signal was recorded on a PC using LabVIEW software supplied by Stanford Research Systems and modified by Sandia to increase the sampling rate from 1 to 10 Hz. The time-bases of the two signals were synchronized by matching the RGA system's Granville Phillips ion gauge output, recorded on the Odyssey, with the RGA signals recorded on the PC. The RGA and pressure signals can be synchronized to within less than 1 RGA sampling period (0.10 seconds) with this method.

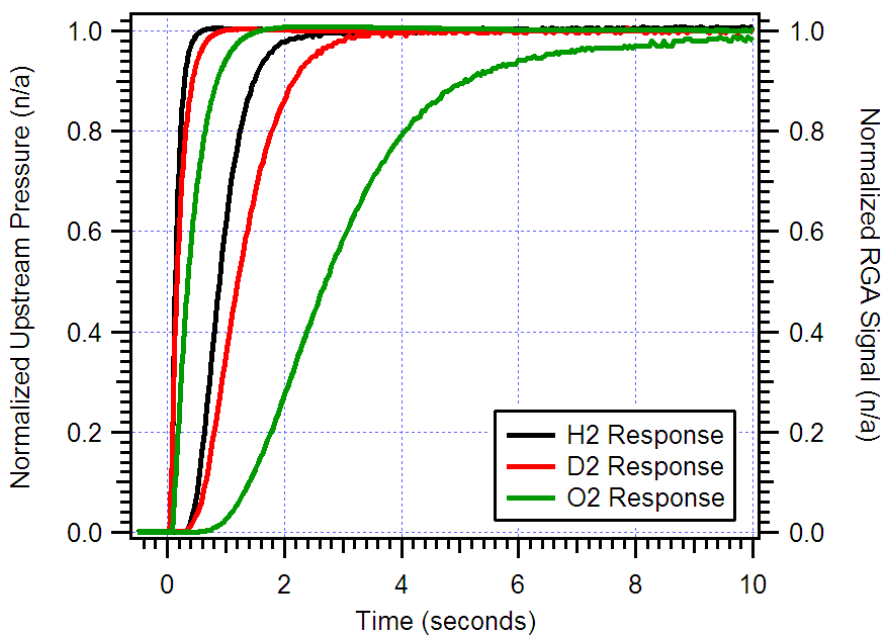

Figure 9: RGA response times for H_2, D_2, and O_2.

The leftmost 3 curves are, from left to right, normalized upstream (input) pressure for H_2, D_2, and O_2 respectively. The three rightmost curves are normalized RGA response. Final pressures were approximately 40, 20, and 40 psia for H_2, D_2, and O_2. The 90% response times are 1.4, 2.0, and 4.9 seconds for H_2, D_2, and O_2. For some tests, RGA response-time effects are not significant; however, for fast injections it is an important consideration. This will be addressed

for each test. The response-time ratios, 1.0, 1.4, and 3.5, are consistent with the expected square root of the molecular weight ($MW^{1/2}$) scaling[2].

Tracer tests characterized gas mixing in the reactor plumbing and back-mixing between the capillary and its downstream plumbing. Specifically, reactor gas mixing and dead-volume effects were characterized using a helium tracer test. A UH_3 bed was evacuated to 0.25 psia then topped to 70 psia with helium gas. Because the equilibrium overpressure of H_2 above UH_3 is low, the reactor gas was essentially 100% He. The oxygen gas supply volume was filled with H_2, also to 70 psia. The initial system configuration is in Figure 10.

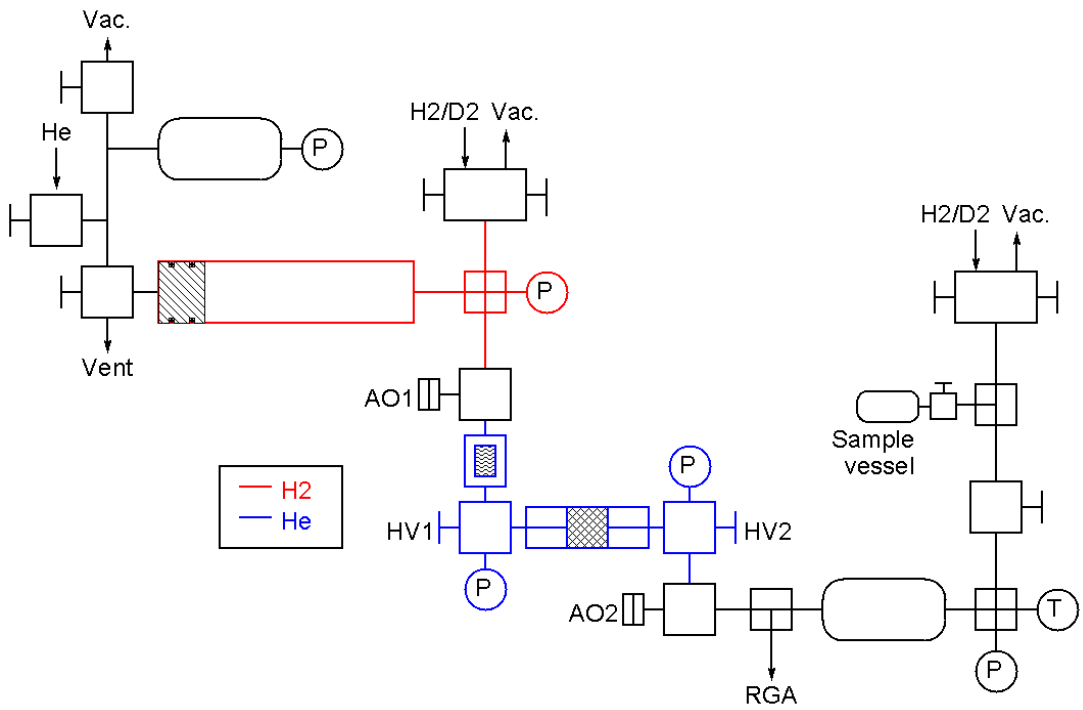

Figure 10: Initial system configuration for reactor gas-mixing test.

Air-op valve #1 (AO1) was opened at 0 seconds. Because the bed and source volumes were at nearly equal pressure very little gas was transferred or mixed between the volumes. Ten seconds later AO2 was opened, establishing flow through the reactor. The RGA monitored the H_2, HD, and He signals. The amount of transferred gas and gas transfer rate were computed from the receiver pressure. Results are shown in Figure 11.

[2] It is understood that the RGA-system response time is given by the RGA chamber's CSTR residence time, i.e. chamber volume / effective volumetric pumping speed. Because the gas in the RGA chamber is in free molecular flow, the pumping speed is proportional to $1/MW^{1/2}$.

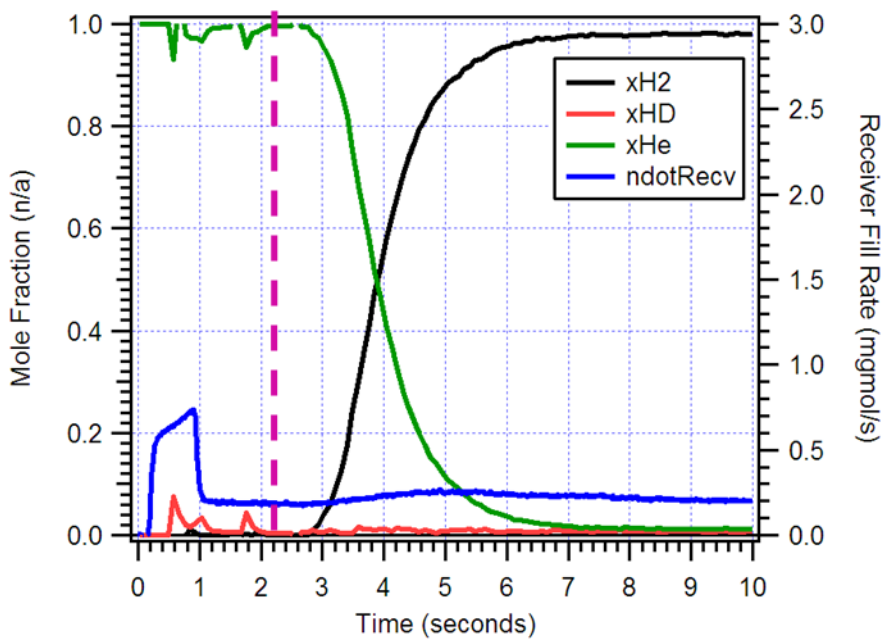

Figure 11: RGA-derived mole fractions and receiver fill rate. The pink line indicates the time required to flush the He overpressure assuming perfect plug-flow in the reactor plumbing.

The He mole fraction begins to decrease about 0.5 seconds after the plug-flow predicted switchover time (at 2.5 s). It decreases steadily, reaching 10% at 5 seconds. This measured response time, 90% response in 2.5 seconds, is only slightly longer than the RGA's known response-time (90% response in 2.0 s). Therefore the true reactor flush time is perhaps only ~1 second longer than predicted by plug-flow theory. This implies that only 0.2 mgmol of additional gas are required above the plug-flow predicted value before helium levels are insignificant. If the reactor plumbing dead-space is assumed to be a stirred-tank reactor, then the 0.2 mgmol of gas at 70 psia is equivalent to a 0.3 cm^3 dead-volume. Under all of the test conditions described in Section 0, reactor dead-volume and mixing effects are essentially insignificant.

Back-mixing between the RGA-capillary and the downstream plumbing was also characterized with a tracer experiment. In this test, a UH_3 bed was topped to 70 psia with H_2 and the O2Volume (see Figure 4) was filled to 190 psia with H_2. The receiver plumbing (up to AO2) was backfilled to 25 psia with D2. At 0 seconds, AO2 was opened followed by AO1 at 10 seconds. Gas pressures, temperatures, and RGA signals were monitored. Computed mole fractions are shown in Figure 12; alongside the receiver fill rate.

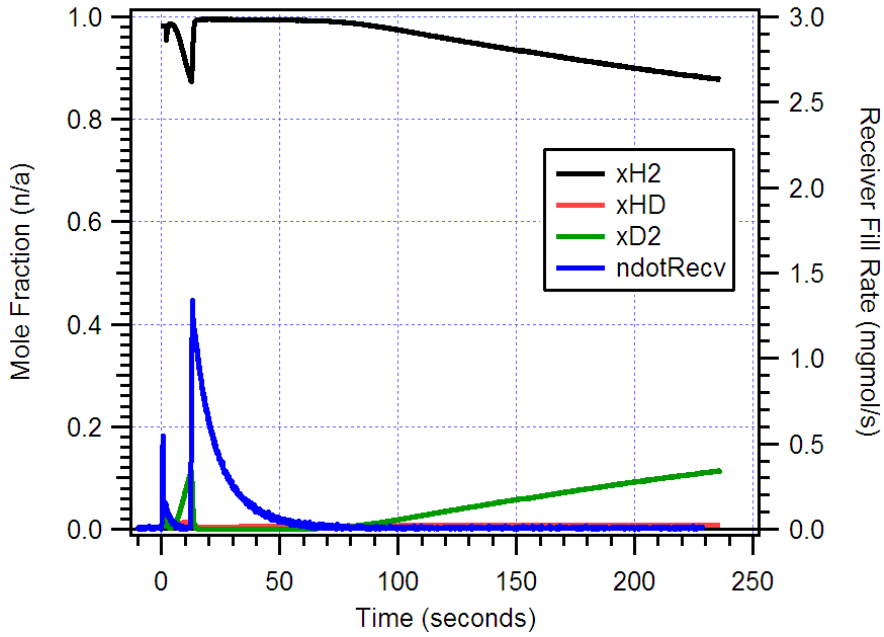

Figure 12: RGA-derived mole fractions during the back-mixing test.

At 0 seconds, when the 70 psia H_2-filled reactor vents into the 25 psia D_2-filled receiver, H_2 displaces the D_2 near the crimped capillary inlet. However, because minimal gas was transferred (0.7 mgmol), D_2 remains in the VCR cross and/or Varian leak valve. This D_2 quickly migrates back to the capillary when the flow rate drops below 50×10^{-6} mol/s. At 12 seconds, when AO1 is opened, this residual D_2 is quickly flushed away and does not begin to reappear until 80 seconds, when the flow rate has dropped to 25×10^{-6} mol/s.

It is only when the flow velocity in the ϕ 0.18 inch ID VCR cross decreases to less than 5 cm/s that back-mixing becomes important. This required velocity is low enough that the RGA signals are not corrupted by back-mixing until the flow rates are low enough to be unimportant. In other words, in most tests, back mixing is not significant until over 99% of the gas has been transferred to the receiver.

3 NUMERICAL SIMULATIONS

3.1 Motivation

Modeling is a useful method for developing an understanding of the behavior of complex systems. The storage system of interest here is a good example, and may be called a chemical reactor to better acknowledge its dynamic behavior. As discussed below, the reactor performance involves an interaction between chemical, mechanical, thermal and mass transport phenomena. Given the limitations of experimental diagnostics, the importance of these interactions on the rate of delivery of hydrogen from the reactor would be very difficult to determine by measurements alone. These interactions are explicitly accounted for in the model, and their effects on measurable quantities such as the thermal response of the reactor surface, and the states of the source and exiting gas, are predicted for comparison to the experiments. The model, in turn, relies on experimental results to help guide the selection of parameter values that best represent the real system. So, it is the combination of modeling and experiments that comprises an effective approach to revealing the important phenomena affecting reactor behavior, and ultimately, the development of an optimum reactor design.

3.2 Model description

The model is comprised of the governing equations for momentum, energy and mass transport, the chemical reactions that take place in the hydride material, the material properties, the initial and boundary conditions, the finite element model, and the method of solving the equations. These model features are described below.

3.2.1 Governing transport equations

The release of hydrogen from the reactor begins with the injection of oxygen. Modeling this process requires an equation describing momentum transport. The gas flow paths include both open channels as well as porous media, where the latter creates the dominant restriction to gas flow. Many different forms of equations have been developed for describing flow through porous media [25-26]. One of the simpler forms was selected here, Darcy's equation,

$$\frac{\partial \rho \phi}{\partial t} - \nabla \cdot \left(\frac{K \rho}{\mu} \nabla p \right) = R. \tag{14}$$

The source term on the right accounts for the consumption of oxygen and the production of gas phase deuterium within the hydride bed (it is zero elsewhere). Although the Navier-Stokes equation is more appropriate for describing gas flow through the open channel portions of the system, the flow restrictions there are very small making the details of the viscous and inertial forces in those regions unimportant to the system behavior. Consequently, Darcy's equation was used to describe momentum transport in all portions of the system, where a very large permeability (10^{-3} cm^2) was selected for the open channel regions.

Heat transfer occurs by both convection and conduction. Within the porous media the gas and solid phases are assumed to have the same temperature at any given point and time. The equation used here to describe heat transfer is,

$$\rho c_p \frac{\partial T}{\partial t} + \left(\rho c_p\right)_{gas} V \cdot \nabla T = \nabla \cdot k \nabla T + Q. \tag{15}$$

Note that the second term on the left describing convection uses the density and specific heat of the gas – since that is the phase that is in motion. The thermal inertia term (first term on left) and the conduction term (first term on right) use the properties of the solid phase since they are much larger than the corresponding gas phase values. The source term (second term on the right) accounts for the heat generation by the chemical reactions in the hydride material (it is zero elsewhere).

The gas in this system is a mixture of two species, oxygen and deuterium. Transport of the individual species occurs by convection and diffusion, as described by,

$$\frac{\partial c}{\partial t} + \nabla \cdot cV = \nabla \cdot \left(\rho \mathcal{D} \nabla \frac{c}{\rho} \right) + R_c. \tag{16}$$

Here, c denotes the mass concentration of oxygen. The distribution of the mass concentration of deuterium is given by $\rho - c$. Note that the convection term is in conservative form (i.e., the divergence operator acts on the product of concentration and velocity), which is important due to the variability of the total gas density. The source term (second term on right) accounts for the consumption of oxygen in the hydride material.

The consumption of hydride material is described by the conservation equation,

$$\frac{\mathrm{dUD_3}}{\mathrm{d}t} = R_{\mathrm{UD_3}}, \tag{17}$$

where transport of this species by either diffusion or by mechanical deformation is neglected. A similar equation is used for the conservation of uranium. The distribution of the oxide material (U_3O_8) is given by (UD_3^0-UD_3-U)/3.

3.2.2 Chemical reactions

A set of three chemical reactions was assumed to take place in the hydride material. First, there is the decomposition of uranium hydride to form uranium and deuterium gas,

$$\mathrm{UD_3} \rightarrow \mathrm{U} + \frac{3}{2}\mathrm{D_2}. \tag{18}$$

The rate of this reaction is assumed to follow a standard Arrhenius form, $R_5 = k_5\ [UD_3]\ e^{-Q/T}$, where $k_5 = 14003\ s^{-1}$ and $Q = 8630$ K based on the experiments of Condon [14]. This reaction is assumed to take place only when the local partial pressure of deuterium is less than the temperature dependent uranium hydride equilibrium pressure give by $\log_{10}(p_{eq}) = 9.14 - 4410/T$, where p_{eq} is in torr, as given by Lindner [27]. The enthalpy change for this reaction is $\Delta H_5 = 128000$ J/mol-UD_3 (endothermic).

The second chemical reaction is the oxidation of uranium given by,

$$U + \frac{4}{3}O_2 \rightarrow \frac{1}{3}U_3O_8. \tag{19}$$

Finally, the third reaction is given by the sum of the first two reactions,

$$UD_3 + \frac{4}{3}O_2 \rightarrow \frac{1}{3}U_3O_8 + \frac{3}{2}D_2. \tag{20}$$

This latter equation follows from our experimental observations that uranium hydride reacts with oxygen at room temperature and below. The decomposition rate is very small at these low temperatures, so only the hydride material would have been present, and no uranium. In order to explain the experimental result, the direct oxidation of the hydride material was assumed to take place.

Note that there are several different species of uranium oxide, and that in Equation 7, U_3O_8 is assumed to form. This is based on the experimental measurements of the amount of oxygen that was absorbed by the hydride material and the amount of deuterium that exited the reactor. That is, when a substoichiometric dose of oxygen was introduced under slow reaction conditions, the measured ratio of deuterium released to oxygen absorbed was closer to 1 1/8, corresponding to the formation of U_3O_8, than it was to 1½, corresponding to the formation of uranium dioxide (i.e. $UD_3 + O_2 \rightarrow UO_2 + 3/2\ D_2$). U_3O_8 was also assumed to be the reaction product in Equation 6.

The direct oxidation of uranium hydride has received very little attention in the literature. The small amount of work that has been done is not quantitative in terms of reaction rate [2-3, 6, 28]. The experiments carried out here did not provide quantitative reaction rate data either, however, they did appear to show that the reaction rate at cold temperatures (−60°C) was just as vigorous as at room temperature. Given the lack of uranium hydride oxidation rate studies, the studies of uranium oxidation might be considered to apply with the expectation that it is similar to that of uranium hydride. It has been studied by Ritchie [29], but the rate expression he provides was found to predict very little reaction at room temperature, even when considering a large specific surface area of the hydride powder (1 m^2/g).

In this work we estimated kinetic parameters by fitting the model to the experimental results. As discussed in Section 4.2.4.2, the gas composition exiting the reactor in reactor#1 injection-3 transitioned from deuterium to oxygen, and the rate of that transition provided a signature for the effective reaction rate. That is, the model showed that as the reaction rate increased, the gas

composition transition rate increased. This provided data for determining the kinetic parameters. The range of oxygen injection rates that was used in the experiments provided additional data for determining the kinetic parameters. The model showed that the temperatures created in the bed increased with the injection rate, i.e. the reaction rate increased with increasing injection rate. In the experiments that used slow injection rates, resulting in slow reaction rates, no oxygen was observed to exit the reactor (see Results section for additional explanation). This provided evidence for the minimum reaction rate. Since the collection of experiments resulted in a range of bed temperatures, the activation energy and pre-exponential factor in an Arrhenius kinetic mechanism could be individually determined, albeit crudely.

The rate expression for reaction 7 takes the form, $R_7 = f_{O2}\ UD_3\ k_{ox}\ e^{-Q/RT}$, where k_{ox} was set to 4.38 s^{-1} and Q was set to 16630 J/molK. The factor f_{O2} reflects the availability of oxygen, where it is equal to unity when oxygen is abundant, and it goes to zero if the local oxygen concentration goes to zero. Specifically, f_{O2} ramps from unity to zero as the local partial pressure of O_2 goes from 200 torr to zero. This is based on work reviewed by Ritchie, [29], that showed little dependence on the partial pressure of oxygen for pressures above 200 torr. The expression for the oxidation of uranium, R_6, is similar to R_7 where a factor of U is used in place of the factor, UD_3. The enthalpies of reaction for reactions 6 and 7 are ΔH_6 = –1085000 J/mol-U, and ΔH_7 = –957000 J/mol-UD_3, respectively (exothermic). Note that the value of the activation energy given by Ritchie is 76619 J/molK, much larger than the value used here. That large value for Q cannot explain both the complete consumption of oxygen observed in the slow oxygen injection experiments, and the rate of transition of the gas composition observed in the final, faster oxygen injection rate, experiment.

The source terms in the transport equations can now be identified. In Darcy's equation it is,

$$R = \frac{3}{2} M_{D_2} \left(R_5 + R_7 \right) - \frac{4}{3} M_{O_2} \left(R_6 + R_7 \right). \tag{21}$$

The first term accounts for the production of deuterium, on a mass concentration basis, by reactions 5 and 7. The second term accounts for the consumption of oxygen by reactions 6 and 7. The source term in the energy equation is given by,

$$Q = \sum_i \Delta H_i R_i, \tag{22}$$

where the sum is over the three reactions given in Equations (17)−(19). The source term in the oxygen transport equation is,

$$R_c = \frac{4}{3} M_{O_2} \left(-R_6 - R_7 \right). \tag{23}$$

Finally, the source terms for the solid phase conservation equations are,

$$R_{UD_3} = -R_5 - R_7, \quad R_U = R_5 - R_6, \tag{24}$$

where, here, they are expressed on a molar basis.

3.2.3 Properties

The gas is assumed to obey the ideal gas law, $p = nRT$. Solving this equation for the total molar density, n, and equating it with the sum of the molar densities of the two gas species, $c/M_c + (\rho - c)/M_{D2}$, gives an equation for the gas density as a function of pressure, temperature and composition, $\rho = M_{D2}(p/RT - c/M_c) + c$. The density of the powder bed is evaluated as, $\rho_{bed} = n_{bed} M_{bed}$, where the total molar density, $n_{bed} = ([UD_3^0] + 2[UD_3] + 2[U])/3$, and the molecular weight of the bed, $M_{bed} = \sum M_i x_i$, with the sum over all species present. Solid phase species densities are 10.95, 19.1, and 8.38 g/cm^3, for UD_3, U and U_3O_8, respectively.

Solid phase specific heats were assumed to be constant with the exception of composition effects. The specific heat of a mixture is evaluated as, $c_p = \sum x_i C_i / \sum x_i M_i$, where C_i is the specific heat per mole of species i, and c_p is the specific heat of the mixture per unit mass. Values for C_i are 49.3, 27.7 and 238 (J/molK), for UD_3, U and U_3O_8, respectively. Gas phase specific heats were obtained from temperature dependent expressions, where for O_2, c_p (J/gK) = 0.052 + 0.334log$_{10}$(T(K)), and for D_2, c_p (J/molK) = 7.07 + 0.00079 T(°C), and for the mixture, $c_p = \sum(\rho_i/\rho)c_{p\,i}$.

A temperature dependent thermal conductivity is used for the gas, independent of gas composition, and is given by the power law expression, k (W/cmK) = 0.000163 $(T/273)^{0.73}$. The thermal conductivity of a packed powder bed is known to depend less on the bulk values of the species present, and more on the thermal contact between individual particles. A constant thermal conductivity was used for the bed with a value of 0.01 W/cmK, and a value for the frits equal to the product of solid volume fraction (70%) and the conductivity of bulk stainless steel, giving 0.1 W/cmK.

The diffusivity of hydrogen in oxygen is pressure and temperature dependent as taken from [30], and is given by D (cm^2/s) = $1.25/p\ (T/400)^{1.404}$, where p is in atmospheres.

The gas viscosity was taken from White, [31], and is assumed to be temperature and composition dependent, as given by $\mu = \sum x_i \mu_i\ (T / 273)^{0.68}$, where the sum is over the two gas species present, and the base values of μ_i are 0.0001919 and 0.0001192 (g/cm s) for oxygen and deuterium, respectively.

3.2.4 Permeability

The permeability of the hydride powder bed was modeled as a function of the local Knudsen number, Kn, as described by Young et al. [32]. Their result can be expressed as,

$$K = \frac{\phi d_p^2}{\tau^2}\left(\frac{1}{32} + \frac{5}{12}Kn\right), \tag{25}$$

where ϕ is the porosity, d_p is the characteristic pore size, and τ is the characteristic tortuosity. Here, $Kn = \lambda/d_p$, where $\lambda = 1/(\sqrt{2}\,\pi\, n'\, d_m^2)$, is the gas mean free path. The same relationship was used for the permeability of the frits, but with different values for ϕ, d_p and τ. The initial porosity of the bed is based on the measured uranium loading of the reactor (assuming the material to be fully hydrided), the bulk density of the uranium hydride, and the dimensions of the bed volume in the reactor, giving $\phi^0 = 0.605$. Starting from that initial value, changes to the porosity are based on the oxide content, i.e. uranium oxide has a much smaller bulk density than uranium hydride. Consequently, conservation of mass requires that the oxide phase expands and occupies more of the bed volume, such that the porosity decreases. For example, based on the bulk densities of uranium hydride and uranium oxide, and the initial porosity, the porosity for the fully oxidized bed is $\phi^1 = 0.393$.

It is assumed that the bed maintains a mechanical equilibrium, where as oxide forms in one part of the bed, the solid phase expansion that results creates stresses that compress the remainder of the bed such that ϕ, d_p and τ remain uniform throughout the bed at all times. Then the porosity of the bed may be expressed as $\phi = 1 - (1 - \phi^0)(1+\Delta V \cdot F)$, where F is the fraction of the bed that is oxide and $\Delta V = 0.536$, is the volume expansion of the oxide phase relative to the hydride phase. The pore size and tortuosity are expressed in terms of the porosity as,

$$\frac{\phi - \phi^0}{\phi^1 - \phi^0} = \left(\frac{d_p - d_p^0}{d_p^1 - d_p^0} \right)^{n_d}, \tag{26}$$

$$\frac{\phi - \phi^0}{\phi^1 - \phi^0} = \left(\frac{\tau - \tau^0}{\tau^1 - \tau^0} \right)^{n_\tau}, \tag{27}$$

where the superscripts 0 and 1 placed on ϕ, d_p and τ denote values corresponding to $F = 0$ and $F = 1$, respectively. The pore size and tortuosity corresponding to these two extremes were determined by fitting the model to results from flow-through experiments, where deuterium stored in a small vessel is allowed to flow through the bed and exhaust to a vacuum pump. The pressure decay in the deuterium vessel reflects the permeability of the bed, i.e. as the permeability decreases so does the rate of pressure decay. These flow-through experiments were conducted after loading and hydriding the bed, and after the bed was fully oxidized. Based on these two experiments, values for d_p and τ for the hydride and oxide states were determined by using the model to simulate the flow-through experiments and fitting it to the experimental data. Similarly, flow-through experiments were conducted for the case where only the frits were present in the reactor to determine the pore size and tortuosity for the frits. The results for the bed are, $\phi^0 = 0.605$, $d_p^0 = 1.9\times10^{-4}$ cm, $\tau^0 = 1.693$, $\phi^1 = 0.393$, $d_p^1 = 0.7\times10^{-4}$ (cm), and $\tau^1 = 2.16$. The values for the frits are, $\phi = 0.3$, $d_p = 7.5\times10^{-4}$ cm and $\tau = 1.85$. Note that this constitutes a reduction in permeability of almost a factor of 20 due to the transition from the initial hydrided state to the fully oxidized state.

Flow-through experiments were also conducted after the first and second oxygen injection experiments, where the bed was a mixture of hydride and oxide phases. The measurements from

these experiments were compared to the calculated results to help guide the selection of the exponents n_d and n_τ appearing in Equations 9 and 10, where the results are 2 and 1, respectively.

3.2.5 The finite element model

The governing equations described above were solved using the finite element method. The finite element model of the reactor is shown in Figure 13. It includes the oxygen source bottle, the flow channel connecting it to the hydride bed, the two frits that prevent the powder hydride material from leaving the reactor, a short length of the flow channel allowing gases to exit the bed, and the reactor wall enclosing the hydride material. The reactor housing is stainless steel. Two thermocouples were attached to the outer surface of the reactor wall in the experiments, as shown in the figure. TC#1 was located upstream of the hydride bed, where gas flows upward through the reactor for the orientation shown in Figure 1. TC#2 was located downstream of the hydride material. The temperatures predicted by the model at these locations were compared to the measured results from the experiments. There is substantially more hardware attached to the reactor for fixturing and gas handling purposes in the experiments than represented by this model. This extra hardware creates additional heat sinking to the reactor. Its effect on the thermal response in the model was approximately accounted for through the use of temperature boundary conditions as described below.

The experiments were carried out by storing oxygen at an elevated pressure in a small vessel, and then allowing this oxygen to flow through the reactor. As it does, the pressure in the small vessel decreases such that the flow rate is a maximum at the beginning and monotonically decreases with time. The simulations of the experiments are carried out in the same way, the part of the model representing the small vessel is initially prescribed to contain pure oxygen at elevated pressure, and as the oxygen flows through the reactor the pressure in the small vessel and the flow rate through the reactor decrease with time. The gas in the small vessel is assumed to be isothermal.

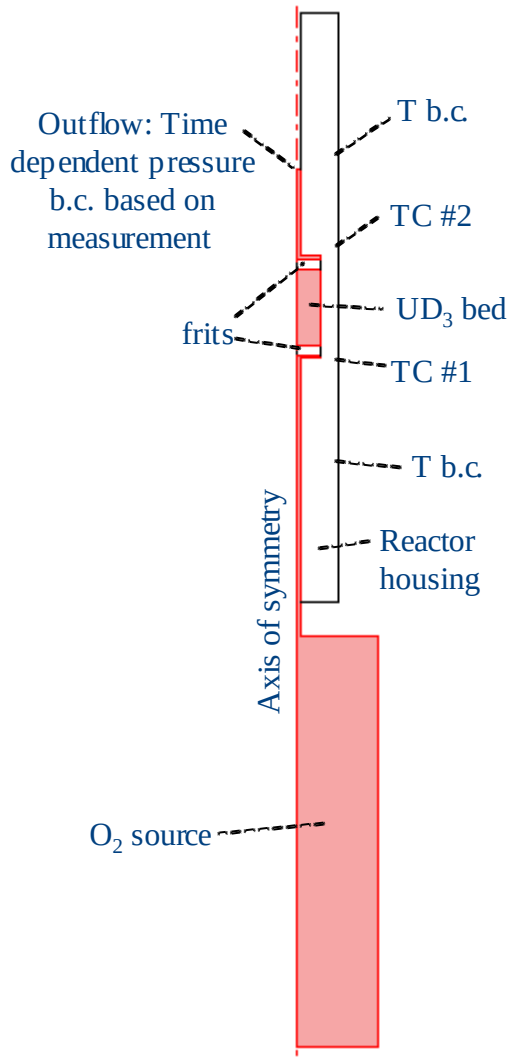

Figure 13: An axisymmetric finite element model of the reactor.

3.2.5.1 Initial conditions

The oxygen source vessel is given an initial gas composition of pure oxygen and a pressure corresponding to the experiment to be simulated. This varied from 20 to 171 psia, depending on the experiment. The gas composition in the reactor is prescribed to be pure deuterium. The initial temperature was approximately of room value. The reactor was loaded with 0.01193 moles (2.84 g) of uranium where the distance between the frits was 1.328 cm and the internal diameter of the reactor was 0.8 cm. After several hydriding/dehydriding cycles (using D_2) the uranium was converted to a fine powder of uranium deuteride resulting in an initial UD_3 density of 0.0178 mol/cm^3.

3.2.5.2 Boundary conditions

The boundary conditions for Darcy's equation are that: the reactor walls are impermeable, there is symmetry at the axis of the reactor, and there is a time dependent pressure specification at the outlet to the reactor, as shown in Figure 13. This time dependent pressure boundary condition is based on measurements taken during the experiments. Contact heat flux boundary conditions were applied to small regions (0.1 cm long) of the outer reactor wall, as shown in Figure 1, corresponding to where gas tight seals were made in the experiments. The heat flux was given by, $q = h_{contact}(T - T_{seal})$, where $h_{contact}$ = 0.2 W/cm^{2}K. The "seal" temperatures were not equal (28 and 39°C, at the upstream and downstream locations, respectively) such that a small temperature gradient was established in the reactor as the initial condition. This is due to the elevated temperature that was maintained in the downstream hardware during the experiments to prevent condensation. Adiabatic boundary conditions were applied to the lateral surfaces of the reactor wall. While in reality there are heat losses to the environment, these losses are small compared to the heat conducted into surfaces where the contact heat flux boundary conditions are applied. The boundary conditions on the oxygen transport equation are that the reactor walls are impermeable and there is a zero concentration gradient at the outlet.

3.2.5.3 Solution of the equations

The equations were solved using the commercial software, COMSOL. The energy equation was solved in steady state form to establish the initial temperature distribution. Then all equations were solved in transient form.

4 EXPERIMENTAL RESULTS AND DISCUSSION

4.1 Experimental plan

We seek to determine if the UH_3+O_2 reaction can be used to make a reactor system that will rapidly generate hydrogen gas with no unwanted gaseous byproducts. Few relevant data are available and there is relatively minimal research in this regard using uranium; hence this project began with simple experiments.

Having selected a reactor size and geometry that minimizes uranium mass while allowing reliable measurements, the experimental apparatus was built. After shake-down tests with surrogate powders built confidence in the test procedure and eliminated procedural and/or apparatus bugs, the uranium experiments were initiated as follows.

1) Do the first tests with uranium to work though an experimental iteration; from loading to disposal with surveying.
   a) Prepare the first reactors. The questions to be answered are:
      i) Will U hydride to UH_3? Is the H_2 gas supply clean enough to not inhibit UH_3 formation? Can stoichiometric uptake be measured?
      ii) What are the bed characteristics after hydriding? Radiography and flow tests will characterize the bed.
      iii) How precisely will reactors be made? Can two be made sufficiently similar to ensure repeatability and make valid comparisons between reactors?
   b) Perform one or two oxygen injection tests on the first UH_3 beds with the bed initially at ambient temperature to determine:
      i) Qualitatively, what will happen when oxygen is injected?
         (a) Will the initial rate of reaction be so slow that the O_2 passes though the bed without reacting? Preliminary numerical modeling suggests that this may happen if UH_3+O_2 kinetics are assumed identical to U+O_2 kinetics.
         (b) Will the reaction start quickly, but rapidly slow due to surface oxide passivation? This is what one would expect based on UH_3+air reaction literature.
         (c) Will the reaction start quickly and oxidize the UH_3 to completion? Will this release so much heat that the bed melts or clogs?
      ii) What are the post-test bed characteristics? Will it be fully or partially clogged? Will the post-decomposition U powder have retracted/shrunk from the reactor wall?
      iii) How can the bed be made inert after the test? Can any remaining un-reacted U and/or UH_3 be fully oxidized to UO_2 and/or U_3O_8?
      iv) Are the grade-1 (1-μm-rated) frits sufficient containment for the uranium powders? Which parts of the reactor assembly are reusable?
      v) How easy is it to dispose of a spent reactor?
2) Using what was learned in Step 1, more focused experiments will be designed to understand reactor failure/operating modes.

At the outset it was difficult to plan beyond the "what is going to happen" tests. However, the key questions to be answered are:

1) What are the kinetics of the UH_3+O_2 reaction over an initial bed temperature range of −60°C to 210°C? Are the kinetics:
   a) Fast enough to locally oxidize the bed and allow design of a flow-through reactor?
   b) Slow enough to inject and distribute the entire charge of oxygen before significant portions of the bed react? This would be suitable for a single-ended, huff-and-puff-style reactor.
2) Depending on what the kinetics are, can the reaction and heat generation be managed to yield sufficiently pure and controlled H_2?

Upon answering the preceding questions, we will know if the UH_3+O_2 system could possibly work.

We were not able to quantitatively measure UH_3+O_2 reaction kinetics using our experimental setup, primarily because the reaction is so strongly exothermic. However, we demonstrated qualitatively that the reaction is fast enough, even at −80°C, to locally oxidize/react the bed such that it could be used as a flow-through reactor. The sections below describe the experiments in detail.

In addition to the oxygen injection tests, hydrogen-deuterium isotope exchange experiments were conducted at 25, 100, and 250°C. Because the isotope exchange reaction is much less exothermic, the exchange kinetics are more easily quantified.

It was discovered that hydrogen isotope diffusion in the uranium hydride particles limits the overall gas-to-solid isotope exchange rate. In addition, a set of high quality experimental data was generated. This data can be analyzed with a bed exchange and transport model to infer effective intra-particle diffusion coefficients. It appears that, at 250 °C, isotope exchange may be fast enough to design an effective hydrogen isotope separation system.

4.2 Reactor #1 – slow O_2 injection

Reactor #1 established the preparation process; slow O_2 injections demonstrated that:

- UD_3+O_2 is faster than U+O_2
- UD_3 reacts completely to U_3O_8 with no passivation
- The reaction front is sharp (no surprise) and pretty flat (more of a surprise)
- The bed mechanically evolves due to $UD_3 \rightarrow U_3O_8$ particle expansion

4.2.1 Bed preparation

4.2.1.1 Uranium material

The uranium used in all reactors is from the same 25-g piece of 99.975% pure uranium metal supplied by the National Bureau of Standards (standard reference material 960) and used without further chemical treatment (e.g., no etching of the sample with aqueous HNO_3 to remove the surface oxide as suggested in SRM-960's material certificate).

The entire 0.47×0.47×15.24-cm^3 uranium rod was cut into approximately 0.635- to 0.965–cm-long pieces using a heavy-duty cable cutter supplied by McMaster Carr (part number 39615A72)[3]. To prevent the spread of radioactive contamination, the cutting operation was performed inside an air-filled glove-bag in a dedicated work area. The cut-pieces were weighed on a 0.01-g-resolution portable scale (±0.01-g accuracy), grouped into 2.7−2.9-g samples, and placed in plastic bags. The packages were stored in a desiccated dry box until they were loaded into a reactor.

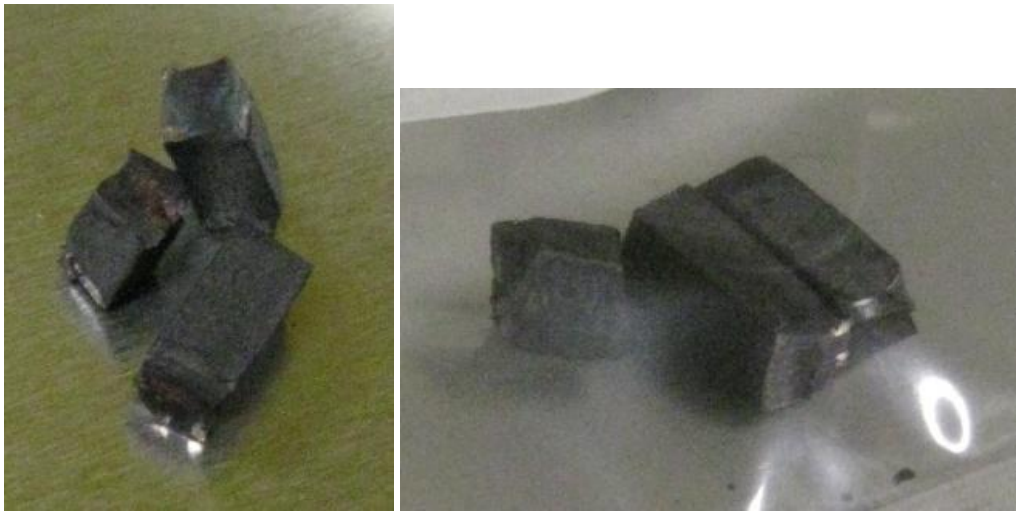

Figure 14: Uranium pieces 30 minutes after cutting (left) and after 20 days of storage in a dry box (right). In the right photo, the pieces are inside a plastic bag. The pieces in the right photo weigh 2.84 g and were used in Reactor #1. The material's dark color is due to the surface oxide.

4.2.1.2 Reactor loading and processing

Before loading into a reactor, the uranium pieces were weighed a second time and then placed into the reactor tube upon which the top frit was pressed into place. The frit locations were measured using 0.0254-mm (0.001-in) -resolution dial calipers and the bed length was computed from the measurements. The spacers were then screwed into the ends of the reactor tube to support the frits and lock them in place. After this, the 9/16-in (1.429-cm) medium-pressure-to-M250C-adapters were installed followed by the reactor valves. After the reactor assembly was assembled, external contamination surveys were used to confirm that the system was safe to remove from the uranium work area.

4.2.1.3 Activation

Because air-exposed uranium has a surface oxide coating, vacuum-thermal activation is required to defeat the oxide layer so that the metal will react readily with H_2 [8]. Based on work by Heung [33] and Powell [15], activation conditions were 300°C for 3 hours in a vacuum (~100 mtorr).

[3] Uranium, even as a pure metal, is fairly hard, similar in shear strength to 1040 carbon-steel.

Reactor 1 activation data were not captured; however, Figure 15 shows RGA data from Reactor 3, which is expected to be similar to all reactors.

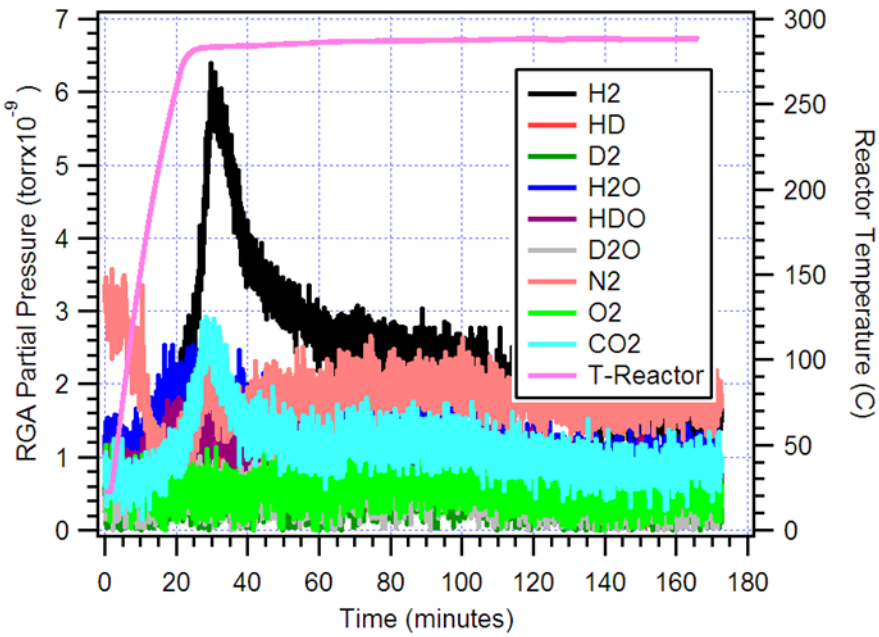

Figure 15: Reactor temperature and RGA partial pressures during Reactor 3 activation.

As the reactor heats from 25 to 290 °C, the evolving gas changes from N_2 (residual air) to H_2O (adsorbed water), followed by CO_2 and H_2. The H_2 is likely coming from the uranium. It is known that uranium will form both oxide and hydride species when reacting with moist air (in storage). There is less certainty about the origin of the CO_2; it is possible that carbon impurities in the uranium are reacting with the oxide, reducing the oxide, and forming CO_2. However, this seems like a large amount of CO_2 to be generated by 99.975% pure uranium metal. It's also possible that this signal (m/e = 44) is a cracking product from a heavier molecule. Regardless, after this activation step, the uranium metal readily reacts with D_2.

4.2.1.4 First hydride

The kinetics of hydriding massive uranium metal have been studied extensively. Following Powell [15], 250 °C was the hydriding temperature. There are 2 known forms of UH_3, α-UH_3 and β-UH_3. By hydriding at 250 °C, 100% β-UH_3 should be formed (α-UH_3 forms at ambient to sub-ambient temperatures) [34].

Hydriding was performed immediately after activation. The valve to the reactor was closed and the ~150-cm^3 receiver volume was filled with enough D_2 to completely react the uranium to UD_3 with 30 psia (0.21 MPa) of D_2 remaining in the system afterwards. Deuterium uptake was tracked using a PVT mass balance. The D_2 gas missing from this closed system is assumed to have formed UD_3. Figure 16 shows the computed D/U atomic ratio during hydriding.

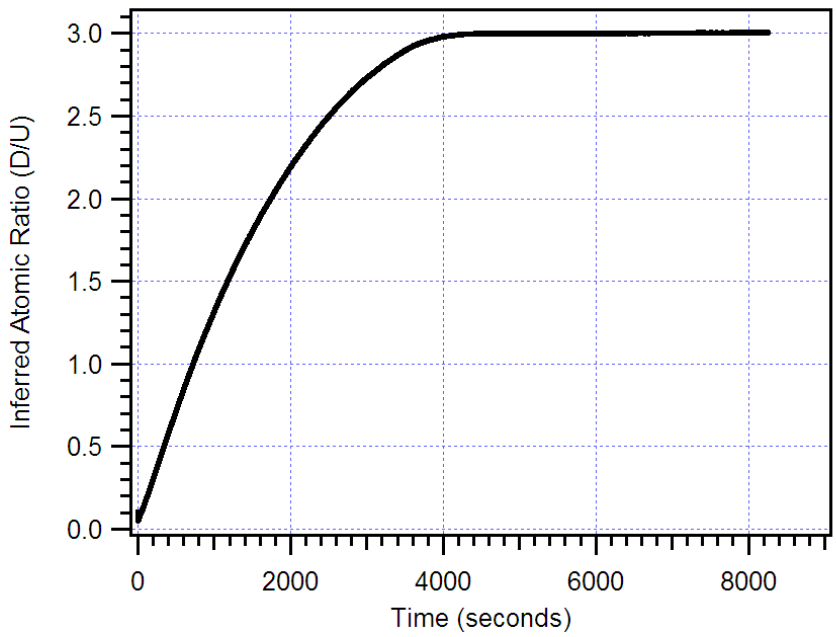

Figure 16: Hydride reaction progression for Reactor 1. The uranium reached D/U = 3 in approximately 1.2 hours.

The uranium absorbed D_2 at a faster-than-expected rate. Models by Bloch [35] and Condon [14] predict that hydriding should take between 3 and 13 hours. For all four reactors, hydriding was completed in approximately 1.2 hours. This disagreement between model and experiment is not unexpected; uranium's hydriding rate is sensitive to the metal's condition (e.g., extent of cold-work, impurity elements, mass and surface area) [35].

4.2.1.5 Flow testing

The bed was flow-tested with D_2 after hydriding. The 150-cm^3 receiver vessel and reactor were filled with D_2 at 90 psia (0.62 MPa). Then, with the vacuum pump actively evacuating the O2Volume vacuum port, AO1 was opened. Deuterium was allowed to flow through the reactor until the pressure in the 150-cm^3 vessel reached 30 psia (0.21 MPa), at which point the air-operated valve was closed. Source volume pressure and temperature were recorded along with the pressures upstream and downstream of the reactor. These data were used to compute the dusty gas model (DGM) flow parameters for the bed (permeability, B, and molecular flow coefficient, K_0).

The flow parameters were computed using a steady-state DGM model [36]. For steady flow of a pure ideal gas through a uniform-temperature bed with uniform properties, the molar flow rate is,

$$\frac{\dot{n}}{A_C} = \frac{D^K}{RTL_C}\left(P_1 - P_2\right) + \frac{B}{2\mu RTL_C}\left(P_1^2 - P_2^2\right), \tag{28}$$

where P_1 and P_2 are the upstream and downstream pressures, μ is gas viscosity, R is the gas constant, and L_C is the bed length. This can be rearranged into a more useful form by noting that $\left(P_1^2 - P_2^2\right) = \left(P_1 + P_2\right)\left(P_1 - P_2\right)$ and defining $P_{AVG} = \frac{1}{2}\left(P_1 + P_2\right)$ and $\Delta P = P_1 - P_2$. This yields,

$$\frac{\dot{n}}{A_C} = \frac{\Delta P}{RTL_C}\left(D^K + \frac{BP_{AVG}}{\mu}\right), \tag{29}$$

which relates the molar flow rate to the pressure differential. The pressure drop across the bed is proportional to the molar flux, $\dot{n}/A_C$, and the bed thickness, L_C. The internal structure of the bed is parameterized by the effective permeability, B, and the effective molecular flow coefficient, K_0. The Knudsen diffusion coefficient, D^K, is related to K_0 according to

$$D^K = \frac{4}{3} K_0 \sqrt{\frac{8RT}{\pi M}}, \tag{30}$$

where M is the molecular mass of the flowing gas.

To determine the DGM parameters, the molar flow rate was computed from the molar depletion rate of the 150-cm^3 vessel. Combining the measured upstream and downstream pressures, bed geometry, bed temperature, and gas viscosity facilitates plotting $\frac{\dot{n}RTL_C}{A_C \Delta P}$ against P_{AVG}. Parameters B and D^K are estimated through linear least-squares regression.

The measured pressure drop across the reactor comprises the pressure drop across the frit-bed-frit system. To more accurately measure the true flow characteristics of the bed, the calculations must consider the pressure drops across the frits. Flow tests on frits alone yield DGM parameters of $B_{\mathrm{frit}} = 1.73\times10^{-13}$ m^2 and $K_{0,\mathrm{frit}} = 1.15\times10^{-7}$ m for 0.157-cm-thick, 0.8-cm-diameter frits.

Figure 17 shows the measured reactor upstream/downstream pressures and the computed pressures at the frit-bed interfaces during a typical flow test. The frit pressure drop correction is relatively small, but not negligible.

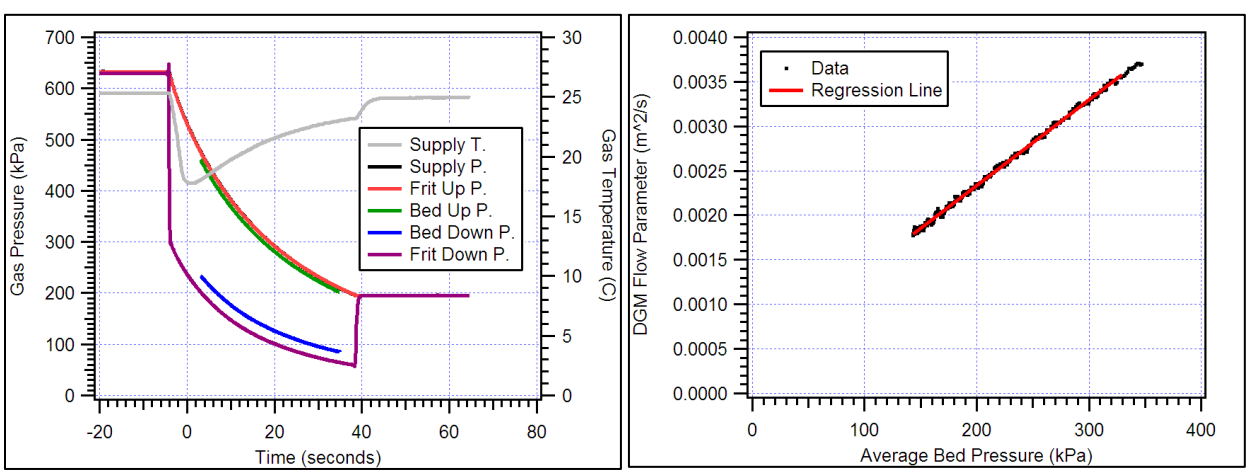

Figure 17: Flow test data and DGM parameter plot for Reactor #1 after the initial hydride. The DGM parameter is calculated using the frit-corrected pressures just upstream and downstream from the porous bed.

For all reactors, $\frac{\dot{n}RTL_C}{A_C \Delta P}$ varied linearly with P_{AVG}, as predicted by the theory. However, the values of B and K_0 calculated from the data in Figure 17 suggest that the bed was not uniformly dense after the first hydride cycle; because B and K_0 were both higher than predicted by accepted correlations, [36], assuming specific surface area S_m = 1.0 m^2/g and porosity ϕ = 0.60. In a nonuniform bed, the local B and K_0 increase more in regions of higher porosity than they decrease in lower porosity regions. Therefore, the effective bed B and K_0 is expected to increase as the degree of bed nonuniformity increases.

An initially nonuniform porosity is expected because the bed started as large chunks of uranium metal, which decrepitated to form ~1.0-m^2/g UD_3 powder (see Figure 18).

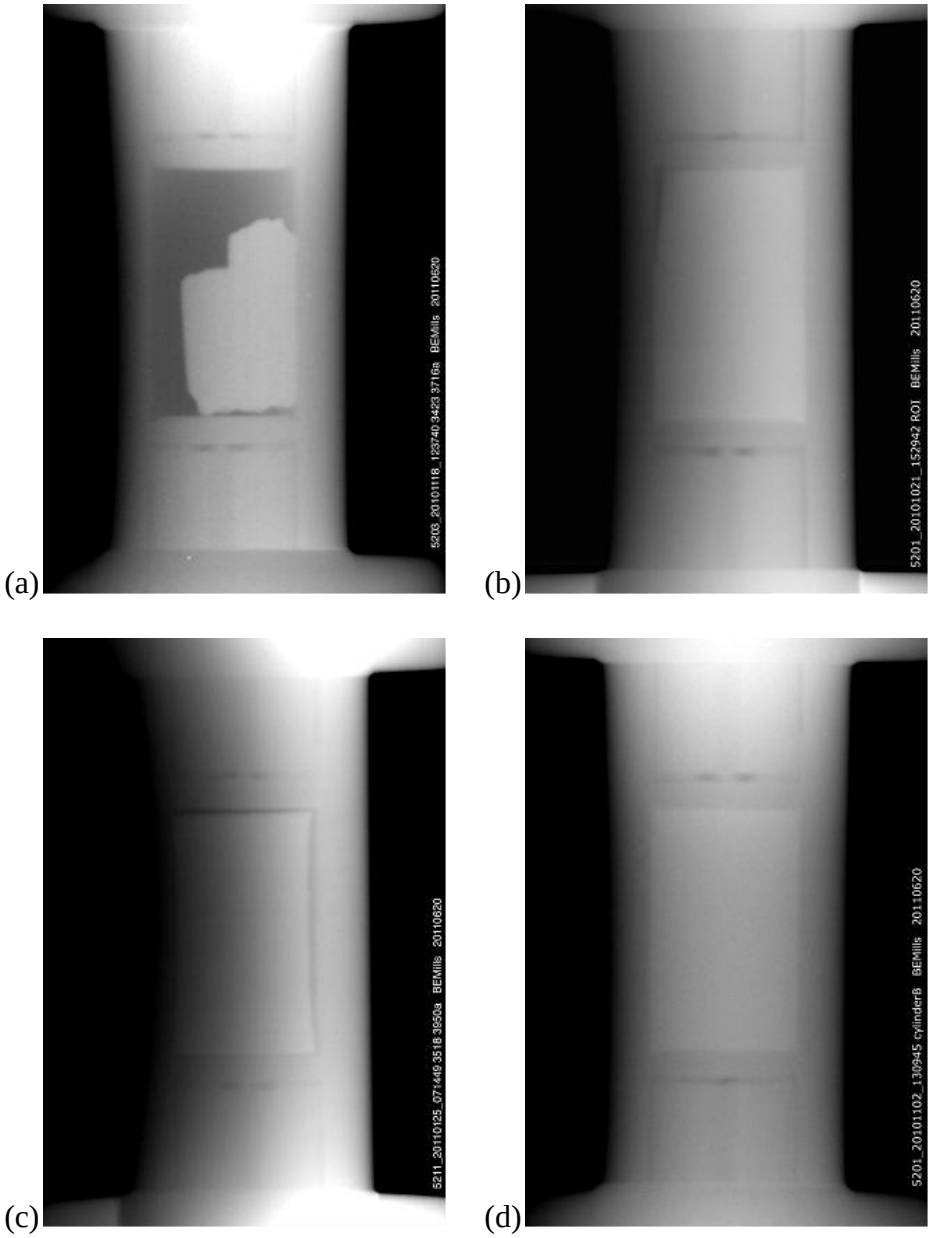

Figure 18: Radiographs of reactors during processing. (a) Reactor #2 filled with two chunks of uranium metal. (b) Reactor #1 after the first hydride cycle. (c) Reactor #2 after dehydriding (between hydrides 6 and 7). (d) Reactor #1 after the second hydride cycle.

Figure 18 affords a more thorough appreciation for the process. Because uranium decrepitates into a fine powder, significant material rearrangement is required to go from solid chunks to a 40%-dense packed-powder bed. Rearrangement is incomplete after the first hydride cycle. The top-right radiograph shows a region of lower density in the bed's upper left corner. However, the beds become much more uniform after repeated cycles of dehydriding and hydriding. Figure 18 provides evidence for this; the bottom-right radiograph is Reactor #1 after the second hydride cycle. The low-density region in the top-left corner of the bed is no longer apparent. The flow

test results are consistent with these radiographs; flow tests were conducted after each hydride cycle and the reactors, which have similar porosities, converge to similar flow parameters.

Figure 19 demonstrates how the measured DGM parameters converge; the effective DGM flow parameters are compared with values predicted by Meyer's correlations [36-37]. Due to variations in uranium loading and bed length, Reactors 1, 2, 3, and 4 have slightly different porosities. The bed parameters are summarized in Table 1.

Table 1: Reactor bed parameters

Reactor	Uranium load (g)	Bed Diameter (in)	Bed Length (in)	Porosity (n/a)
1	2.84	0.316	0.517	0.605
2	2.85	0.316	0.526	0.610
3	2.75	0.316	0.500	0.604
4	2.78	0.316	0.471	0.575

The bed length and porosity vary slightly, however, in all cases, the UD_3 powder surface area is assumed to be 1.0 m^2/g. To avoid confounding the reactor-to-reactor comparison with porosity-induced changes in the DGM properties, ratios of measured/predicted values are presented in Figure 19.

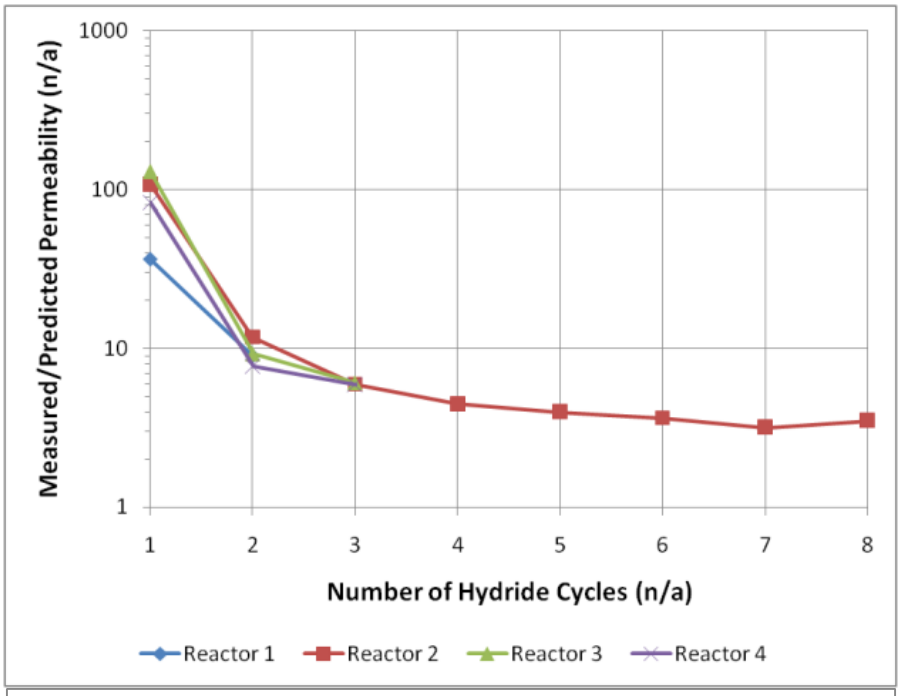
Measured/Predicted Permeability (n/a)
1000
100
10
1
1
2
3
4
5
6
7
8
Number of Hydride Cycles (n/a)
Reactor 1
Reactor 2
Reactor 3
Reactor 4

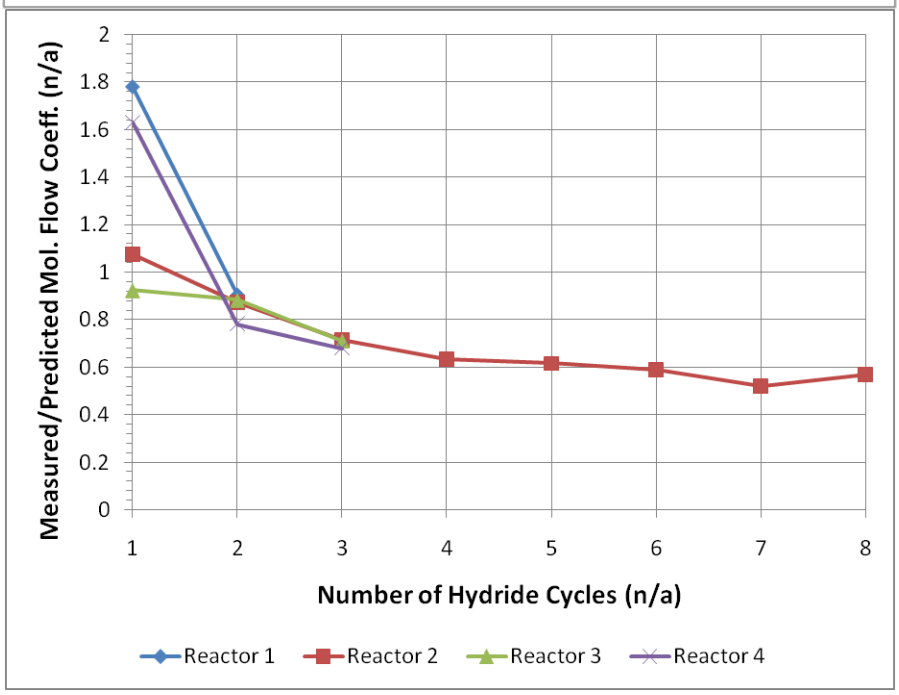
Measured/Predicted Mol. Flow Coeff. (n/a)
2
1.8
1.6
1.4
1.2
1
0.8
0.6
0.4
0.2
0
1
2
3
4
5
6
7
8
Number of Hydride Cycles (n/a)
Reactor 1
Reactor 2
Reactor 3
Reactor 4

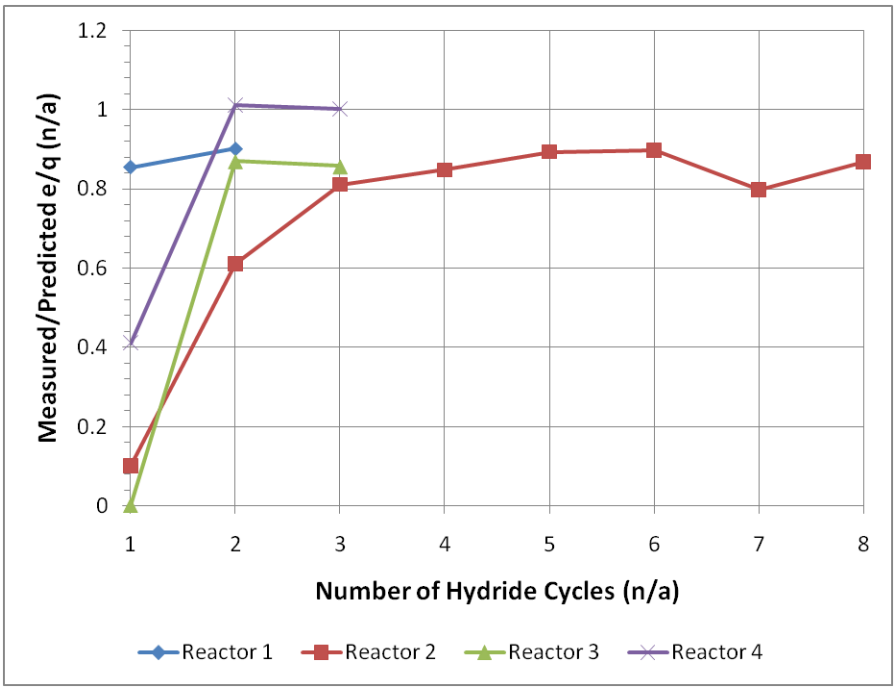

Figure 19: Effective DGM flow parameters for Reactors #1−4. Measured/predicted ratios of effective permeability (log-scale), molecular flow coefficient, and porosity/tortuosity ratio are shown.

After the first hydride cycle, the spread between reactors is large because each started with different uranium metal chunk configurations. The spread in porosity, *B*, is larger than that for the effective molecular flow coefficient, K_0; because *B* is most strongly affected by bed non-uniformity [26]. However, disparities quickly decrease as the number of hydride cycles increase, because the bed loses memory of its starting configuration.

After three cycles the beds are effectively uniform. It would be unlikely that the four reactors, each of which started with differently sized, shaped, and distributed uranium chunks, would end up with comparable *B*, K_0, and effective porosity to tortuosity ratios, *e*/*q*, if the beds were non-uniform.

In addition, *B*, K_0, and *e*/*q* are in reasonable agreement with the values predicted from Meyer's correlations [36]. This suggests that much, if not all, of the powder's 1.0 m^2/g surface area is exposed to gas flow. If less of the BET-derived surface area were exposed to flowing gas, for example because the particles had significant internal porosity, then the scaling relationship between BET surface area and flow channel diameter that is inherent in Meyer's correlations, derived from measurements on media with relatively smooth non-porous particles [36-37], would not be obeyed and our measured *B* and K_0 would be significantly higher than predicted. The permeability, *B*, is higher and K_0 is lower than Meyer's predictions. The disagreements however, are reasonably small and therefore not cause for concern. Particle morphology is discussed is more detail following the hydride cycling section.

4.2.1.6 Hydride cycling

Reactor #1 underwent two hydride cycles before performing the oxygen injection tests. Between hydride cycles, the bed was dehydrided at 400°C, for 2 hours, under dynamic vacuum (~1 mtorr). These conditions were selected based on the isothermal decomposition model of Lindner [27]. On subsequently tested Reactors #2−4, decomposition was monitored with the RGA. Figure 20 is a representative data set of the partial pressures and temperatures during dehydriding.

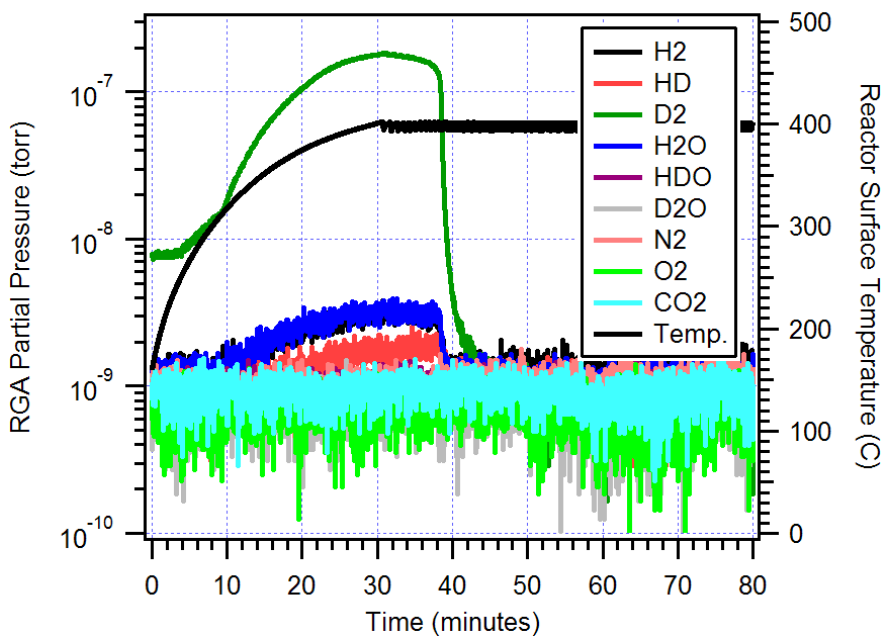

Figure 20: RGA partial pressures and reactor temperature during the second dehydride cycle of Reactor #2. These data are representative of all dehydride cycles in all experiments.

The drop in D_2 signal at approximately 40 minutes indicates that decomposition is complete. This took significantly less time than predicted by Lindner's model; most likely because the vacuum in the bed is less than was assumed for the model calculation (1 mtorr). This would cause the bed to decompose more quickly. Lindner's model predicts that decomposition rate increases with $\ln(P/P_0)$, where P_0 is the equilibrium decomposition pressure and P is the gas pressure above the hydride.

Due to increased surface area, hydriding of the post-decomposition uranium powder was significantly faster than the initial hydriding of the uranium metal chunks. For example, during the second hydride, Reactor #1's bed reached D/U of 2.97 in ~2 minutes (other reactors achieved full hydride stoichiometry in similar times).

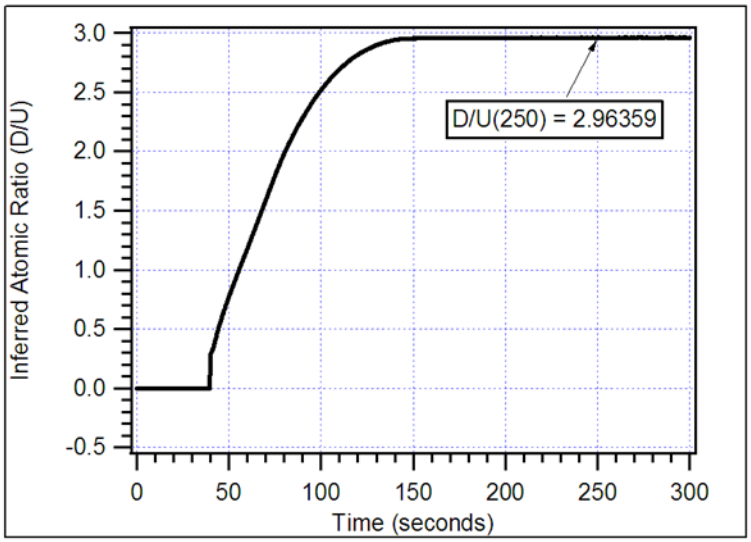

Figure 21: Hydride reaction progression for Reactor #1 during the second hydride; the uranium reached D/U = 2.96 in approximately 2 minutes.

4.2.1.7 Powder morphology

Understanding the reactivity of uranium hydride powder requires knowledge of the morphology, surface area, particle size, and particle structure. Fortunately, uranium hydride has been studied extensively and reference data are available. Uranium metal decrepitates into a fine powder upon hydriding. There is also evidence that, if the uranium pieces/particles are larger than about 50 μm, the fineness of the hydride powder is more-or-less independent of the initial metal particle size. Finally, it is well established that the hydride powder specific surface area increases with the number of hydride/dehydride cycles [14, 38].

SEM are available for uranium hydride and uranium metal powders during cyclic hydride-dehydriding. Because both the hydride and uranium metal powders are air-sensitive, the SEM samples must be prepared and imaged in an oxygen- and water-free environment to obtain representative images.

In a recent publication, Bloch [39] shows SEM micrographs of U with 0.1 wt% Cr material (presumably in the dehydrided condition) after approximately 50 hydride-dehydride cycles. The micrograph shows a complicated structure with non-spherical, needle like, particles between 0.1 and 1 μm thick. Unfortunately, Bloch's powder was exposed to air for several hours before imaging and is likely a mixture of unreacted metal and uranium oxides. These images are not likely to be representative of our materials.

Condon and Larson [14] also provide an SEM image of uranium powder. The authors were careful to control gas purities and limit contamination during their ultra-high vacuum hydriding/dehydriding tests. In addition to studying hydriding kinetics, they measured the powder surface area using argon BET. Unfortunately, they do not indicate whether the 0.8-m^2/g uranium powder sample shown in SEM image (Figure 22) was air-exposed. Considering the care

with which Condon and Larson conducted their experiments, we speculate that the SEM-sample in Figure 22 was not exposed to air and is therefore representative of our materials.

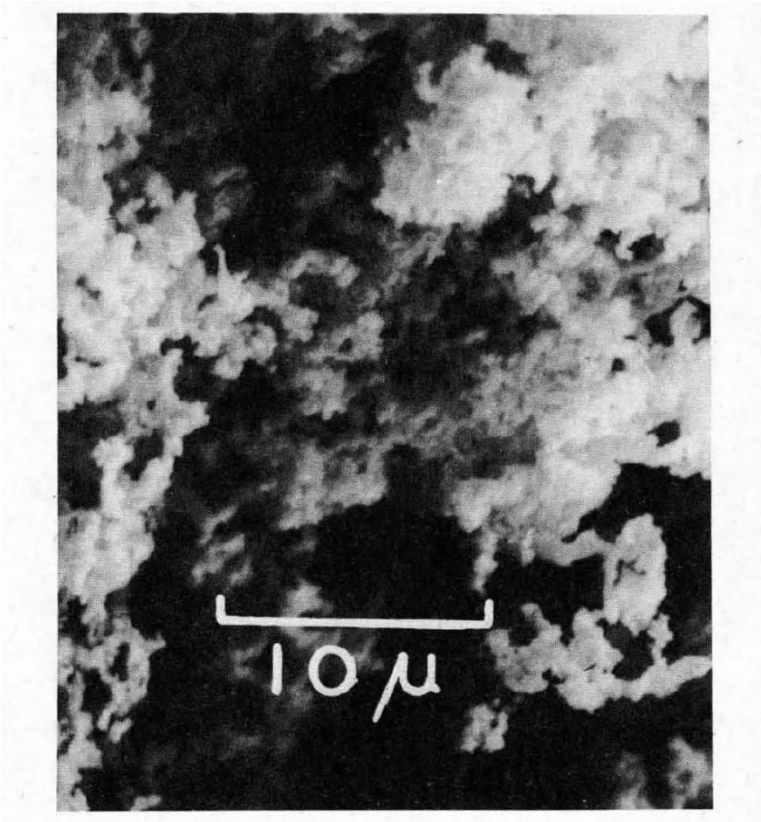

Figure 22: SEM micrograph of 0.8 m^2/g uranium powder [14]. The specific surface area indicates that the sample likely underwent two hydride/dehydride cycles.

Figure 22 shows what appear to be 10-μm aggregates of <1-μm particles. This is consistent with the BET-measured specific surface area, which yields a 0.4-μm equivalent solid-sphere diameter. If the uranium particles hydride without further decrepitating, they would produce 0.5-μm equivalent solid-sphere hydride particles[4].

Le Gyuadec et al. [5] included an SEM image (see Figure 23) in a recent study of the pyrophoricity of U and UH_3 powders. Their hydride was prepared in an argon glovebox and protected from water, oxygen, and air contamination prior to SEM imaging. The uranium (of unspecified purity) started as ~1-mm chunks; and only one hydride cycle was performed before imaging. There is a broad particle size distribution comprising ~100-μm aggregates of particles as small as 1 μm. No specific surface area was reported. These are the best available images of uranium hydride powder, however, they are not likely to be representative of our powder, which underwent multiple hydride/dehydride cycles.

[4] This is easily computed from the known densities and molecular weights of uranium and uranium hydride. Because the hydride is less dense, the uranium spheres should get 52% larger by volume when hydrided.

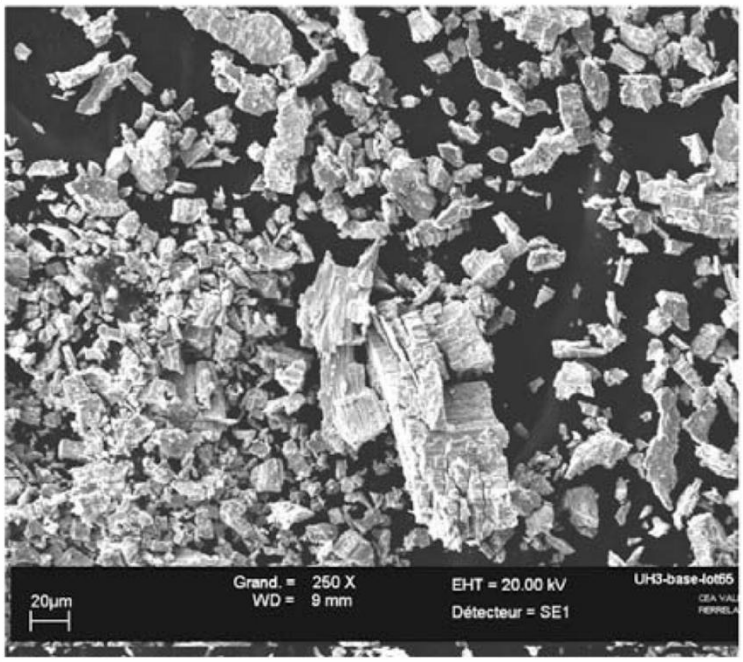

Figure 23: SEM image of uranium hydride powder [5].

Images of uranium hydride powders that are similar to our materials are available in an unpublished document and are reprinted in Figure 24. SEM images of uranium and uranium tritide were taken in a dedicated SEM facility for radioactive and pyrophoric materials at Mound laboratory [40]. The specially constructed facility housed an SEM and sample preparation equipment inside a large argon glovebox. Due to the hazards involved with manipulating UT_3 powders, the atmosphere was controlled and that no air or water contamination was introduced.

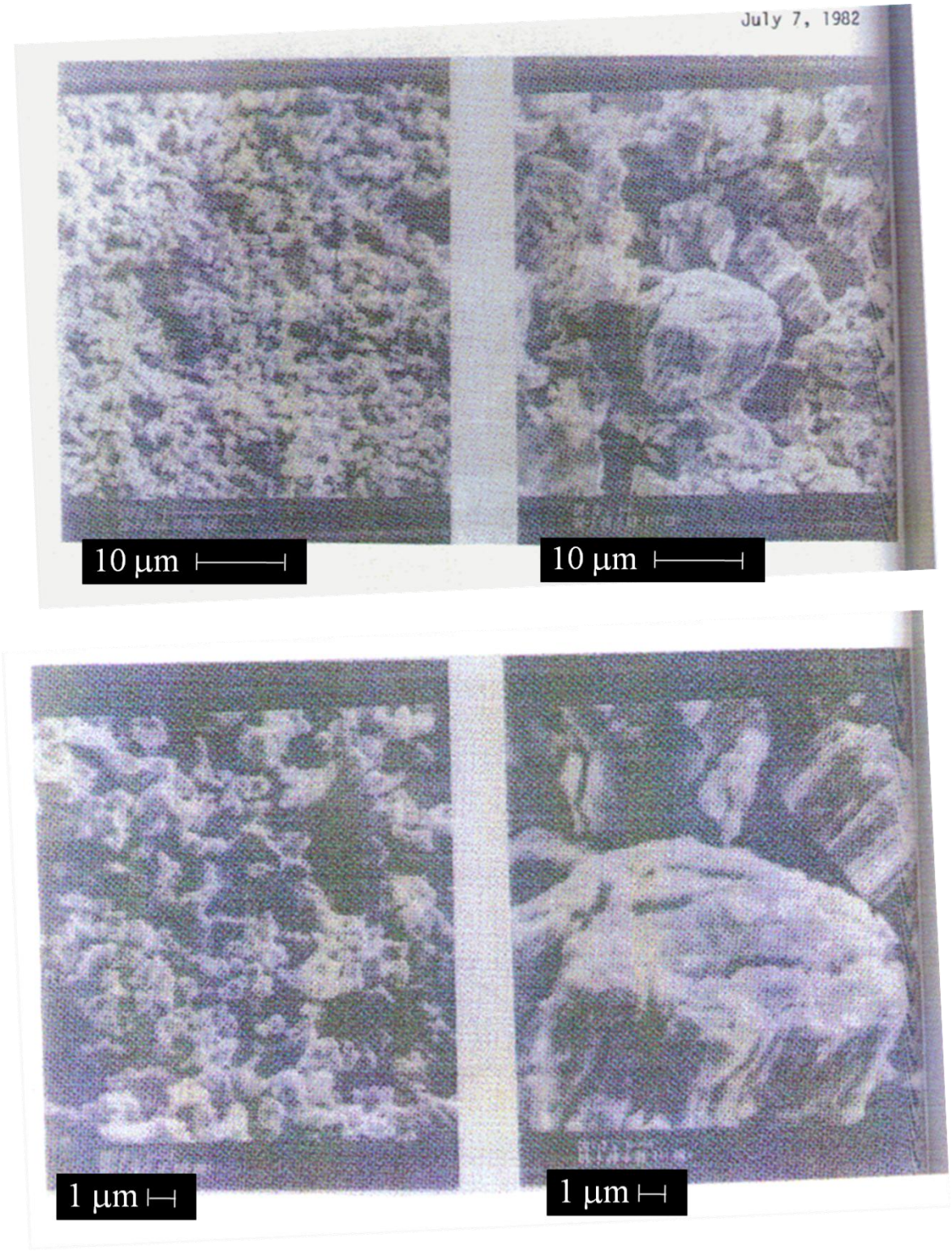

Figure 24: SEM images of UT_3 powders [41]. Samples began as ~ 20-μm spherical uranium particles. Each row is at an equal magnification. The left column is UT_3 powder after 5 hydride/dehydride cycles; the right column is UT_3 powder after a single hydride cycle.

The single-hydride sample in Figure 24 shows similarities to the single-hydride sample of Figure 23. Both images show large, cracked particles and a broad particle size distribution. Large hydride aggregates are absent in Figure 24 because the sample began as ~20-µm uranium spheres.

This morphology is rather different from the sample subjected to 5 hydride/dehydride cycles. The cycled sample, left column of Figure 24, reveals solid particles with a fairly narrow size distribution. From the images, the mean particle size is about 0.5 µm. The powder in all of our reactors was treated with at least two hydride/dehydride cycles and is expected to have similar morphology.

These visual observations are in reasonable agreement with BET-measured surface areas. A collection of 0.5-µm monodisperse solid spherical hydride particles would have a BET surface area of 1.0 m^2/g (as the hydride). If the hydride were decomposed to uranium metal without further decrepitation, then the surface area of the resultant uranium powder would be 0.6 m^2/g.

Figure 25 shows BET results from other researchers. Although somewhat different from the specific surface areas reported by Stakebake [38] (0.9 m^2/g after five cycles) and Condon and Larson [14] (1.6 m^2/g after five cycles), our approximation of 1 m^2/g for UH_3 is not unreasonable.

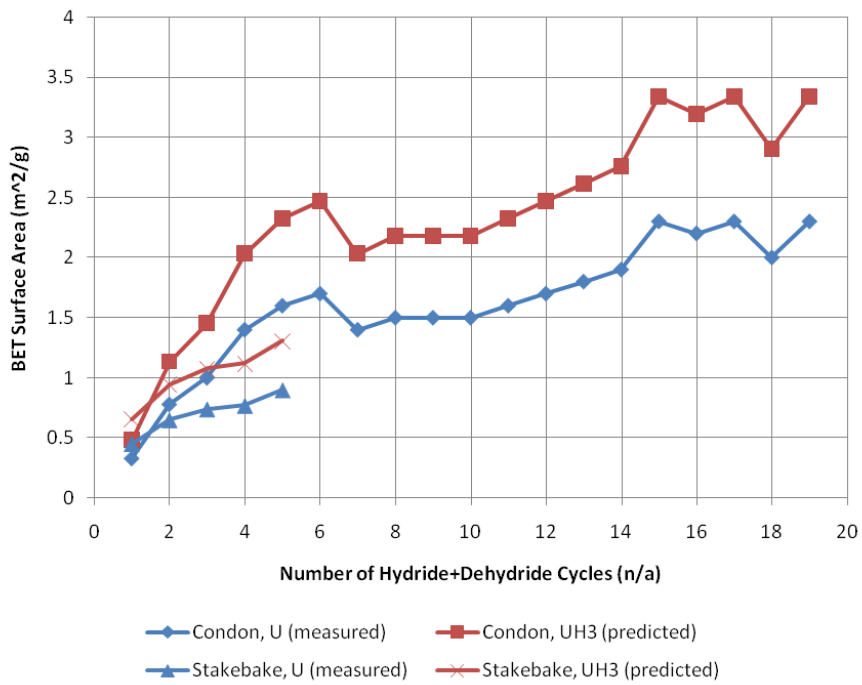

Figure 25: U and UH_3 BET surface area vs. hydride/dehydride cycles.

The hydride powder in our experimental beds can be modeled as 0.5-µm monodisperse solid spherical particles with a specific surface area of 1.0 m^2/g. To a first approximation, particle size distribution effects can be neglected.

4.2.2 O_2 injection-1

The goal for injection-1 was to test the assumption that at 25°C, $UD_3 + O_2$ react with the same kinetics as $U + O_2$. This assumption was made because no published reaction kinetics data could be found for oxidation of uranium hydride. If this assumption was true, then there should be minimal reaction when O_2 gas is injected into the bed (i.e., O_2 will flow through the bed without reacting because elevated temperatures are required for $U + O_2$ to quickly react).

Only 20% of the oxygen required to fully oxidize the bed to UO_2 was slowly injected over ~300 seconds. The initial bed temperature was between 30 and 35°C. The plumbing between the reactor exit and receiver was heated to 100°C to minimize condensation of water, facilitating its detection, should any be formed during the reaction. Finally, surface-mount thermocouples were attached to the reactor-tube as shown in Figure 26.

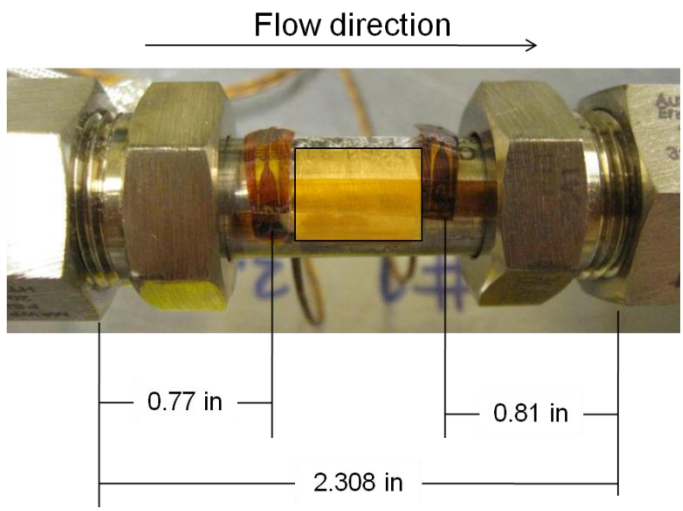

Figure 26: Surface-mount thermocouple locations for injection 1. The orange square indicates the position of the UD_3 bed inside the reactor tube. The tube OD and ID are 1.43 and 0.8 cm, respectively.

4.2.2.1 Experimental results

Figure 27 shows system pressures during injection. The bed contained an overpressure of 30 psia (0.21 MPa) D_2; which reduced to 22 psia (0.15 MPa) upon opening the reactor hand valves and expanding into the tubing volume between AO1 and AO2. This gas vented into the receiver tank when AO2 was opened. Upon pressure equilibration, AO1 was opened to admit oxygen at 19.5 psia (0.13 MPa) into the reactor. Oxygen flowed smoothly into the reactor until the system reached pressure equilibrium at 300 seconds whereupon AO1 was closed. At 480 seconds, AO2 was closed to seal the reactor.

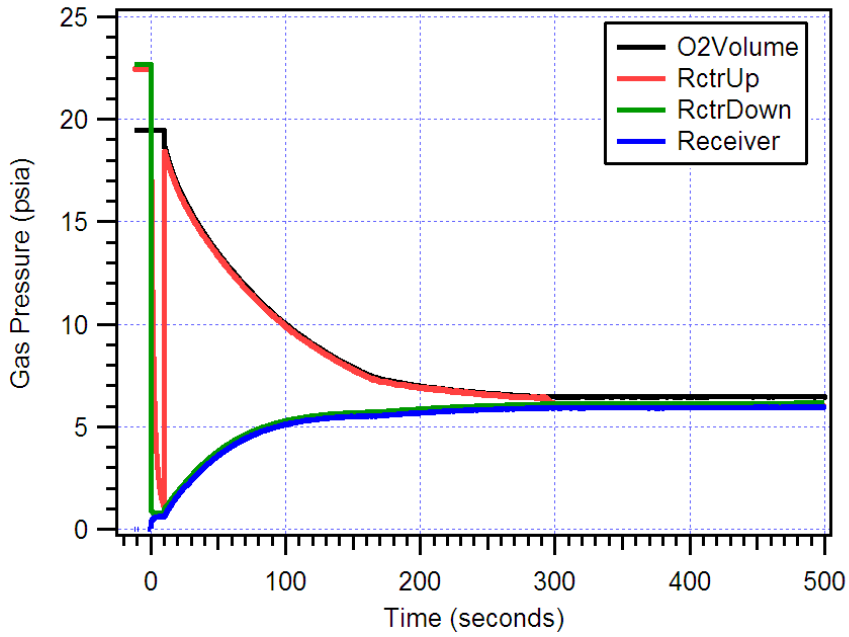

Figure 27: System pressures during injection 1.

The RGA monitored effluent gas composition during the test; it was configured to record data for the mass-to-charge ratios listed in Table 2.

Table 2: RGA channel configuration

Mass/charge ratio (amu/e_c)	Expected major species
3	HD
4	D_2/He
18	H_2O
19	HDO
20	D_2O
28	N_2/CO
32	O_2
44	CO_2

The bed was loaded with deuterium (99.7% D, 0.3 % H). The species in Table 2 were selected to cover deuterium, normal/deuterated water, CO formed if oxygen reacted with any carbon impurities in the UD_3, unreacted O_2, and CO_2 formed from carbon impurities. Figure 28 shows the RGA signals during injection 1.

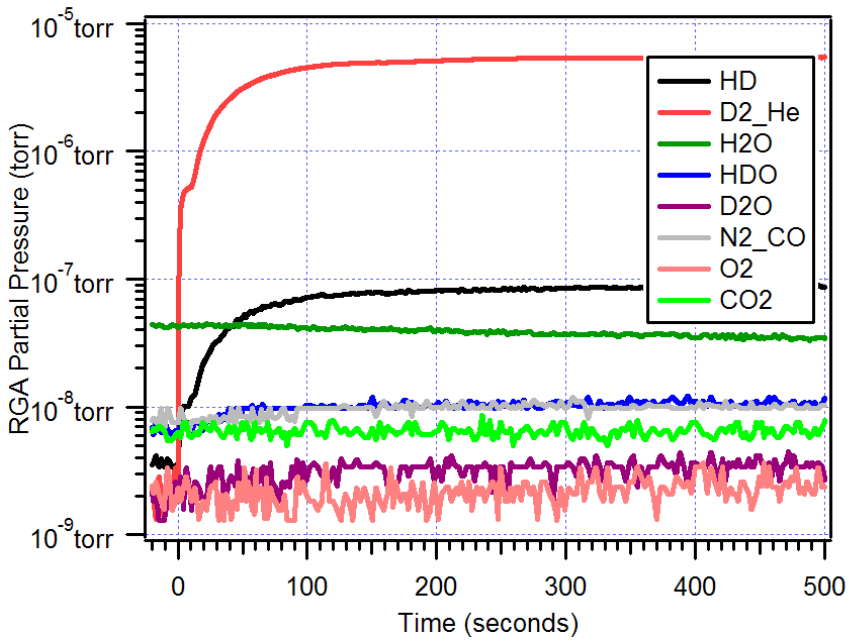

Figure 28: RGA partial pressure signals during injection 1.

All signals, with the exception of H_2O, start below 10^{-8} torr. The initial H_2O signal is residual water in the unbaked RGA vacuum system. When AO1 opens, D_2 and its mixed isotope impurity, HD, are observed. When O_2 injection begins, the D_2 and HD signals climb as the receiver pressure increases. Other than a factor-of-two increase in HDO and N_2/CO, no other signals vary significantly. It is hypothesized that the N_2/CO signal increase may be due to a small N_2 impurity in the injected oxygen (N_2 passes through the bed without reacting). Also, the HDO observed is likely formed in the RGA by the reaction of D_2 with residual H_2O producing HDO and HD.

The RGA record shows that neither O_2 nor D_2O exit the reactor during injection. This is in contrast to the model prediction (under the assumption that $UD_3 + O_2$ kinetics are the same as $U + O_2$ kinetics) and expressly implies that, under these conditions, the $UD_3 + O_2$ reaction is much faster than the $U + O_2$ reaction. The equivalent-kinetics assumption has therefore been disproved. The data also imply that if any water forms in the bed, it reacts further to form uranium oxide(s) and D_2 before it can exit the reactor; this was expected from thermodynamic considerations and practical experience [19].

The surface-mount thermocouple signals confirm that the $UD_3 + O_2$ reaction is rapid compared to the O_2 injection rate. That is, the data are consistent with a front-like reaction morphology within the bed; the upstream reactor surface temperature sharply increases before the downstream temperature (see Figure 29).

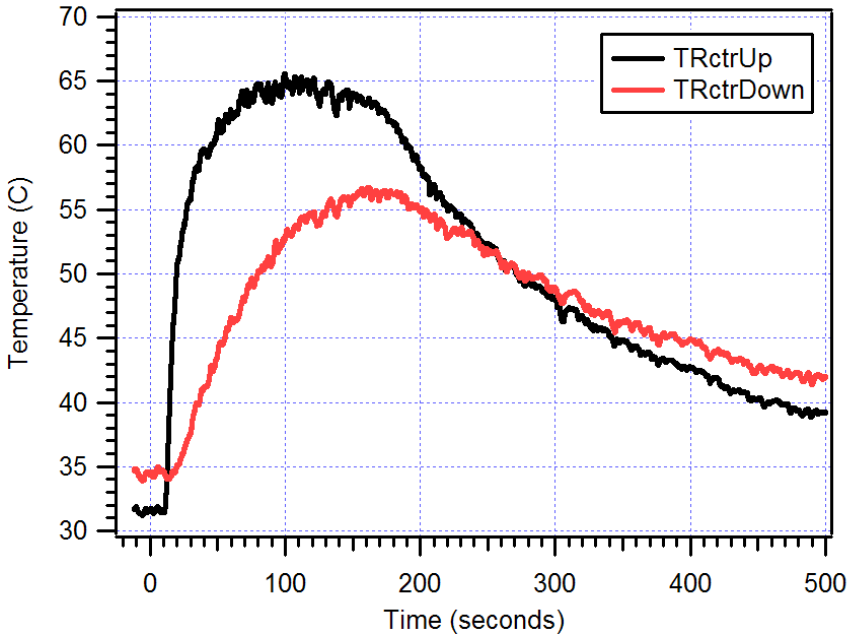

Figure 29: Surface-mount thermocouple signals during injection 1.

Additional information about the reaction can be inferred by combining the RGA and PVT data. Sufficient data exist to perform a mole-balance analysis on the reactor. Treating the reactor as a control volume, as shown in Figure 30, the inflow and outflow of gases are compared during the test.

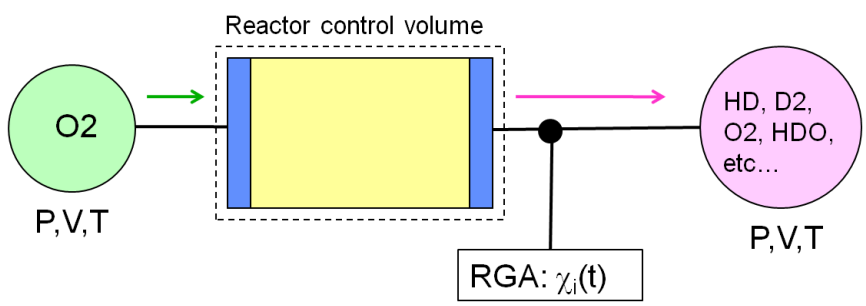

Figure 30: Reactor control volume schematic.

The rate of change of species *i* in the reactor is given by the net inflow and outflow rates,

$$\frac{\mathrm{d}n_i}{\mathrm{d}t} = \dot{n}_{in,i} - \dot{n}_{out,i}. \tag{31}$$

Pressure, volume, and temperature in the supply (green) and receiver (pink) are known or assumed[5]. Each vessel's instantaneous molar contents are derived from the PVT data. Molar flow rates are computed by numerically differentiating the curves using a second-order backward-differencing scheme. Figure 31 shows the receiver contents and fill rate.

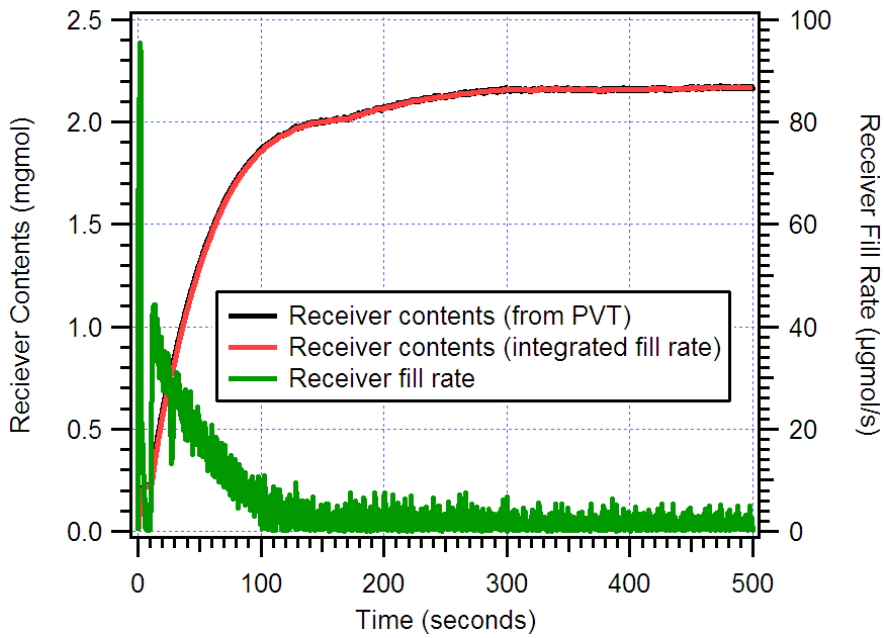

Figure 31: Receiver contents and fill rate for injection 1. The black curve is computed from PVT data; red curve is computed by numerically integrating the fill rate. Good agreement between these curves confirms that the numerical differencing scheme is appropriate.

Next, individual species molar flow rates were computed from the RGA partial pressures assuming that the RGA has identical responses for all species. Although, strictly speaking, this assumption is not true [23], it is immaterial when D_2 is the only gas present in significant quantity. Individual species flow rates are integrated to determine the receiver vessel contents.

[5] The O2Volume gas temperature is assumed to be constant and equal to the initial ambient temperature. This is a reasonable assumption because the gas transfer time is long compared with the gas-to-vessel-wall characteristic heat transfer time.

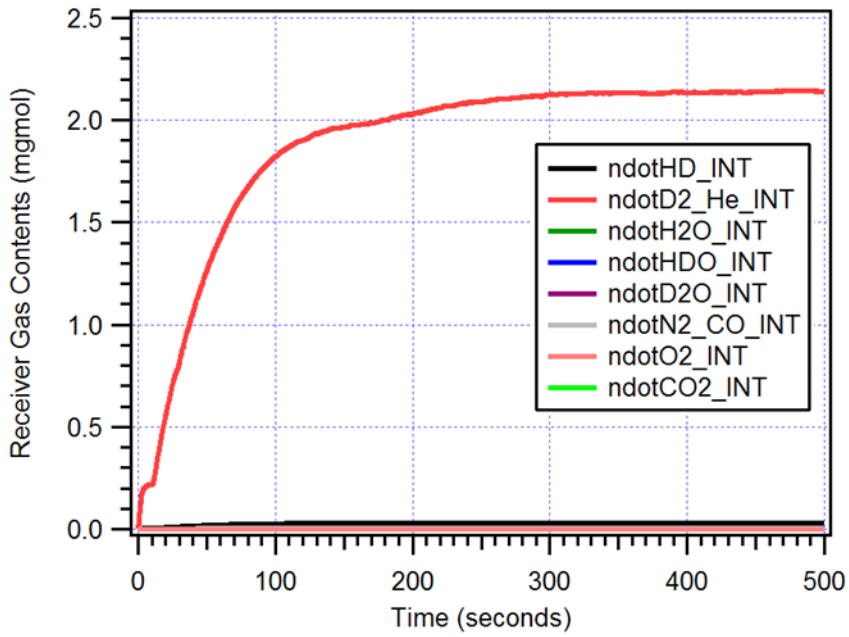

Figure 32: Receiver vessel contents; D_2 is the only significant gas present.

To determine reactor inflow, a system-wide gas-phase mole balance was performed on oxygen (see Figure 33). The moles of O_2 in the driver and in the receiver were compared to the initial amount of O_2 present in the system. All O_2 missing from the gas-phase was assumed to be occluded in the reactor bed (as uranium oxide). This neglects O_2-gas present in the reactor void space, but this volume is negligible.

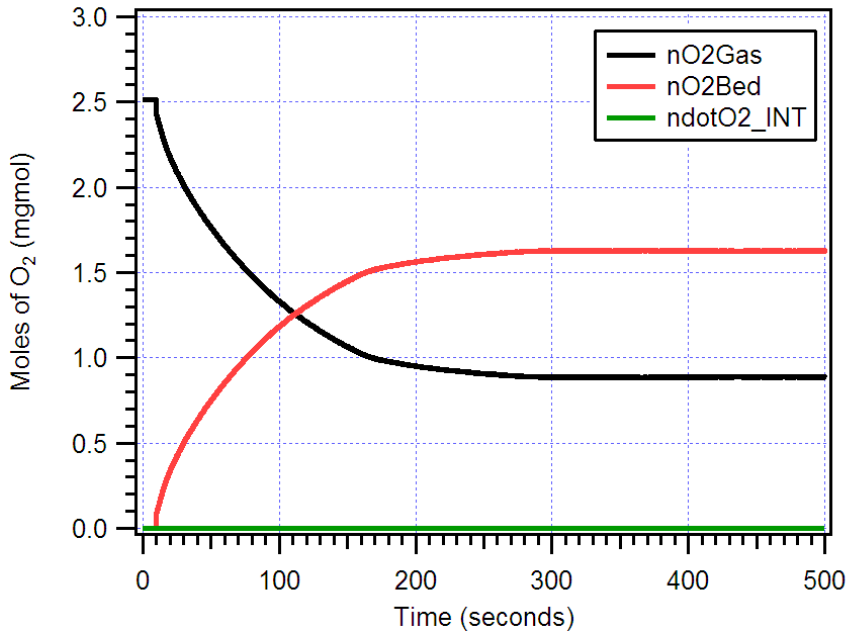

Figure 33: Oxygen mole balance.

Next, the reactor inflow and outflow are compared. Rather than comparing the total deuterium outflow, including the overpressure gas, only the amount of D_2 evolved from the bed is compared to the amount of O_2 occluded by the bed. The reactor overpressure quantity was estimated from the reactor's initial PVT conditions and subtracted from the receiver contents to estimate evolved D_2. Figure 32 illustrates how this correction is quite small (compare the initial hump in the D2 curve between 0 an 10 seconds with the final value at 500 s). Figure 34 shows the occluded oxygen and evolved deuterium. The initial jump in evolved D_2 between 0 and 10 seconds is due to imperfect overpressure-gas correction.

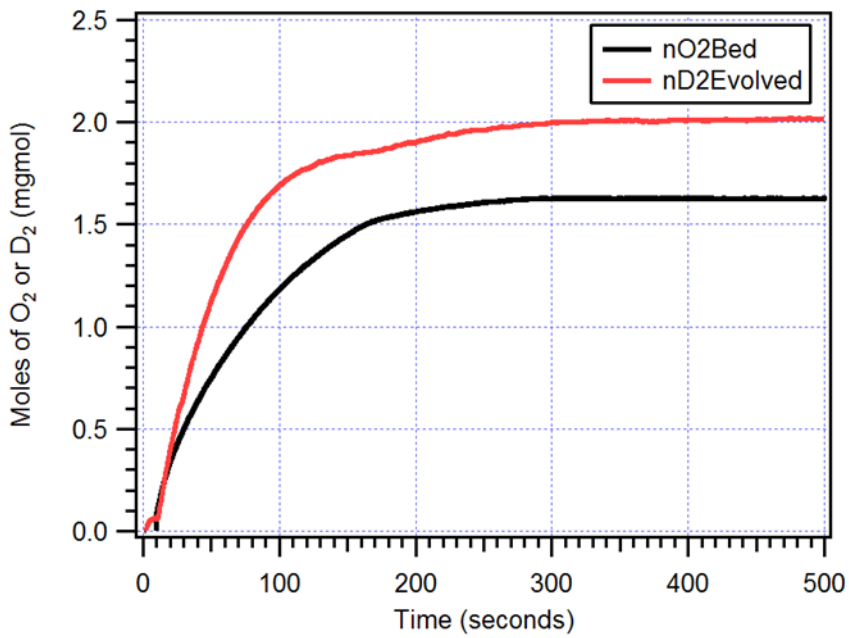

Figure 34: Total reactor oxygen inflow and deuterium outflow during injection 1.

The data in Figure 34 better illustrate the injection and evolution process if the ratio of D_2 evolved to O_2 consumed is plotted as shown in Figure 35.

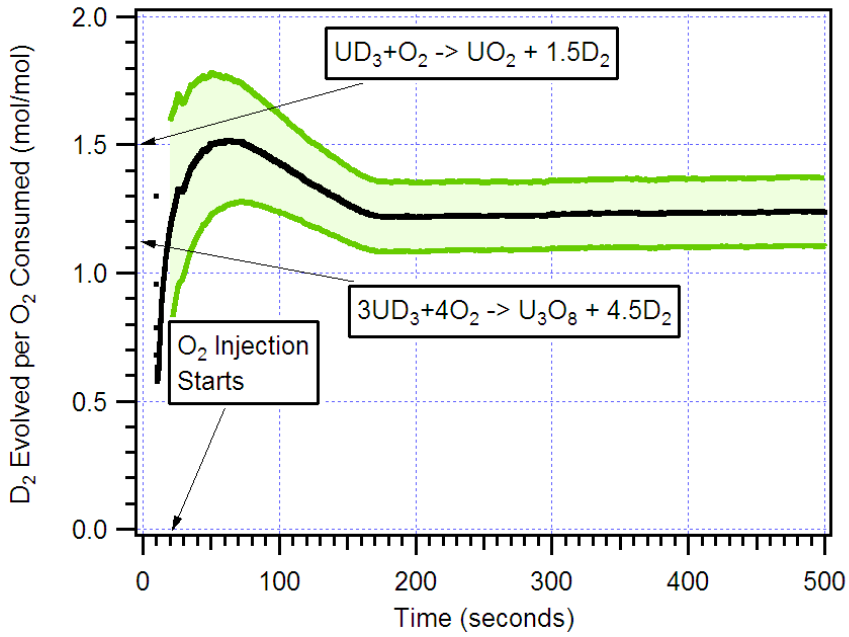

Figure 35: Reactor mole-balance derived D_2 evolution per O_2 consumption. The black curve is the computed data. The green band estimates error. Theoretical values for two possible oxidation reactions are indicated on the ordinate.

Several inferences about the global reaction can be gleaned from Figure 35. First, the ratio isn't constant, even when considering measurement accuracy. However, as the transfer approaches completion, the ratio approaches 1.2. The theoretical value for U_3O_8 formation is 1.125 and is within the experimental error band (green); as are theoretical values for U_3O_7, 1.29, and U_4O_9, 1.33, which are understood to form at temperatures below 250 °C [42]. While the data cannot distinguish between U_3O_7, U_3O_8, and U_4O_9, it is nevertheless believed that the results imply one of two things:

1. Oxygen injection produces U_3O_8 directly and the local temperatures are also high enough to decompose UD_3 near the reaction front (increasing D_2 evolved/O_2 consumed above the U_3O_8 value).
2. Oxygen injection initially produces UO_2, D_2 evolved/O_2 consumed = 1.5, most of which later oxidizes to U_3O_8.

For injection 1, the experimental uncertainty is large enough that it is impossible to distinguish between these two cases or between U_3O_8, U_3O_7, and U_4O_9. In the second injection, more oxygen was injected at a faster rate to better distinguish between case 1 and 2.

Finally, for injection 1 the O_2 mass balance indicated that either 13.7 mole-% or 10.3 mole-% of the UD_3 bed was oxidized, assuming the product was UO_2 or U_3O_8, respectively. The observed completeness of reaction and front-like temperature profile suggest that the bed might be layered, with fully oxidized material at the inlet and unreacted UD_3 at the outlet.

4.2.2.2 Post-test D_2 flow measurement

A flow test was performed after injection 1. The DGM flow parameter data are shown below; along with the data from the unoxidized (virgin) bed.

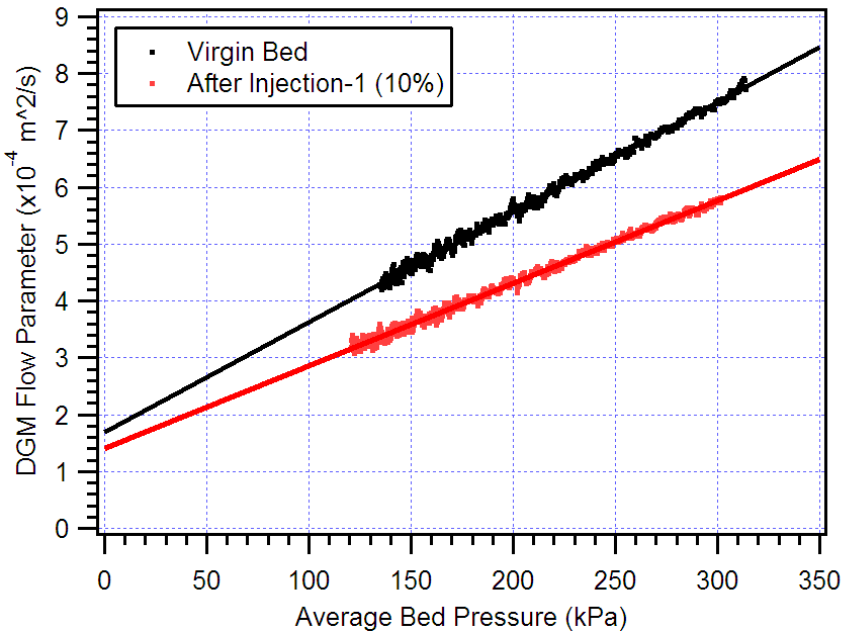

Figure 36: DGM flow parameters vs. average bed pressure before oxidation and after injection-1. Assuming the oxidation product is U_3O_8, injection 1 oxidized 10 mole-% of the bed. Measured data are dots. Least-squares regression lines are included for reference.

Both flow tests used D_2 gas, therefore the slopes and intercepts can be compared directly. Both effective DGM parameters[6] decreased when the bed was partially oxidized. This is not unexpected because, if a UD_3 particle oxidizes to U_3O_8 without decrepitating, its volume increases by a factor of 1.52. Therefore, when a section of bed transforms to U_3O_8, the local porosity is predicted to decrease from 0.60 to approximately 0.39. The decrease in porosity would cause corresponding decreases in the DGM parameters B and K_0. This is discussed in more detail in the following sections.

4.2.2.3 Model results

Injection-1 used an oxygen source vessel with a volume of 45 cm^3 and an initial pressure of 20 psia (0.14 MPa). Oxygen was allowed to flow into the reactor while the effluent gas was collected in the 150 cm^3 receiver vessel. The model was used to simulate that experiment. The detailed results from the model for the chemical reactions, thermal response, mass transfer and pressure decay in the source are presented in the next several figures. Figure 37 shows a close-up

[6] Here it is important to remember that the DGM parameters are effective values for the whole bed. It is almost certain that the bed composition, porosity, and pore-size are non-uniform and likely stratified after injection 1. After injection 1, the upstream ~10 % of the bed is nearly all U_3O_8 and the remaining ~90% is UD_3.

of the bed region of the model[7], where it can be seen that a reaction front is predicted to form at the leading edge of the hydride material. This front moves upward into the bed with time. The reaction rate is sufficiently large to consume all the oxygen, such that the overall reaction rate is determined by the flow rate of oxygen into the hydride material. As the oxygen flow rate decreases with time, the thickness of the reaction front, and its propagation speed into the hydride material, both decrease.

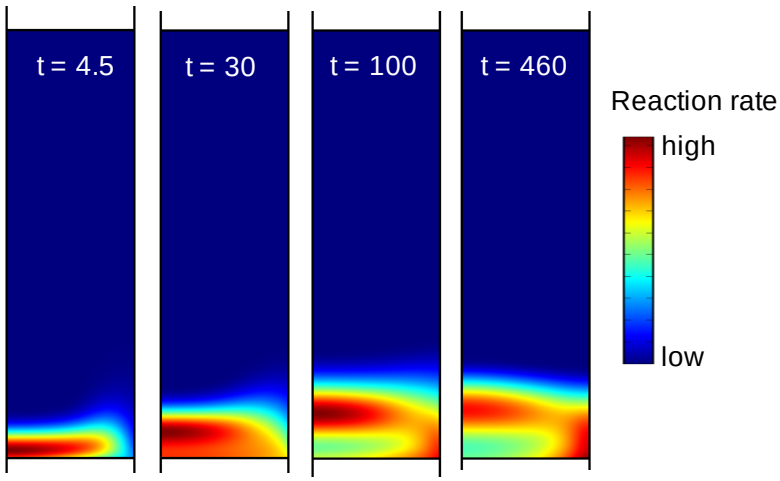

Figure 37: The UD_3 oxidation reaction front predicted by the model at various times for the first oxygen injection experiment. Color is used here only to distinguish between large and small reaction rates at each time state. The actual maximum reaction rate decreases with increasing time.

The temperature and deuterium distributions in the vicinity of the hydride bed early in the process are shown in Figure 38a and b. A region of high temperature is created at the location of the UD_3 reaction front. Due to the slow oxygen injection rate (resulting from the small permeability in the bed and due to the close proximity to the frit, which has a relatively large thermal conductivity), the temperatures that develop are not sufficiently high to decompose (dehydride) the hydride material. Consequently, the model predicts that only the UD_3 oxidation reaction occurs during injection-1. The deuterium concentration is largest at the interface between the leading frit and hydride material, which is where the reaction front was located at t = 4.5 s (see Figure 37). The D_2 concentration is also large downstream of that interface, as well as next to the reactor wall, but near the reactor axis it is smaller due to the high temperature present there. Farther downstream, the concentration decreases as the D_2 disperses by diffusion, and as it moves into regions of lower pressure (i.e., there is a pressure gradient in the bed, with high pressure at the bottom and low pressure at the top). The figure also shows that due to the small flow velocity (typically 3 cm/s near the leading edge of the bed) D_2 is able to diffuse upstream into the inlet frit and even toward the oxygen inlet channel leading to the bed. Figure 38c shows the final UD_3 distribution predicted at the end of the first oxygen injection experiment. The hydride material at the leading edge of the bed has been nearly completely consumed and converted to U_3O_8, while downstream of that region the UD_3 is still at its initial concentration.

[7] In this figure and all similar illustrations, flow enters the bed at the bottom and exits at the top. The left side is the center-axis of the bed and the right side is the outer wall.

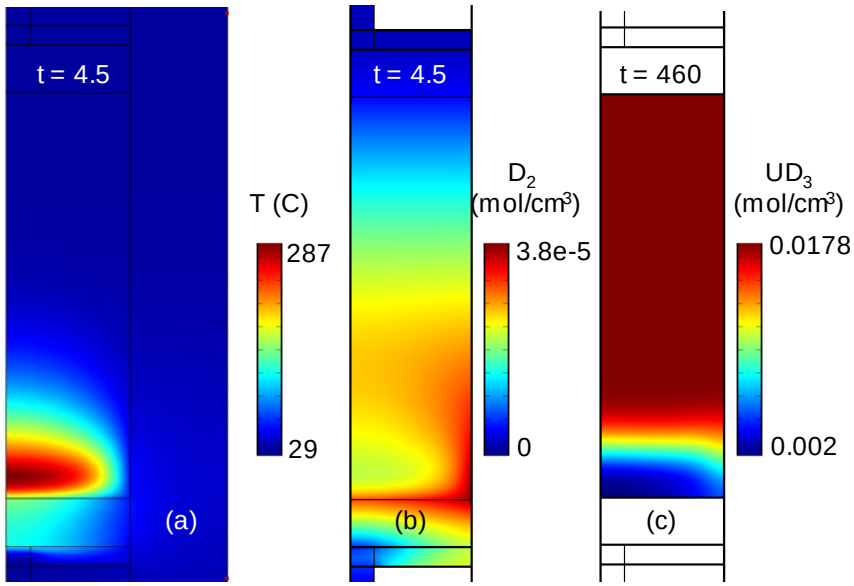

Figure 38: Predictions for the (a) temperature and (b) deuterium distributions in the vicinity of the bed, early in the first oxygen injection experiment, and the (c) final UD_3 distribution at the end of the experiment.

The calculated pressure decay in the oxygen source vessel is shown in Figure 39a, along with the measured result, for injection-1. At early times, the model appears to accurately predict the rate of pressure decay, but later the predicted decay rate is smaller than measured. Figure 39b shows the results for the flow-through experiment that followed injection-1. Here, the model clearly under-predicts the pressure decay rate, indicating it under predicts the permeability of the bed, consistent with the results shown in Figure 39a at later times in the simulation. These results indicate that the bed evolution model described in Section 3.2.4 is not wholly correct; this isn't surprising.

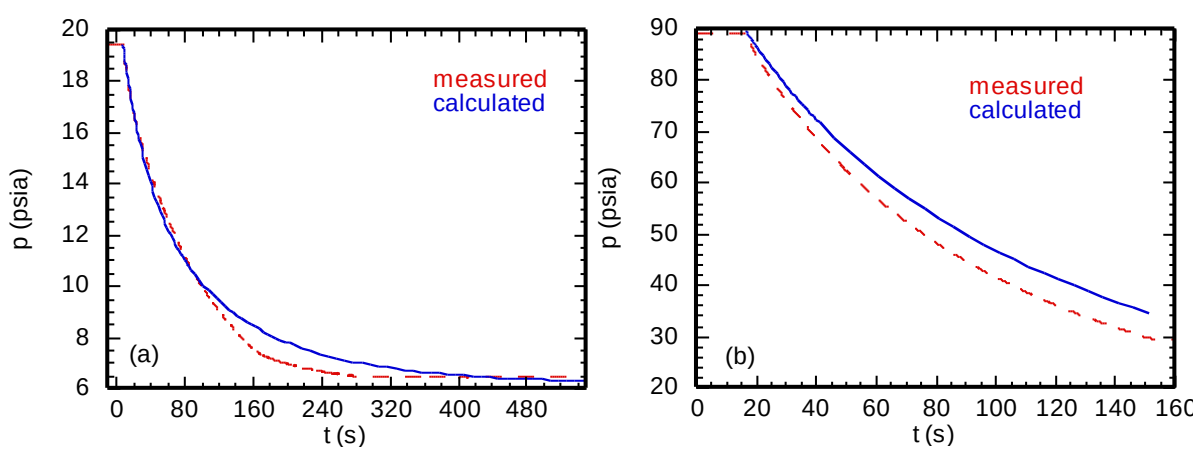

Figure 39: The pressure decay in the gas source vessel (a) during the first oxygen injection experiment, and (b) during the subsequent flow-through test.

The temperature distribution in the hydride material on axis at various times is shown in Figure 40a. The reaction creates a region of high temperature. The frit provides enhanced conduction due to its relatively large conductivity compared to the hydride, such that the maximum temperature is located ~0.07 cm from the leading frit (located at z = 0). There is some heat transfer, primarily by conduction, to other portions of the bed downstream resulting in elevated temperatures there. Figure 40b shows the temperature as a function of time at the thermocouple locations. Although there are some differences between the calculated and measured results, they have an important similarity, they both show that at the upstream location (TC#1) the maximum temperature is higher than that at the downstream location (TC#2). Based on the model, this is due to the confinement of the exothermic reaction and associated heat generation to the leading edge of the bed (i.e., the reaction forms a front as opposed to being distributed throughout the bed). The measured results appear to corroborate this behavior.

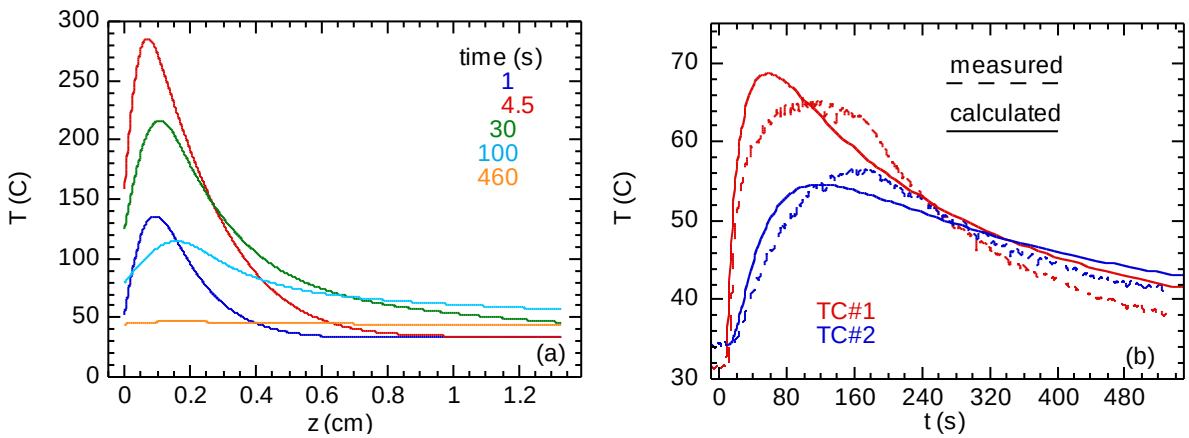

Figure 40: (a) The calculated temperature profiles in the bed on axis at various times, and (b) a comparison of calculated and measured temperatures at the locations of the thermocouples.

Figure 41 shows the UD_3 and oxygen mole fraction profiles on axis in the vicinity of the leading edge of the bed. The UD_3 profile at t = 1 is still near the initial condition (0.0178 mol/cm^3), and the profiles at later times show that the UD_3 concentration tends towards zero near the leading edge of the bed, but at positions downstream it is still at its initial value. The oxygen mole fraction profiles show that at the leading edge of the bed the gas is not pure oxygen due to the presence of deuterium, and that no oxygen exists downstream of $z \approx 0.35$ cm (i.e., all of the oxygen is consumed by the reaction front).

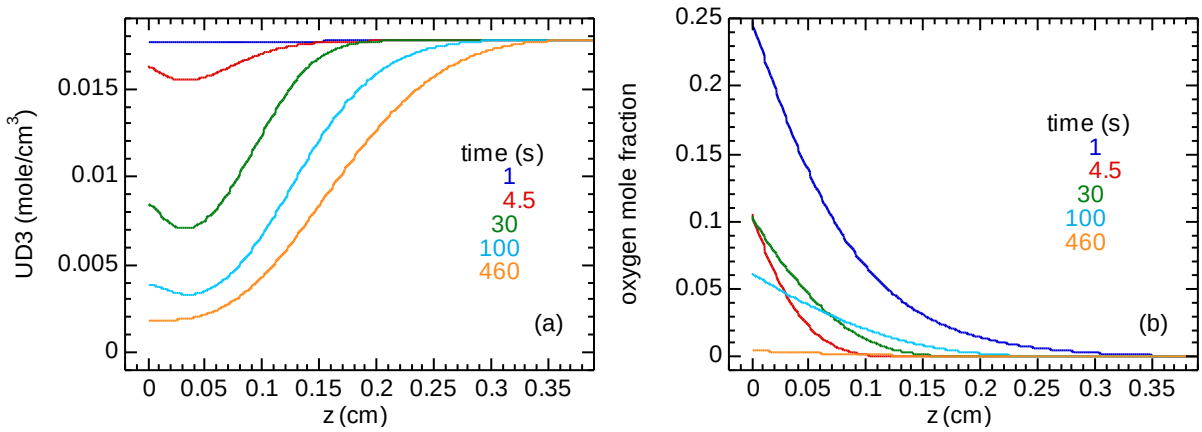

Figure 41: The calculated (a) *UD*$_3$ and (b) oxygen mole fraction profiles on axis near the leading edge of the bed at various times.

4.2.3 O_2 injection-2

The goal for the second O_2 injection test was to take the bed up to approximately 36 mole-% oxidized (assuming a UO_2 oxide product) to see how the reactor effluent behaved.

For this experiment, only 26% of the oxygen required to fully oxidize the bed to UO_2 was injected over ~500 seconds. The initial bed temperature was between 30 and 40°C. The plumbing between the reactor exit and receiver was heated to 100°C to facilitate water detection should any be formed during the reaction. Finally, the surface-mount thermocouples shown in Figure 26 were monitored during the test.

4.2.3.1 Experimental results

The pressure data of Figure 42 show smooth gas input and output. The AO1 valve was closed near 480 seconds, terminating oxygen injection. The downstream valve, AO2 was closed at 550 seconds, sealing the reactor.

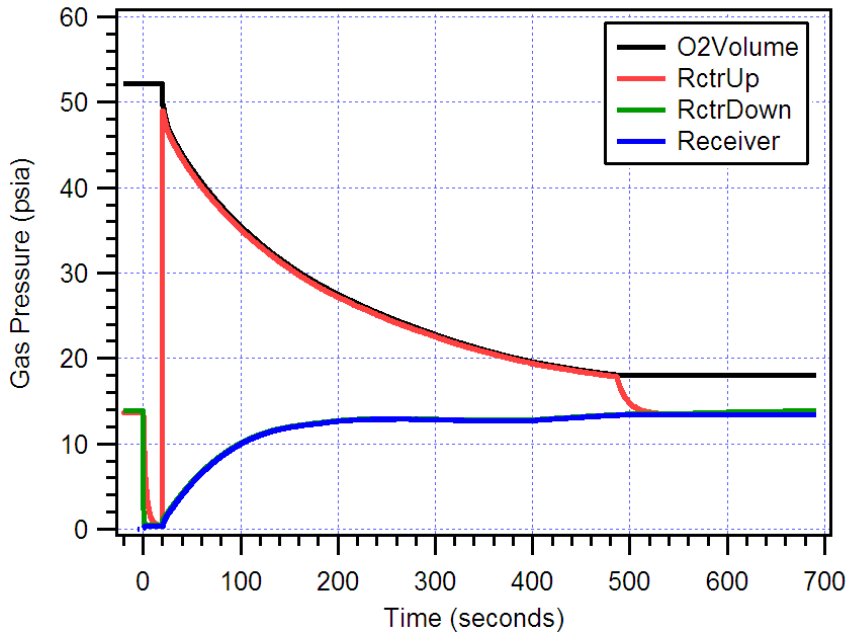

Figure 42: Pressure data from injection-2.

RGA signals are shown in Figure 43. Channel configuration was identical to injection-1 with the exception that H2 (m/e=2) was added to the list.

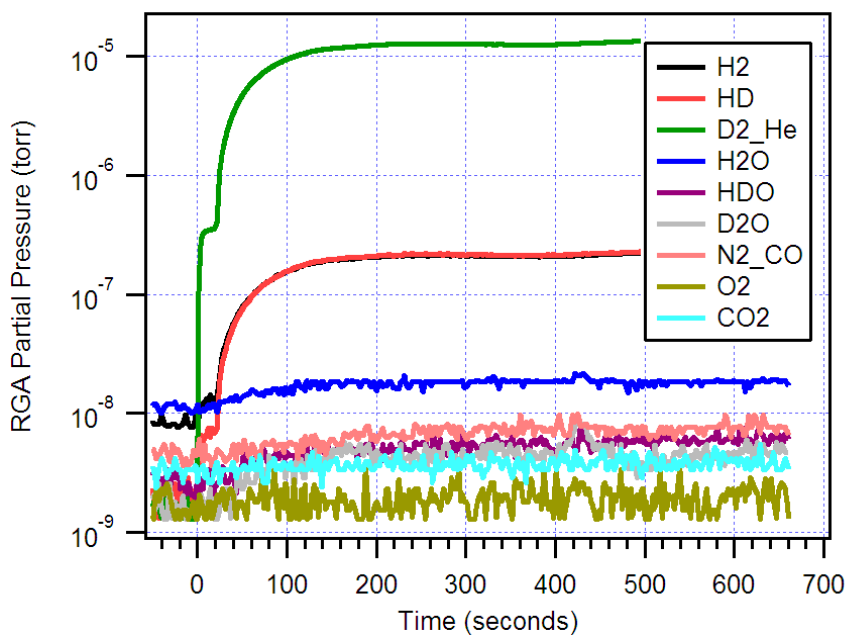

Figure 43: RGA data from injection-2.

All signals, with the exception of H_2O, start below 10^{-8} torr. The initial H_2O signal is residual water in the unbaked RGA vacuum system. When AO1 opens, D_2, its mixed isotope impurity,

HD, and H_2 are observed[8]. When O_2 injection begins, the hydrogen isotope signals climb as the receiver pressure increases. During injection, there is an approximately factor-of-two increase in H_2O, HDO, D_2O, and N_2/CO; no other signals vary significantly.

Similar to injection-1, it is hypothesized that the N_2/CO signal increase may be due to an N_2 impurity in the injected oxygen (N_2 passes through the bed without reacting). Also, HDO is likely formed in the RGA by the reaction of D_2 with residual H_2O producing HDO and HD. However, the small increase in H_2O and D_2O is not readily explainable. It is possible that a very small amount of D_2O formed in the bed and exited without reacting. This will be discussed in detail when injection-3 is analyzed. The increase in H_2O remains a mystery.

The RGA record shows that no O_2 and very little D_2O exited the reactor during injection. As with injection 1, the data imply that if any water forms in the bed, it reacts further to form uranium oxide(s) and D_2 before it can exit the reactor.

Reactor mole-balance analysis was performed as described for injection-1. The ratio of D_2 evolved to O_2 consumed during injection-2 is shown in Figure 44.

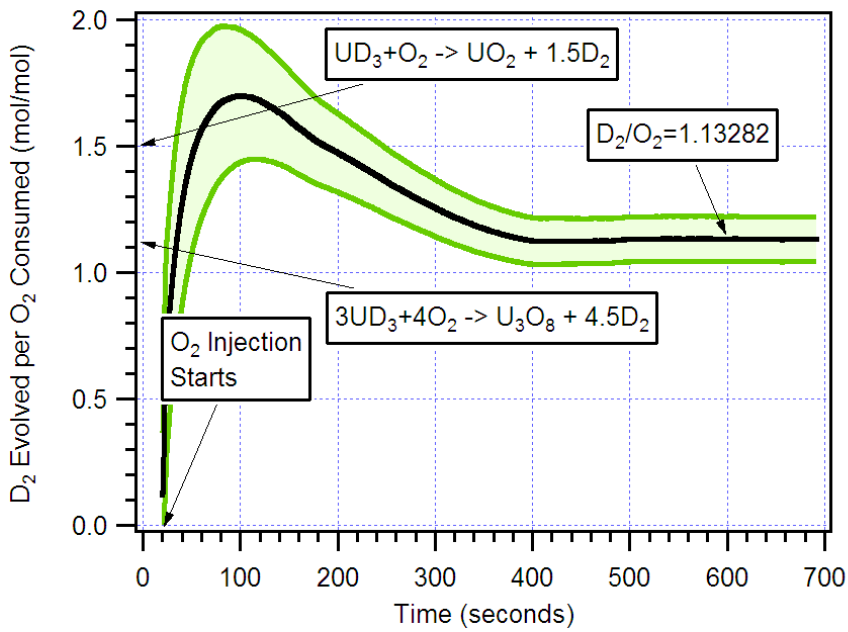

Figure 44: Reactor mole-balance derived D_2 evolution per O_2 consumption. The black curve is the computed data. The green band estimates error. Theoretical values for two possible oxidation reactions are indicated on the ordinate.

It is found that, similar to injection-1, the D_2/O_2 ratio is not constant. Also, as before, as the transfer approaches completion, the ratio approaches 1.13. The theoretical value for U_3O_8 formation, 1.125, is within experimental error. The values for U_3O_7, 1.29, and U_4O_9, 1.33, are outside the error band; this is expected because the predicted bed temperatures are high enough

[8] The relative magnitude of the H_2 and D_2 signals indicate that the m/e=2 signal is a cracking product of D_2; either D^+ or D_2^{2+}. For D_2 cracking, typically the m/e=2 signal is about 1.6% of the m/e=4 signal.

to convert either U_3O_7 or U_4O_9 to U_3O_8 [42]. Finally, at approximately 100 seconds the ratio exceeds the theoretical value for UO_2 formation. It is therefore reasonable to conclude that, in this case (where more oxygen was injected at a faster rate and where the reaction front is closer to the center of the bed), there was some direct thermal decomposition of UD_3 to U and D_2. This is consistent with internal bed temperatures predicted by the numerical model. The post-decomposition uranium powder later oxidized, eventually forming U_3O_8.

Finally, for injection 2 the O_2 mass balance indicated that 26.9 mole-% of the UD_3 bed has been oxidized (assuming the product is U_3O_8). It is believed that the bed is layered, with fully oxidized material at the inlet and unreacted UD_3 at the outlet.

4.2.3.2 Model results

The second oxygen injection experiment used a larger pressure (52 psia/0.36 MPa) in the oxygen source vessel. The initial state of the reactor for the second injection was the final state following the first injection, i.e. the leading ~10% of the bed was oxide. The larger source pressure creates a larger flow rate of oxygen into the reactor, and consequently a larger reaction rate of UD_3 oxidation (reaction 7) and larger temperatures. This leads to UD_3 decomposition (reaction 5) and the formation of the uranium phase, which then leads to uranium oxidation (reaction 6). This can be seen Figure 45 where the reaction fronts associated with reactions 5-7 are shown ~10 s after the beginning of the oxygen injection (the injection began at t = 19.3 s in this experiment). The UD_3 oxidation front started out looking (not shown here) like that shown in Figure 37 for injection-1, where it spanned across the bed from the axis to the reactor wall, but that reaction created large temperatures and the decomposition of UD_3 to form U near the axis such that UD_3 oxidation is then confined to the near wall region and a U oxidation front exists near the axis. A UD_3 decomposition reaction front can be seen leading the U oxidation front (Figure 45b).

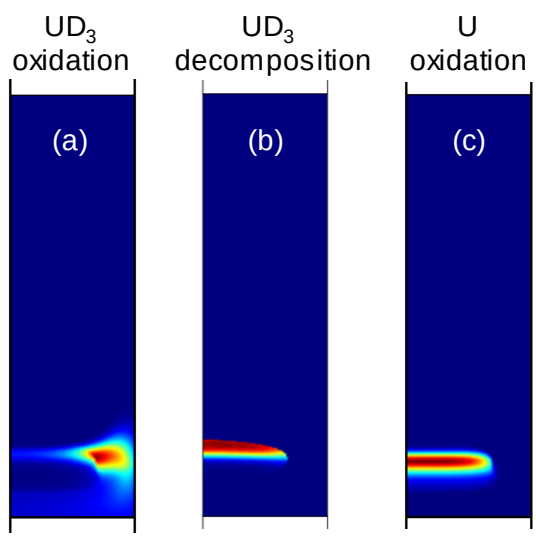

Figure 45: The UD_3 (a) oxidation and (b) decomposition fronts, and the (c) U oxidation front, early (t = 30s) in the simulation of the second oxygen injection experiment.

Figure 46 shows the temperature, U and UD_3 distributions early in the second oxygen injection. Gas flow streamlines are also shown along with the temperature result (Figure 46a). A perturbation to the streamlines can be seen in the region of high temperature created by the reaction because the gas expands as it flows through this region. A small region of uranium has been created by UD_3 decomposition (Figure 46b). The uranium is formed by a decomposition front at the leading edge of this region (upper side) and it is consumed by oxidation at its trailing edge (lower side). The UD_3 distribution at t = 30 s shows the region where the concentration has gone to zero by decomposition and has been replaced by U (Figure 46c). Later in the process after the oxygen flow rate has decreased, the reaction rate and temperature in the bed decrease as well. At this point, there is no decomposition, leaving UD_3 oxidation as the only reaction. The transition from pure U_3O_8 to pure UD_3 then resembles that shown in Figure 37 for injection-1, where it is approximately flat spanning from the reactor axis to the reactor wall. This leads to the final UD_3 distribution for injection-2 shown in Figure 46d at t = 510 s.

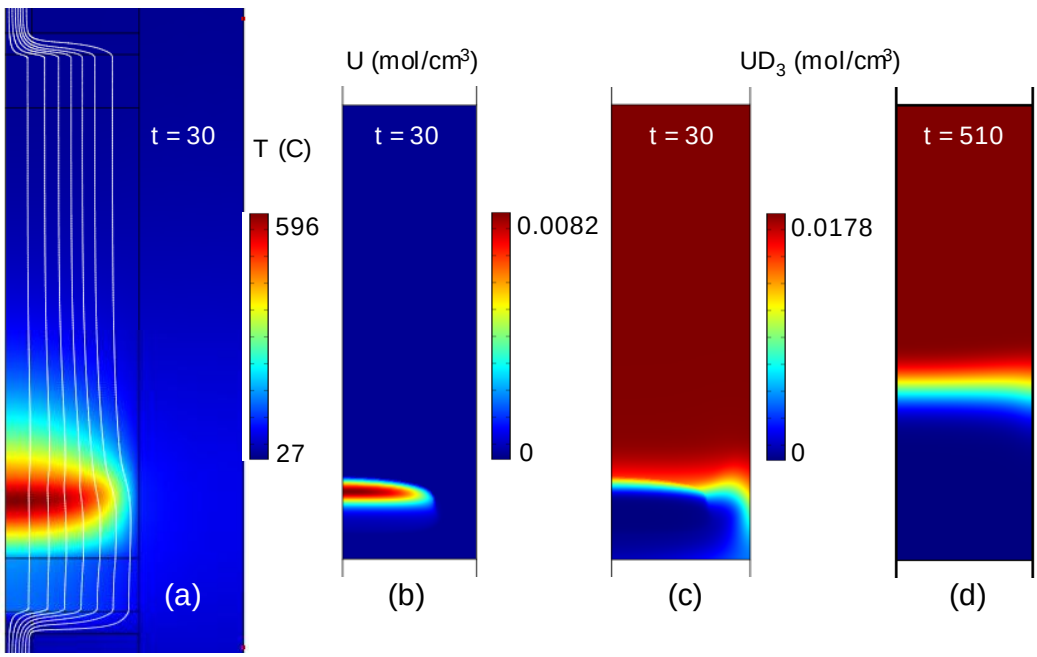

Figure 46: Predictions for the (a) temperature (with flow streamlines), (b) U and (c) UD_3 distributions in the vicinity of the bed, early in the second oxygen injection experiment, and (d) the final UD_3 distribution at the end of the experiment.

The calculated pressure decay in the oxygen source vessel is shown in Figure 47a, along with the measured result, for injection-2. The model over predicts the rate of pressure decay, indicating the calculated permeability is larger than the actual value. Figure 47b shows the results for the flow-through experiment that followed injection-2. Here again, the model over-predicts the pressure decay rate, consistent with the results in Figure 47a.

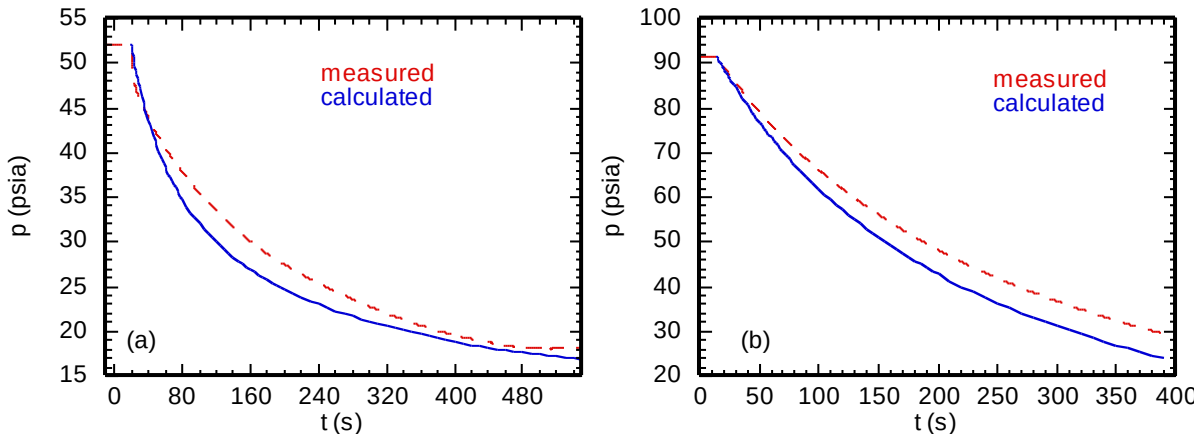

Figure 47: The pressure decay in the gas source vessel (a) during the second oxygen injection experiment, and (b) during the flow-through test that followed it.

The temperature distribution in the hydride material on axis at various times is shown in Figure 48a. The results are similar to those shown in Figure 38a for injection-1, except that the temperatures are much higher here due to the faster oxygen flow rate. Figure 48b shows the temperature as a function of time at the thermocouple locations. As was seen in injection-1, the maximum temperature at the upstream location (TC#1) occurs before the maximum temperature at the downstream location (TC#2), for both the measured and calculated results. However, here the measured result shows the maximums at the two locations are nearly equal, while the model continues to show the maximum for TC#1 is much larger than that for TC#2, as it did for injection-1. The reasons for this discrepancy are not known.

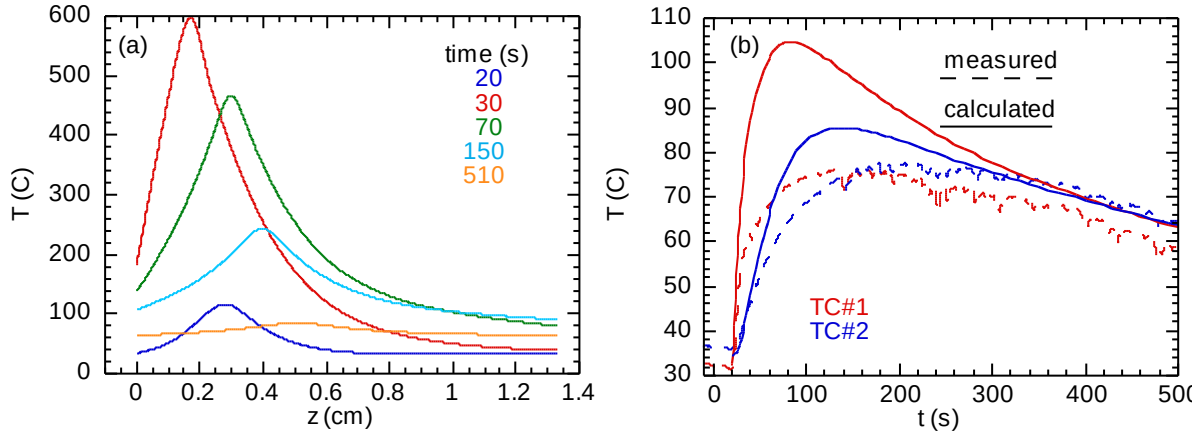

Figure 48: (a) The calculated temperature profiles in the bed on axis at various times, and (b) a comparison of calculated and measured temperatures at the locations of the thermocouples.

Axial profiles of the reaction rates, on axis in the bed, are shown in Figure 49a at various times. UD_3 oxidation is the only reaction early on (t = 20), and it is fairly broad in its extent over the bed. The heat produced by this reaction decomposes the hydride near the axis such that UD_3 oxidation is largely replaced by a UD_3 decomposition front followed by a U oxidation front later on (t = 30). At still later times, after the oxygen flow rate has decreased, and the slower reaction

rates allow temperatures to fall below the decomposition temperature, the UD_3 oxidation reaction becomes the only reaction on axis ($t \geq 150$). The integral of the reaction rates over the bed are shown in Figure 49b as functions of time, along with the oxygen flow rate (multiplied by ¾ to allow for a more direct comparison between it and the reaction rates, i.e. one mole of UD_3 or U is consumed for every 4/3 mole of O_2 consumed). All rates are largest at the beginning when the O_2 source pressure is large. At early times, the oxygen is consumed by a combination of UD_3 and U oxidation, where there is also UD_3 decomposition to produce the U. Later, only UD_3 oxidation remains and then it is equal to the ¾ O_2 injection rate.

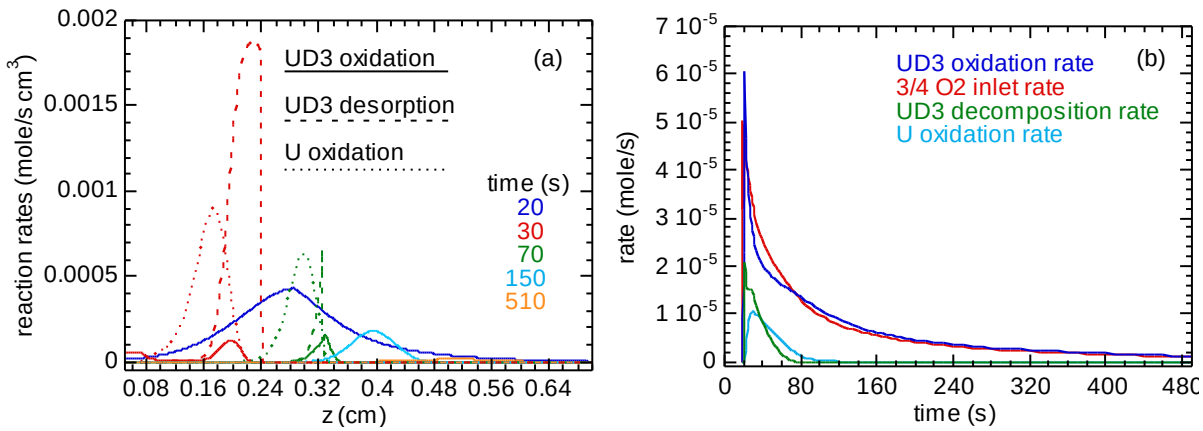

Figure 49: The calculated results for (a) the reaction rates on axis in the bed, and (b) the integral of the reaction rates over the entire bed as functions of time.

Figure 50 shows the UD_3 and U profiles on axis in the vicinity of the leading edge of the bed. The UD_3 profiles show the front that divides the portion of the bed that has been fully depleted of UD_3 from the region where it is still at its initial value (0.0178 mol/cm^3). This front propagates from left to right. Figure 50b shows that U is present only for t = 30 and 70 s.

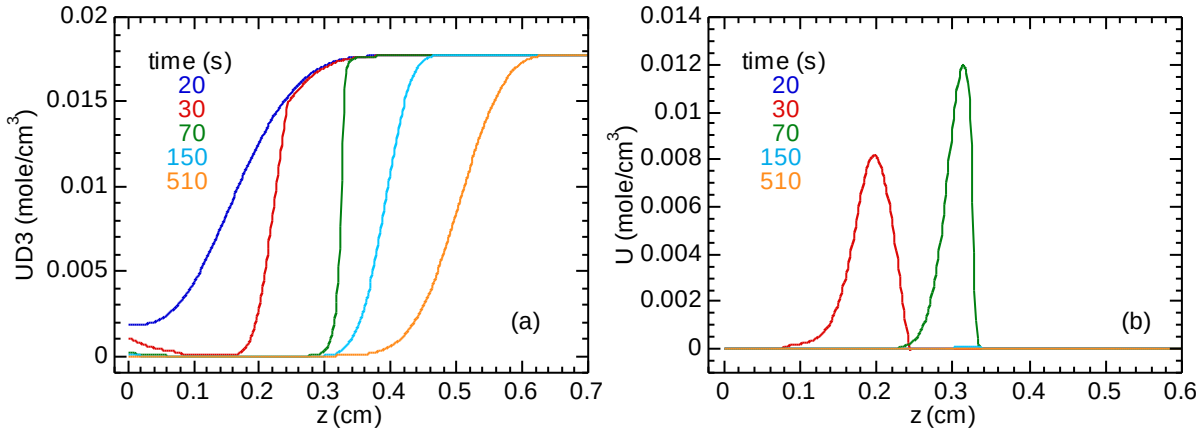

Figure 50: The calculated (a) UD_3 and (b) U profiles on axis near the leading edge of the bed at various times.

4.2.4 O_2 injection-3

The goal for the third O_2 injection test was to fully oxidize the bed and observe oxygen/water breakthrough.

For this experiment, 150% of the oxygen required to fully oxidize the bed to U_3O_8 was piston-driver injected over ~500 seconds. The initial bed temperature was between 30 and 40°C. The plumbing between the reactor exit and receiver was heated to 100°C to facilitate water detection should any be formed during the reaction. Finally, the surface-mount thermocouples shown in Figure 26 were monitored during the test.

4.2.4.1 Experimental results

Pressure data are shown in Figure 51. Oxygen injection started at 40 seconds. The helium-driven piston maintained an approximately constant upstream pressure until 95% of the oxygen had been injected. The remaining 5% depleted from the ~3.4 cm^3 upstream dead-volume between 250 and 500 seconds. Oscillations in the O2Volume and RctrUp pressures between 40 and 150 seconds are caused by piston friction (stick-slip behavior). The receiver pressure increases steadily during O_2 injection. The slope changes are believed to be caused by a changing bed temperature and bed-gas composition. Oxygen breakthrough is observed at 155 seconds.

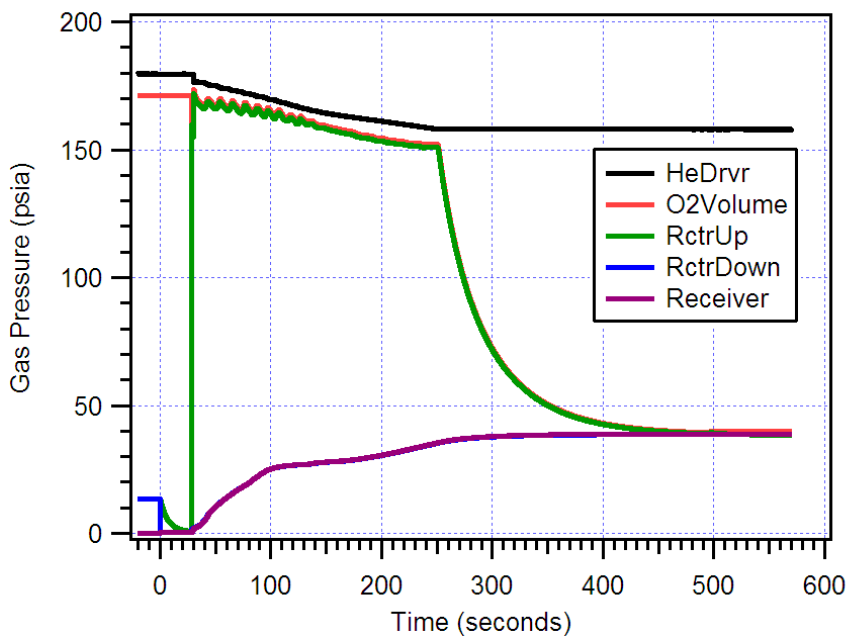

Figure 51: Pressures during injection-3.

RGA signals are shown in Figure 52.

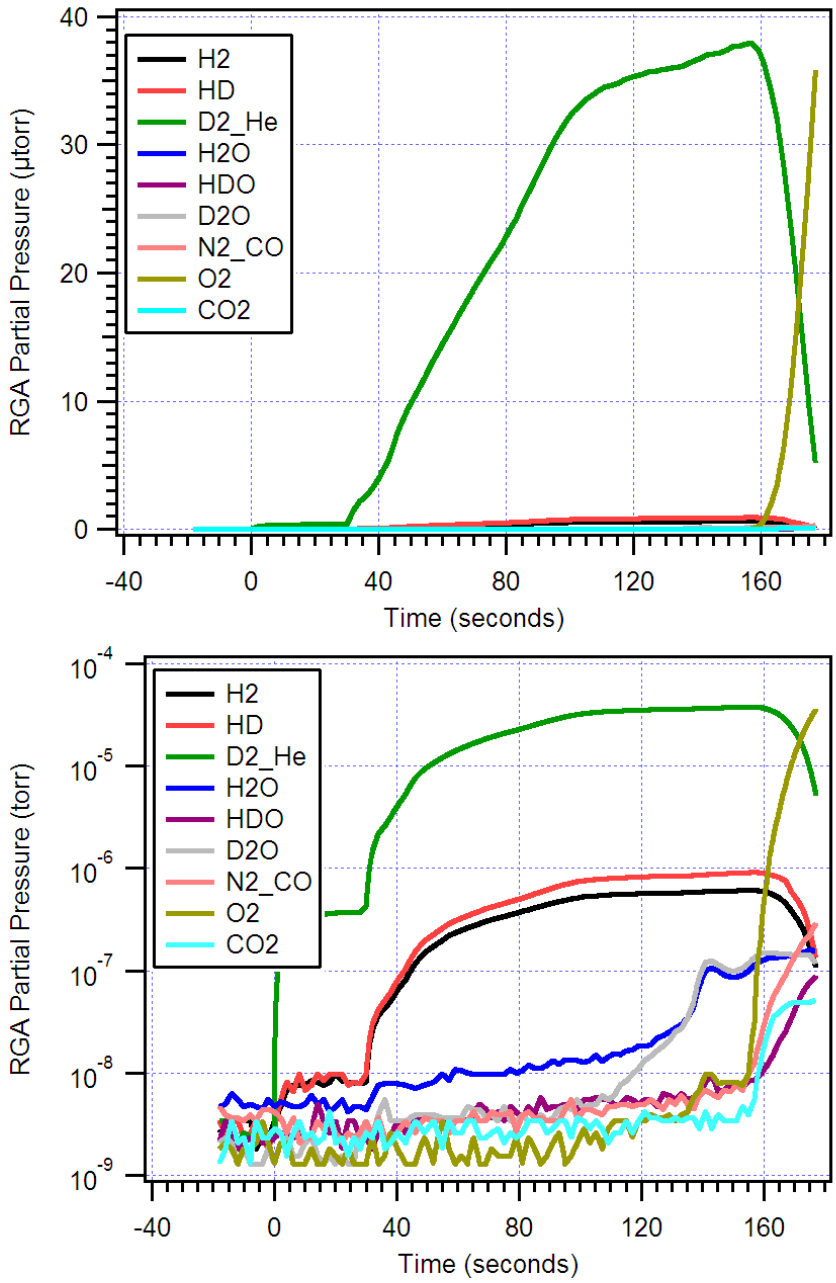

Figure 52: RGA signals during injection-3. The data are shown on linear (top) and log (bottom) scales.

Unfortunately, the entire breakthrough was not captured. At 177 seconds, the RGA-system pressure reached a high-limit and the RGA filament turned off. Nevertheless, enough of the breakthrough was captured to facilitate some analysis.

All signals start below 10^{-8} torr. When AO1 opens, only D_2, its mixed isotope impurity, HD, and H_2 are observed. When O_2 injection begins, the hydrogen isotope signals climb as the receiver pressure increases. The hydrogen isotope signals reach a peak at 157 seconds, and then decrease

as O_2 begins to emerge from the reactor. At this time, the effluent flow rate is 5×10^{-4} gmol/s; high enough that back-mixing at the RGA capillary has an insignificant effect on the measured RGA signals. There are about 15 seconds between the hydrogen isotope peak (157 s) and D_2/O_2 signal crossover (172 s); this is long enough that RGA response-time effects are not significant (the 50% response time for O_2 is about 2.5 seconds). As O_2 begins to emerge from the reactor at 157 s, known impurities in the oxygen gas, N_2 and CO_2, are also observed.

The water signals are more complicated. As in injection-2, there is an unexplained, approximately factor-of-two, increase in H_2O when injection begins. At 100 seconds, the D_2O signal begins to increase. At this point, the D_2 mass balance indicates that 90% of the bed has been consumed. The D_2O signal increases steadily until 140 seconds; then remains approximately constant until RGA data collection stops.

The H_2O and D_2O signals show some correlation; it is not exactly clear why. The H_2O signal, m/e = 18, likely contains contributions from H_2O^+ and DO^+; however the DO^+ contribution should be reasonably small, about 25% of the D_2O signal. Therefore it appears that we have both H_2O and D_2O in the reactor effluent and that their relative amounts are inconsistent with proportions in the H/D bed-composition; which is unexpected. Also, surprisingly, there is very little HDO until breakthrough (157 s). This is surprising because, if H_2O and D_2O were formed by oxygen-hydrogen reactions in the bed, one would expect to see H_2O, HDO, and D_2O relative abundances that are similar to the H/D bed composition (i.e. nearly all D_2O and HDO, with very little H_2O). Instead, the relative abundance of H_2O is much higher; something that cannot be explained at present. A series of control experiments involving known water vapor pressures and an inert bed would facilitate understanding of these signals

Perhaps the most that can be said from this data is that, water isotopologues appear when the bed has been 90% oxidized. However, the water concentration is quite low, ~0.05% of the effluent gas. It also appears that the abundance of waters is almost independent of oxygen breakthrough (i.e. the water signals do not change significantly between 157 and 177 seconds). It is therefore reasonable to conclude that, if the $UD_3 + (4/3)O_2 \rightarrow (1/3)U_3O_8 + (3/2)D_2$ reaction produces waters as an intermediate species, they are short-lived and therefore relatively unimportant.

Initial oxygen breakthrough at 155 s, occurs when the D_2 mass balance indicates that 95% of the bed has been oxidized. Oxygen concentrations increased monotonically until the RGA shut off at 177 s (at this time, the D_2 balance indicates 96% of the bed has been consumed). Figure 53 shows the D_2 evolved from the bed and the O_2 consumed by the bed during injection-3.

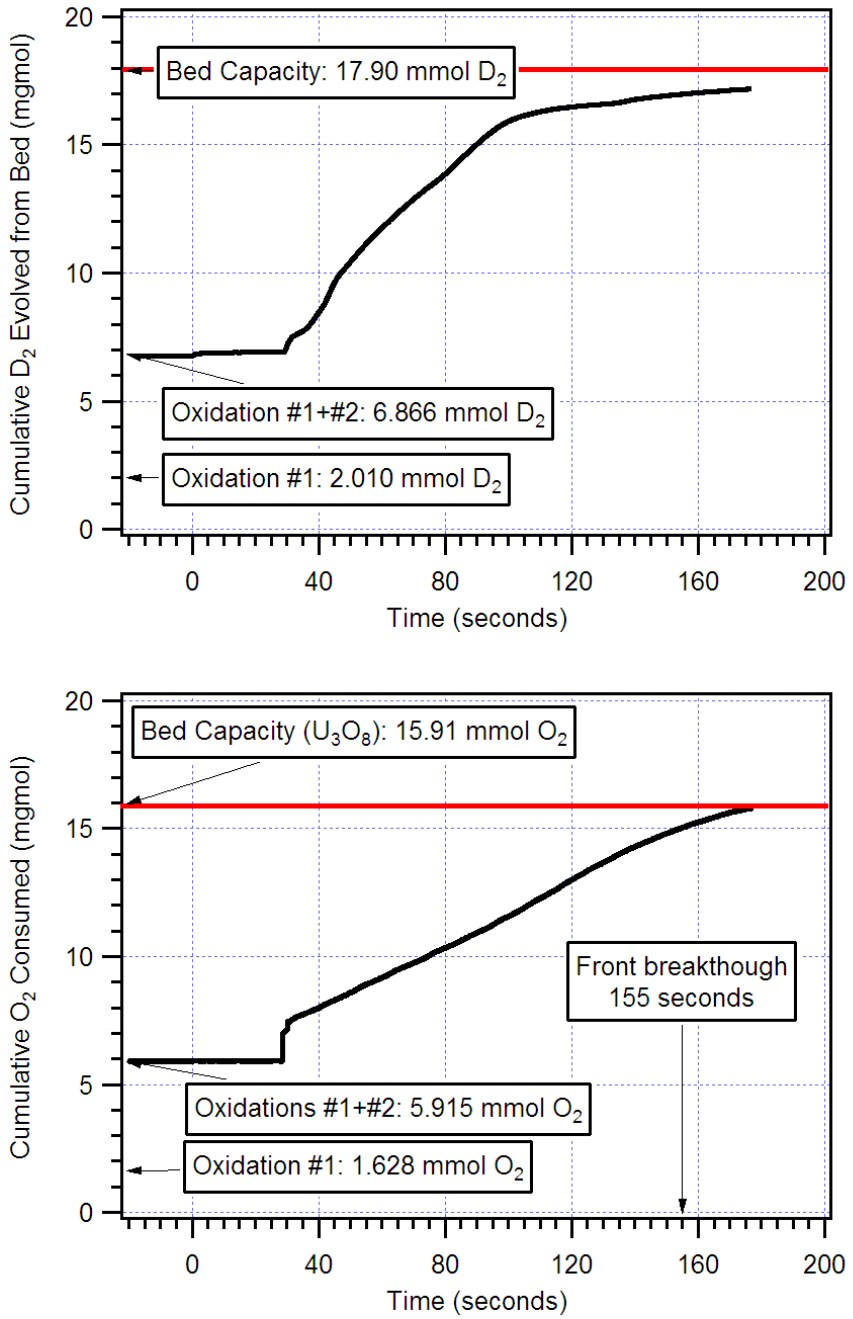

Figure 53: Cumulative D_2 evolved and O_2 consumed during injection-3.

It therefore appears that about 5% of the bed is less accessible to oxygen, due to flow channeling or other non-uniform effects. This is consistent with the overall mass closure error, from PVT mass balance and RGA mole fraction errors, which is also approximately ±5%. Unfortunately, without RGA data from the final portion of the breakthrough, we cannot more precisely quantify the amount of unreacted UD_3 that was present at the time of oxygen breakthrough. All that can be said is that somewhere between 95 and 100% of the UD_3 had been consumed at the oxygen

breakthrough time. One can however conclude that, under these conditions, the final oxide product is nearly all U_3O_8.

The surface-mount thermocouple data are consistent with the gas composition measurements. There is a peak in reactor-surface temperature when O_2 breaks through; presumably because most, if not all, of the UD_3 has been consumed and the bed has stopped generating heat. Beyond 155 s, the reactor cools to the initial, ambient, temperature. The fact that the downstream thermocouple reaches a higher temperature than the upstream thermocouple provides additional evidence that the reaction is occurring at a front that propagates through the bed.

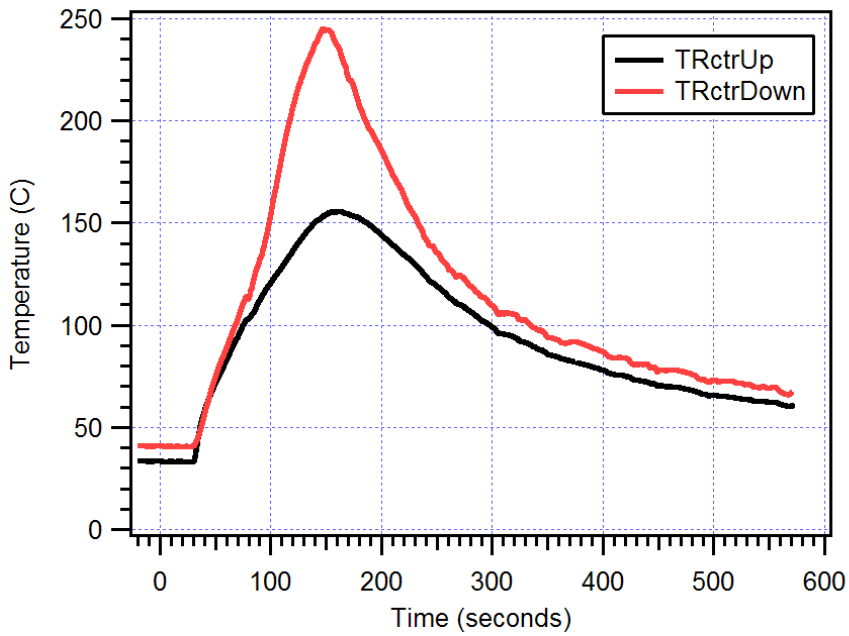

Figure 54: Reactor surface-temperatures during injection-3.

4.2.4.2 Model results

The third oxygen injection experiment used an even larger pressure (171 psia/1.18 MPa) in the oxygen source vessel than the prior two injection experiments. The initial state of the reactor for the third injection was the final state following the second injection (the leading ~38% of the bed was oxide). The large source pressure creates large oxygen flow rates, reaction rates, and temperatures, and significantly more UD_3 decomposition. Furthermore, this experiment made use of a high-pressure helium reservoir to maintain a large oxygen pressure throughout the flow injection process.

Figure 55 shows the temperature, reaction rate, U and UD_3 distributions early in the third oxygen injection simulation (14 s from the beginning of oxygen injection). Similar to the results for injection-2, there is a short development period (not shown here) that leads to a UD_3-oxidation front (Figure 55b) that is confined to a small region adjacent to the wall because near the axis, decomposition has replaced all of the UD_3 with U. The UD_3 decomposition front (Figure 55c) and trailing U oxidation front (Figure 55d) then span most of the width of the bed. A significant

portion of the bed is uranium at this time (Figure 55f). The uranium is formed at the leading edge of this region by decomposition (upper side) and it is consumed by oxidation at its trailing edge (lower side).

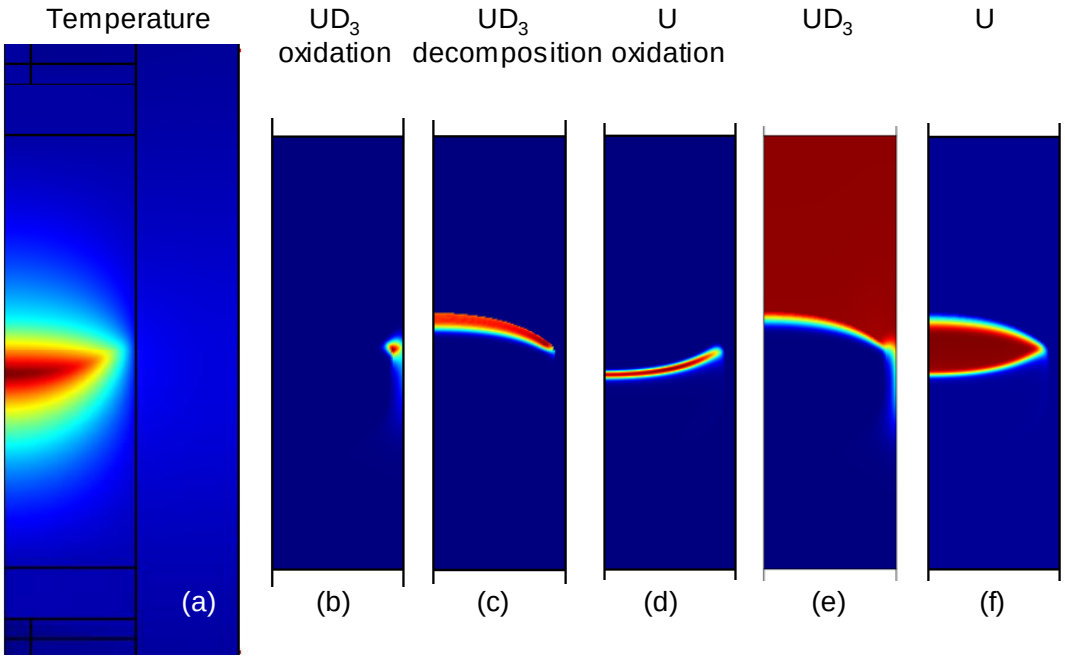

Figure 55: Predictions for the (a) temperature, (b) UD_3 oxidation, (c) UD_3 decomposition, (d) U oxidation, (e) UD_3, and (f) U distributions in the vicinity of the bed, early (*t* = 44 s) in the third oxygen injection experiment.

The pressure decay in the oxygen source vessel is shown in Figure 56a for injection-3. Note that due to the use of a helium reservoir that drives a piston sweep of the oxygen reservoir, the pressure in the latter remains large throughout the injection process. The model did not actually include a piston, rather a source volume equal to the sum of the helium and oxygen reservoir volumes was used, where it must be understood that the flow of oxygen into the reactor stops when the pressure falls below 147 psia (1.01 MPa) corresponding to the injection of an amount of gas that is equal to that initially on the oxygen side of the piston. The model under predicts the rate of pressure decay, indicating the calculated permeability is smaller than the actual value. Figure 56b shows the results for the flow-through experiment that followed injection-3. Here, the model is in excellent agreement with the experiment because the state of the bed is now fully oxidized, one of the conditions for which the model was calibrated.

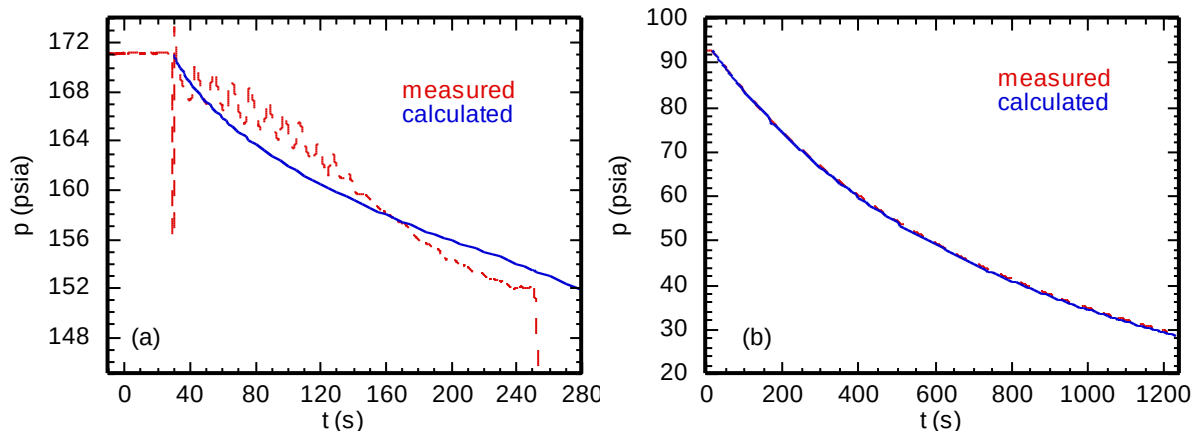

Figure 56: The pressure decay in the gas source vessel (a) during the third oxygen injection experiment, and (b) during the flow-through test that followed it.

The temperature distribution in the bed (on axis) at various times is shown in Figure 57a. The results are similar to those for the prior two oxygen injections, except that the temperatures are much higher here due to the faster oxygen flow rate. Note that the maximum temperature decreases with time not because of a decrease in oxygen flow rate, which is almost constant throughout injection-3, but rather due to the approach to the downstream frit (located at $z = 1.33$ cm), which has a relatively large conductivity. Figure 57b shows the temperature as a function of time at the thermocouple locations. In contrast to the prior two oxygen injections, here the maximum temperature at the upstream location (TC#1) is smaller than that at the downstream location (TC#2), for both the measured and calculated results. This is consistent with a sharp reaction front propagating across the bed, where here the reaction front is closer to the downstream position, making it hotter. There is significant disagreement between the calculated and measure results for the actual shapes of the temperature curves. The cause of this is uncertain, but it is likely related to heat transfer effects in the hardware present in the experiment but absent in the model.

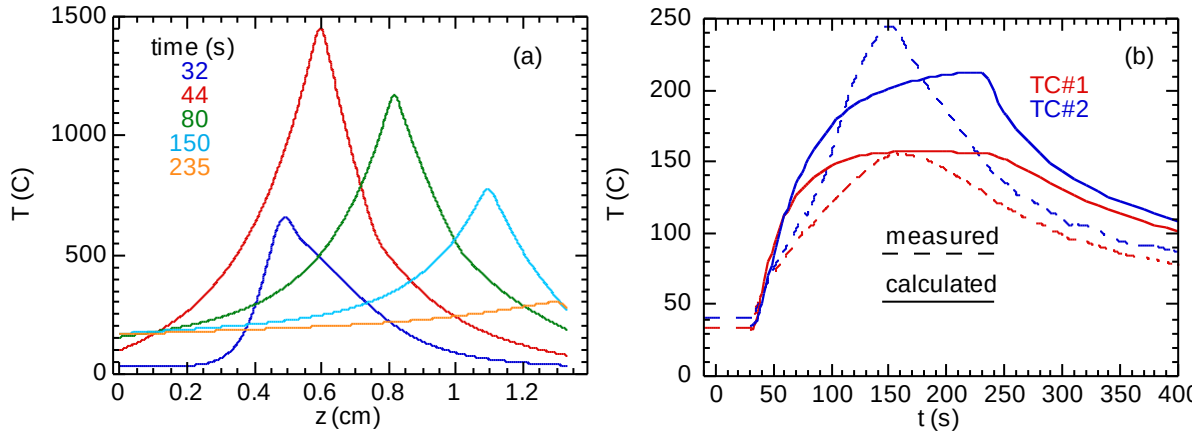

Figure 57: (a) The calculated temperature profiles in the bed on axis at various times, and (b) a comparison of calculated and measured temperatures at the locations of the thermocouples for the third oxygen injection.

Axial profiles of the reaction rates, on axis in the bed, are shown in Figure 58a at various times. UD_3 oxidation is only seen early (t = 32, the injection began at t = 30 s) and late (t = 240), when the temperature is sufficiently low such that decomposition has not depleted all of the UD_3 on axis. The temperature is low at early times because the oxidation reaction has not yet full heated the reactor. It is low at late times because, then, the reaction is near the downstream frit which has a relatively large conductivity. Between these times there is only the decomposition front followed by the U oxidation front. The integral of the reaction rates over the bed are shown in Figure 58b as functions of time, along with the oxygen flow rate (multiplied by ¾). Throughout most of the injection, UD_3 decomposition and oxidation and U oxidation occur. Interestingly, the decomposition rate is the largest at early times. All the reactions stop at t = 250 s because there is no UD_3 or U left. Note that UD_3 oxidation is the last to stop due to the reduction in temperature as the downstream frit is approached. The oxygen flow rate increases after that because the temperature has decreased, leading to decreased gas viscosity and increased density.

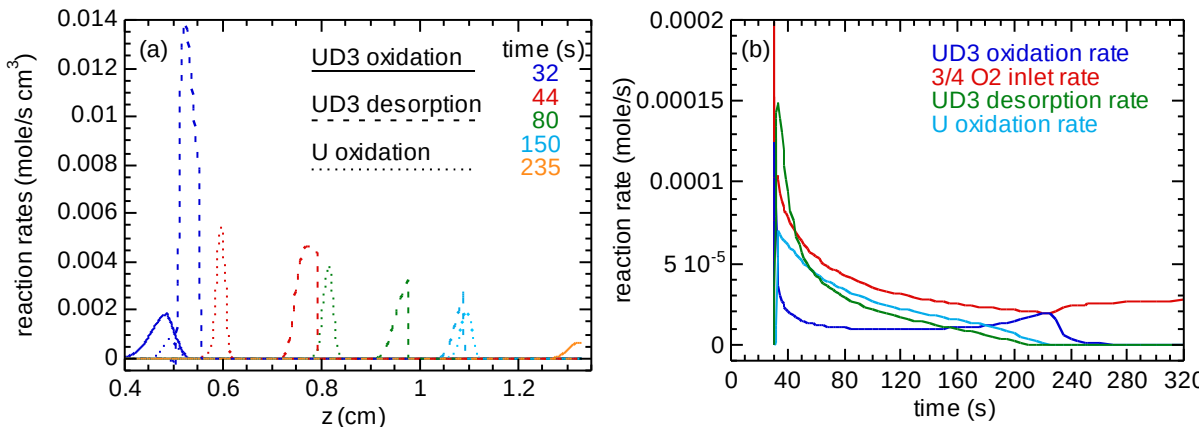

Figure 58: The calculated results for (a) the reaction rates on axis in the bed, and (b) the integral of the reaction rates over the entire bed as functions of time for the third oxygen injection.

The experiments included measurements of the gas composition exiting the reactor[9]. For all except injection-3, that data showed there was no oxygen present. The data for injection-3 is shown in Figure 59. The measured results show that at t = 160 s the gas composition switches from being mostly D_2 to mostly O_2. The calculated result shows similar behavior except it does not happen until t = 220 s. This is consistent with the source pressure results shown in Figure 56a, where the model under predicted the pressure decay rate, and suggests the permeability is under predicted as well. Figure 59b shows the same results, except with a shift in the time scale of the calculated results to allow for an easier comparison to the measured results. The measured rate of the gas composition transition from D_2 to O_2 is well matched by the calculated result. Calculated results using faster and slower reaction rates gave results (not shown here) with faster and slower gas composition transitions, respectively. The agreement seen in Figure 59b gives some confirmation for the kinetic parameters used here.

[9] Here the mole fractions are computed from the RGA signals assuming equal RGA-system response for all gasses. This is not completely accurate (as described in a later section), but is sufficient for the comparisons described below.

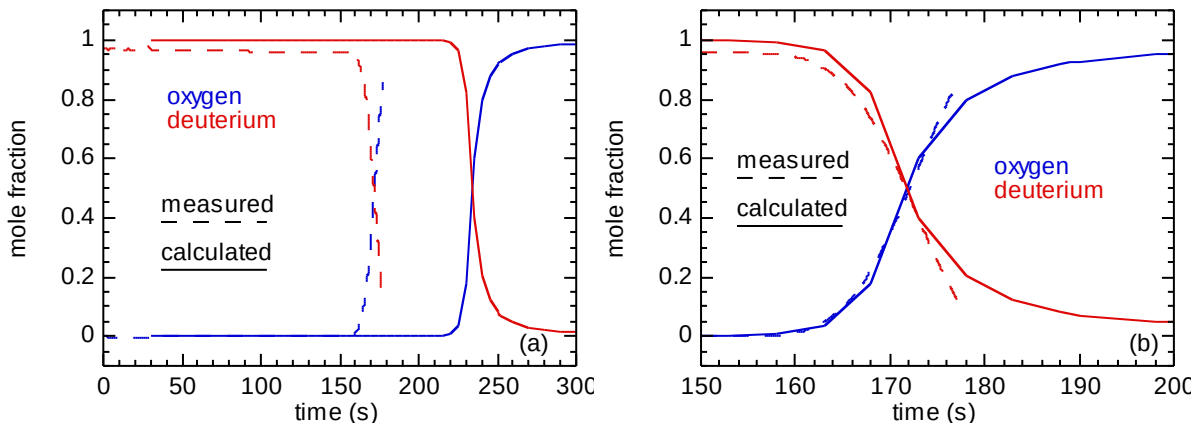

Figure 59: The gas composition exiting the reactor for the third oxygen injection. (a) Results presented using as-measured and as-calculated time scales. (b) Results presented after shifting the calculated time scale to better align with the measured results.

4.2.5 Conclusions from reactor #1

Quite a bit was learned from the three oxygen injections and post-injection flow tests performed on Reactor #1. The most important results are:

- The reaction of UD_3+O_2 is significantly faster than literature reports for U+O_2 near room-temperature (30−40°C).
- Under these conditions, UD_3 will react with O_2 gas and form mostly U_3O_8. No surface passivation was observed. This is different from what Longhurst [4] found for UH_3 + air reactions and is a favorable trait for the reactive thermal decomposition concept.
- Through a combined experimental and modeling approach, it was shown that the oxidation reactions form sharp fronts, especially for large oxygen injection rates. This is understood to happen because the UD_3 + O_2 reaction rate is significantly faster than the oxygen injection rate.
- These reactions consume all of the oxygen, until the bed is almost fully depleted of UD_3. Between 95 and 100% of the bed was reacted to U_3O_8 before significant amounts of O_2 were observed in the effluent gas. This implies that the reaction front progresses through the bed in a more-or-less uniform (one-dimensional) manner; which suggests that the bed is uniform and flow channeling is unimportant.
- Water isotopologs were observed after more than 90% of the bed was oxidized. Their total concentration however was very low, ~0.05%. Therefore, if the UD_3 + O_2 reaction produces water, it is likely a relatively short-lived intermediate. When smaller fractions of the uranium are consumed, as occurs for rapid injections that result in UD_3 decomposition, water yield can be negligible.
- Post-injection flow tests show that the bed mechanically evolves during oxidation; the permeability decreases significantly, presumably due to $UD_3 \rightarrow U_3O_8$ particle expansion.

These results answer a number of the questions posed in Section 4.1.

4.3 Reactor #2 – fast O_2 injection at 30 °C

Reactor #2 was used to explore the bed-preparation process and investigate faster oxygen injection – still with an initial reactor temperature of 30−40°C. It was learned that:

- Three hydride/dehydride cycles are sufficient to produce a uniform bed (discussed previously in section 4.2.1).
- Not surprisingly, for this bed configuration, rapid oxygen injection leads to rapid local heating, which leads to local bed sintering and flow channeling.

4.3.1 Hydride/dehydride cycles

Reactor #2 was used to better understand the bed preparation process. The reactor was loaded with 2.85 g of uranium (three chunks) and eight hydride/dehydride cycles were performed on it. The bed diameter and length are 0.316 (0.803) and 0.526 in (1.336 cm), respectively; yielding a post-hydride porosity of 0.610. Flow measurements, were performed after each hydride cycle. The results were compared and discussed previously in Section 4.2.1.6.

In addition to the flow measurements, the bed capacity was measured. Figure 60 shows the ultimate D/U for the eight hydride cycles.

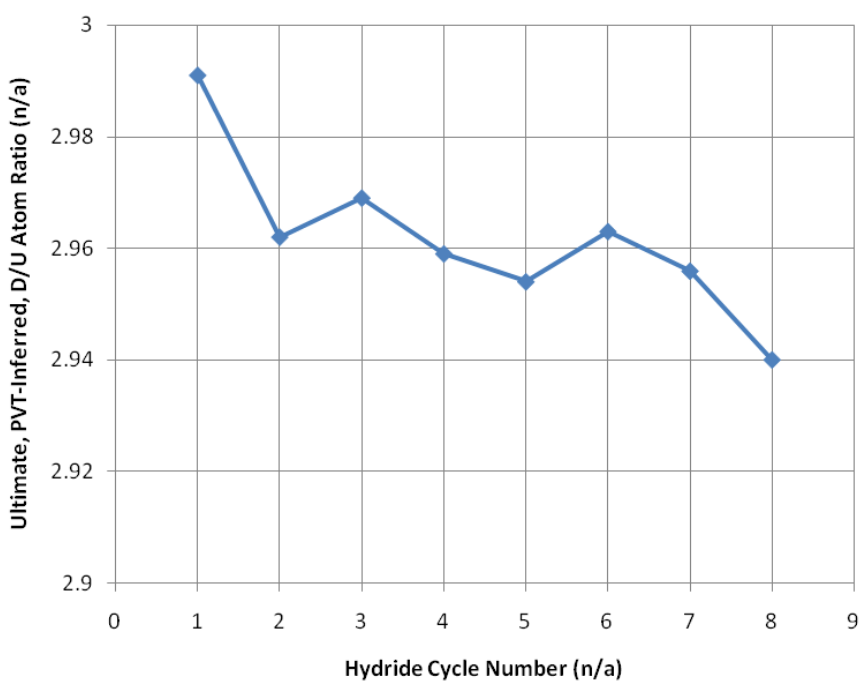

Figure 60: Ultimate D/U vs. hydride cycle number for Reactor #2.

The bed capacity decreases with increasing cycle number, but the decrease is small (about 2% between cycles 1 and 8).

The capacity decrease is believed to be caused by reactions between the uranium metal/hydride and residual contaminant gasses, (H_2O, N_2, CO, O_2, CO_2, etc.) in the system. However, it is also possible that the decrease is due to residual deuterium that is not fully removed during dehydriding. The RGA records, e.g. Figure 20, however, contradict this to some extent. A systematic decrease in capacity with cycle number is more consistent with the contaminant-reaction hypothesis.

4.3.2 O_2 injection-1

The goal for this experiment was to test a significantly faster oxygen injection rate. This allows interrogation of faster UD_3+O_2 reaction rates, and, provided the bed remains intact, observation of more extensive UD_3 decomposition.

For the experiment, 150% of the O_2 needed to fully oxidize the bed to U_3O_8 was injected using a 350 psia (2.413 MPa) helium-driver pressure. This was predicted to convert 100% of the bed to U_3O_8 in just 30 seconds. As before, the plumbing between the reactor exit and receiver was heated to 100°C to facilitate water detection. Finally, thermocouples were mounted in the reactor wall as shown in Figure 61.

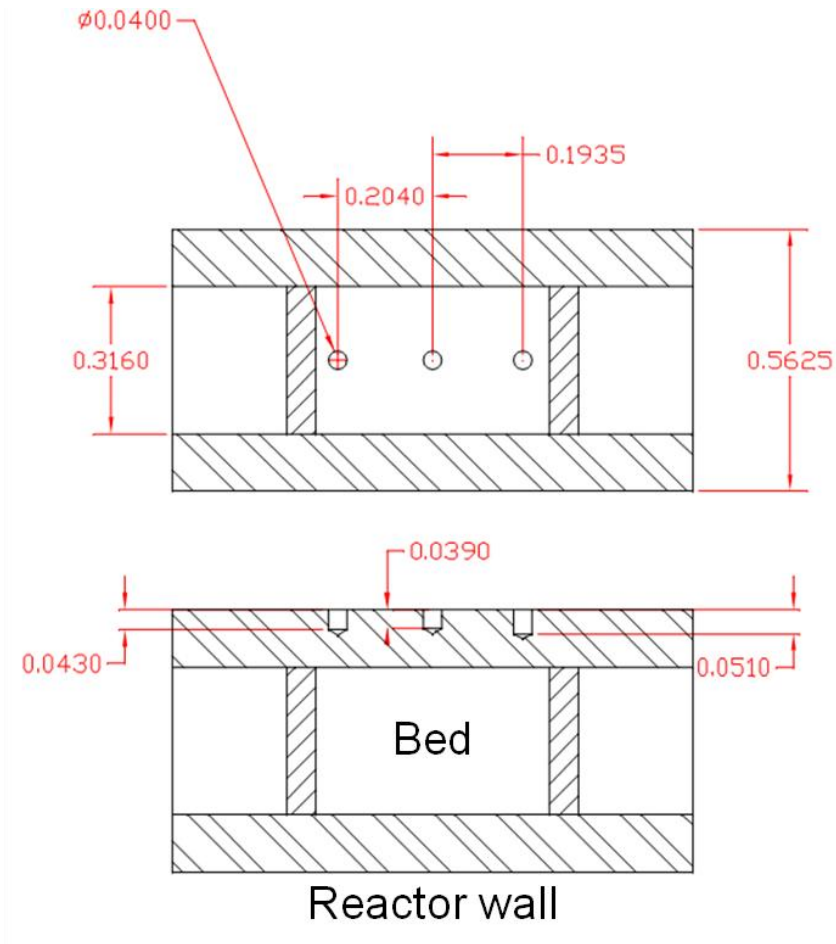

Figure 61: Reactor #2 thermocouple locations (dimensions in inches).

Three 0.032–inch (0.081-cm) -diameter sheathed type-K thermocouples were fixed in the wells with Omegabond-600 air-set ceramic cement.

System pressures are shown in Figure 62.

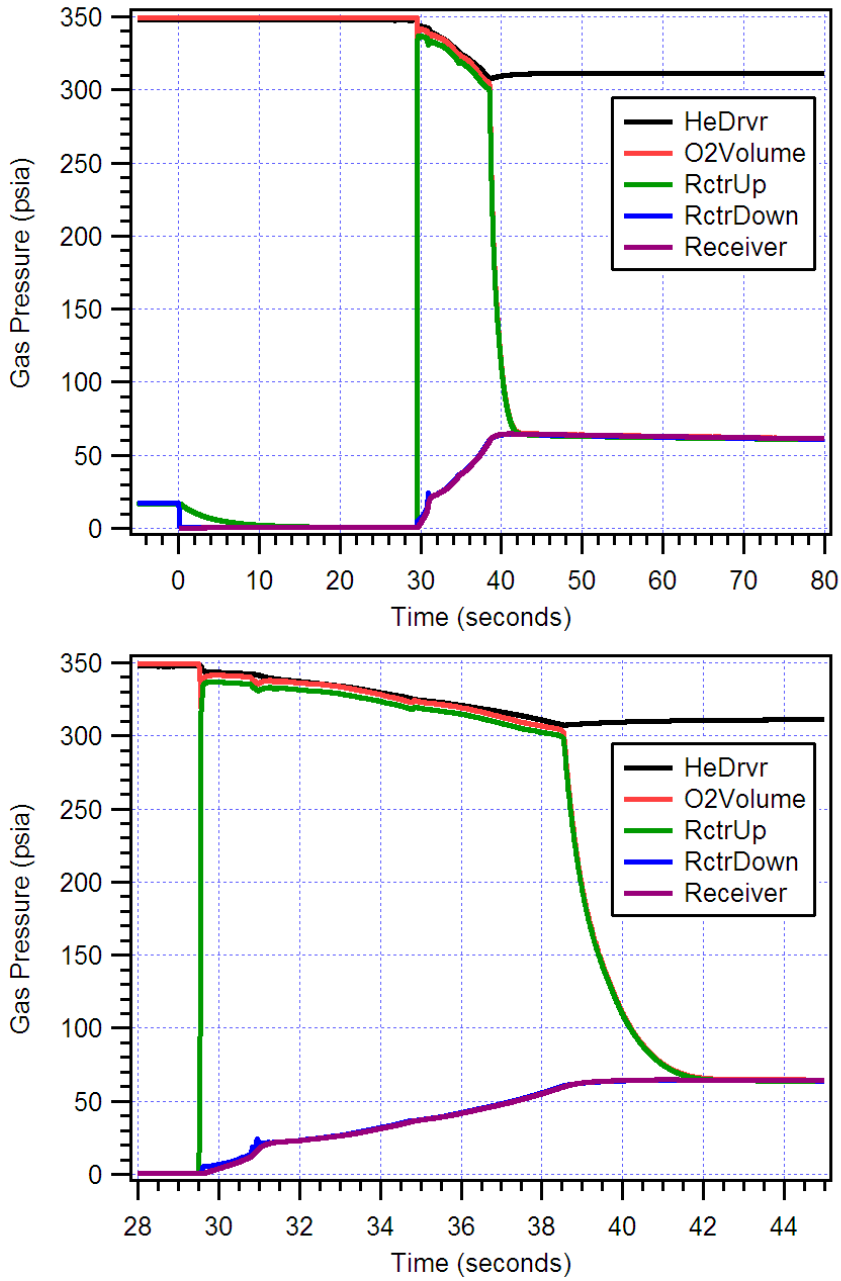

Figure 62: Pressure data from injection-1. The bottom plot shows only the injection portion of the gas transfer (28 to 45 s).

A system model that included oxidation-induced permeability changes but not heat release, predicted that the system would reach pressure equilibrium 63 seconds after injection started.

The actual system reached pressure equilibrium much more quickly, in about 12.5 seconds. Based on this, it was suspected that local sintering had damaged the bed; which lead to flow channeling.

The reactor was radiographed and in Figure 63 it is clear that significant density non-uniformities had developed, presumably caused by local sintering.

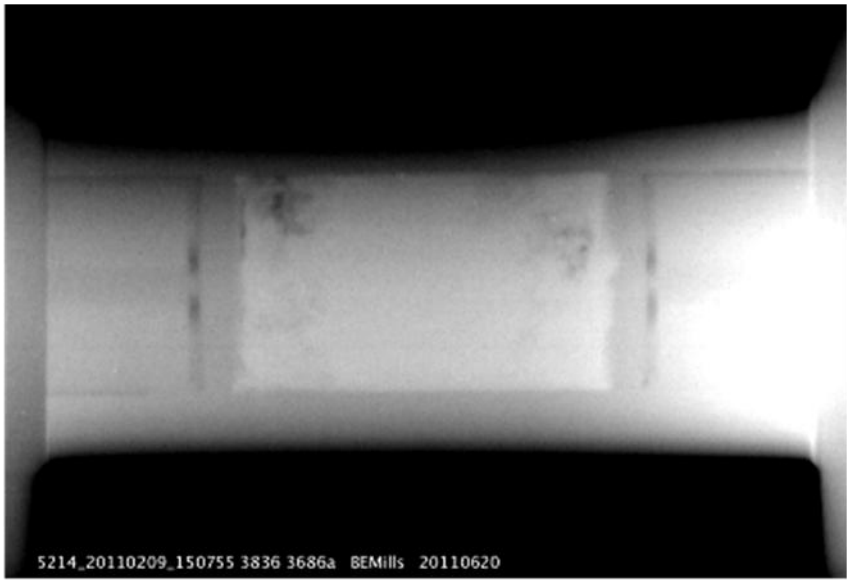

Figure 63: Radiograph of Reactor #2 after injection-1. Flow direction is from left to right.

A deuterium flow test was performed after injection-1. The bed had a greatly decreased flow resistance. The blowdown time was reduced from the 200 seconds for the virgin bed to about 10 seconds. This result also suggests flow channeling and therefore a non-uniform bed.

Because flow channeling was significant, not much can be said about the reaction beyond the observation that, at a 30−34°C initial temperature, O_2 reacted quite promptly with the UD_3 bed. After the reaction started, the heat release was sufficient to cause local thermal run-away leading to local bed sintering. Close inspection of the pressure traces (Figure 64) can give some indication of the promptness of the reaction.

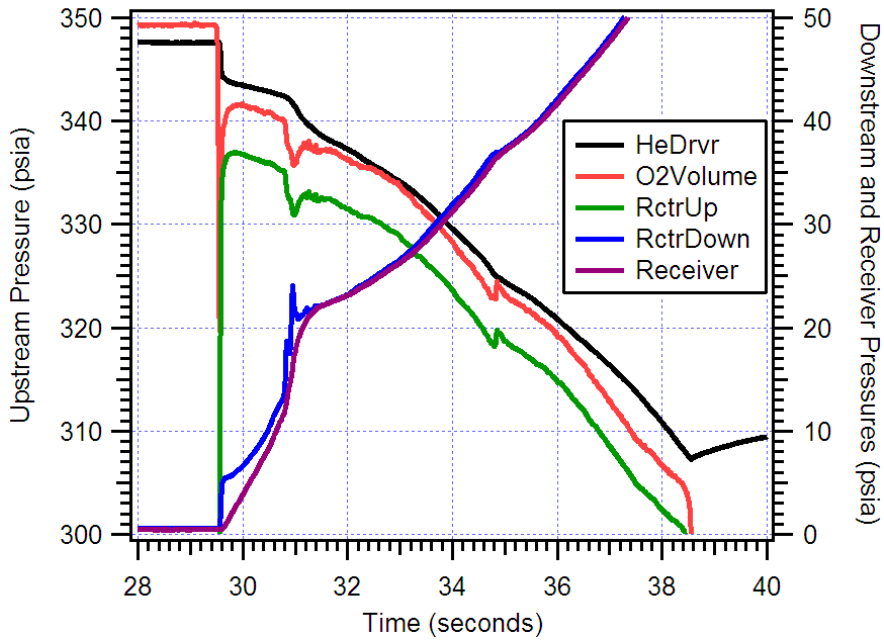

Figure 64: A detail-view of injection-1 pressure data.

At about 31 seconds, 1.25 seconds after injection starts, there is a sharp increase in RctrDown and a sharp decrease in RctrUp. This may indicate either: (1) the start of significant thermal run-away (rapidly increasing D_2 release and O_2 consumption), or, (2) the development of a sizeable flow channel. In either case, something significant, which was caused by UD_3 + O_2 reaction, happened 1.25 seconds after injection started. This implies that, at 30−34°C, the incubation time for the UD_3 + O_2 reaction is, at most, 1.25 seconds[10].

Because the transfer event lasted only 8 seconds, not much longer than the RGA response-time, the RGA signals are too convoluted with the RGA-system response-function to be of much use in finding the total quantities of transfered gas. Therefore, a gas sample was taken and sent to Chris Harvey at LLNL for mass-spectrometric analysis with results listed in Table 3.

Table 3: Reactor #2 injection-1 LLNL gas analysis results

Component		Concentration (mole-%)
Hydrogen	H_2	0.42
Hydrogen deuteride	HD	0.51
Deuterium	D_2	40.25
Helium	He	<0.2
Nitrogen	N_2	0.45
Oxygen	O_2	58.37
Argon	Ar	<0.02

[10] If the RGA response were sufficiently fast, it could be used to distinguish between cases 1 and 2. Unfortunately, the 90%-response time for O_2 is 5.0 seconds, too-slow for this 8-second transfer event.

The data in Table 3 are combined with PVT measurements to estimate the receiver contents: 9.12 mmol-D_2 and 12.9 mmol-O_2. A system mass balance indicates that 8.84 mmol-D_2 and 10.42 mmol-O_2 are occluded, presumably in the bed. The following global reaction is postulated

$$a\mathrm{UD}_3 + b\mathrm{O}_2 \rightarrow c\mathrm{U}_3\mathrm{O}_8 + d\mathrm{U} + e\mathrm{UD}_3 + f\mathrm{D}_2 + g\mathrm{O}_2, \tag{32}$$

where *a*-*g* are stoicheometric coefficients. Using the U, D, and O species balance equations the three unknowns, *c*, *d*, and *e*, may be determined: $c = 2.61$, $d = -1.73$, and $e = 5.89$. The $d < 0$ result is non-physical indicating either (1) D_2 or O_2 species-closure measurement-errors of ~ 10%, or, (2) the assumed reaction is incorrect. In this case, because the required measurement error is of similar magnitude as the measurement uncertainty, we believe that measurement error is responsible for the $d < 0$ result.

Unfortunately, this experiment led to local bed sintering, flow channeling, and little useful data. Options to mitigate this include:

1. Do not change the experiment, only evaluate the promptness of the reaction.
2. Dilute the UD_3 with an inert material (e.g. Al_2O_3). To be effective, this will require mixing on a small length scale, perhaps ~100 μm.
3. Dilute the O_2 with an inert gas (e.g. Ar, He, or even H_2).
4. Make the bed thinner/smaller (to increase the heat removal rate). The bed would have quite thin, approaching ~ 1 mm.
5. Inject only a small amount of O_2. Some of the bed should still be intact.
6. Change the UD_3 powder surface area; use massive UD_3 particles. Monolithic UH_3 has been made by solidifying molten hydride [43]. It requires pressures around 10,000 psia (69 MPa) and temperatures ~1000°C.

All of the above options, except for #1, require substantial work. Therefore for Reactor #3, we chose to continue with the flow-through bed configuration and test if the UD_3 + O_2 reaction is comparably prompt at low temperature (−80°C). If the reaction kinetics has slowed sufficiently, then all of the injected O_2 may pass through the bed without reacting.

4.4 Reactor #3 – Fast O_2 injection at −80°C

Reactor #3 was used to investigate fast oxygen injection at low temperature. An initial reactor temperature of −80°C was selected for the injection. It was learned that the UD_3+O_2 reaction is still prompt at an initial reactor temperature of −80°C and that the promptness is comparable to 30°C initial temperature.

The reactor was loaded with 2.75 g of uranium (two chunks) and three hydride/dehydride cycles were performed to condition the bed. The bed diameter, length, and post-hydride porosity are

0.316 in (0.803 cm), 0.500 in (1.27 cm), and 0.604 respectively. Flow measurements, were performed after each hydride cycle. The results were compared and discussed in Section 4.2.1.6.

Reactor #3 had similar bed geometry to reactors 1, 2, and 4. However, the reactor housing design was different. In an attempt to simplify reactor assembly, a custom mini-conflat sealed housing was used (see Figure 65).

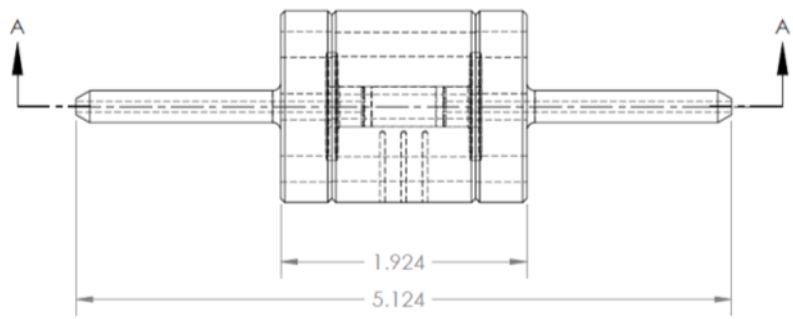

Figure 65: Reactor #3, the mini-conflat design.

This reactor design was subsequently abandoned because the temperatures used for bed dehydriding, ~400°C, partially anneal the mini-conflat gaskets. Consequently, leaks develop when the reactor is cooled back to room temperature. Fortunately for reactor #3 the leaks were slow and the bed was not contaminated with air during processing because the reactor was stored at higher-than-atmospheric pressure. However, for subsequent experiments this housing design was abandoned.

4.4.1 O_2 injection-1

The injection conditions matched reactor #2; 150% of the O_2 needed to fully oxidize the bed to U_3O_8 was injected using a 350 psia (2.413 MPa) helium-driver pressure. The plumbing between the reactor exit and receiver was heated to 100°C to facilitate water detection. Thermocouples were mounted in the reactor wall. The thermocouple wells are visible in Figure 65.

The reactor was cooled to −80°C using the cold-chamber shown in Figure 6. The gas pre-conditioner described in Section 2.4.2 had not been developed yet and therefore was not used for this test. However, the frit directly upstream of the bed has sufficient thermal mass and fluid-solid contact time that, at the time of $UD_3 + O_2$ reaction initiation (29.6 s), the estimated inlet gas temperature is below −60°C. The gas temperature can be estimated by assuming that: the frit is adiabatic, its temperature is uniform, and the incoming gas and frit are at thermal equilibrium. Figure 66 shows the estimated gas temperature at the bed inlet (after exiting the upstream frit) during injection-1.

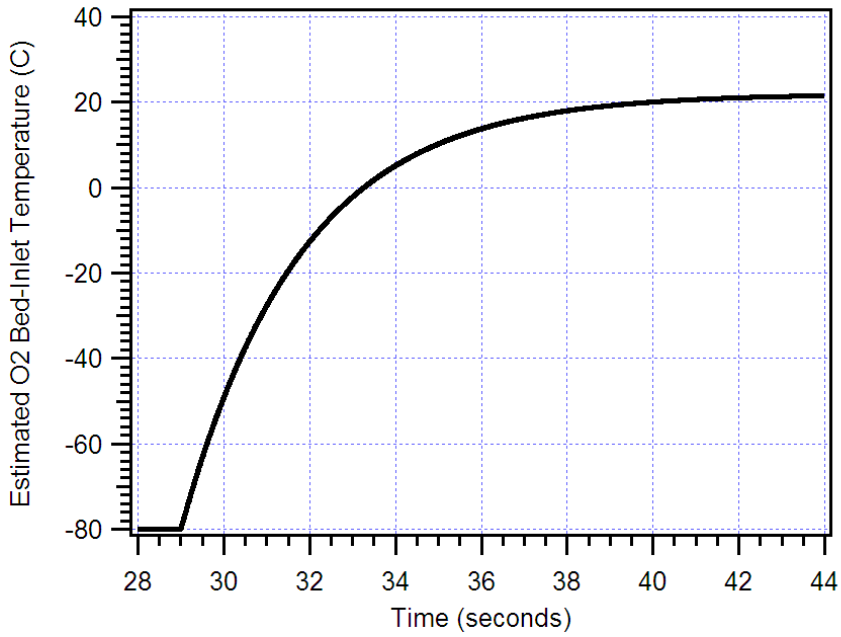

Figure 66: Estimated gas temperature at the bed inlet during injection-1.

The pressure traces (Figure 67) look similar to Reactor #2 injection-1. AO1 was closed at 300 seconds and AO2 was closed at 360 seconds. Pressure equilibrium is reached about 11 seconds after injection starts. This is similar to Reactor #2 and faster than predicted for an intact bed.

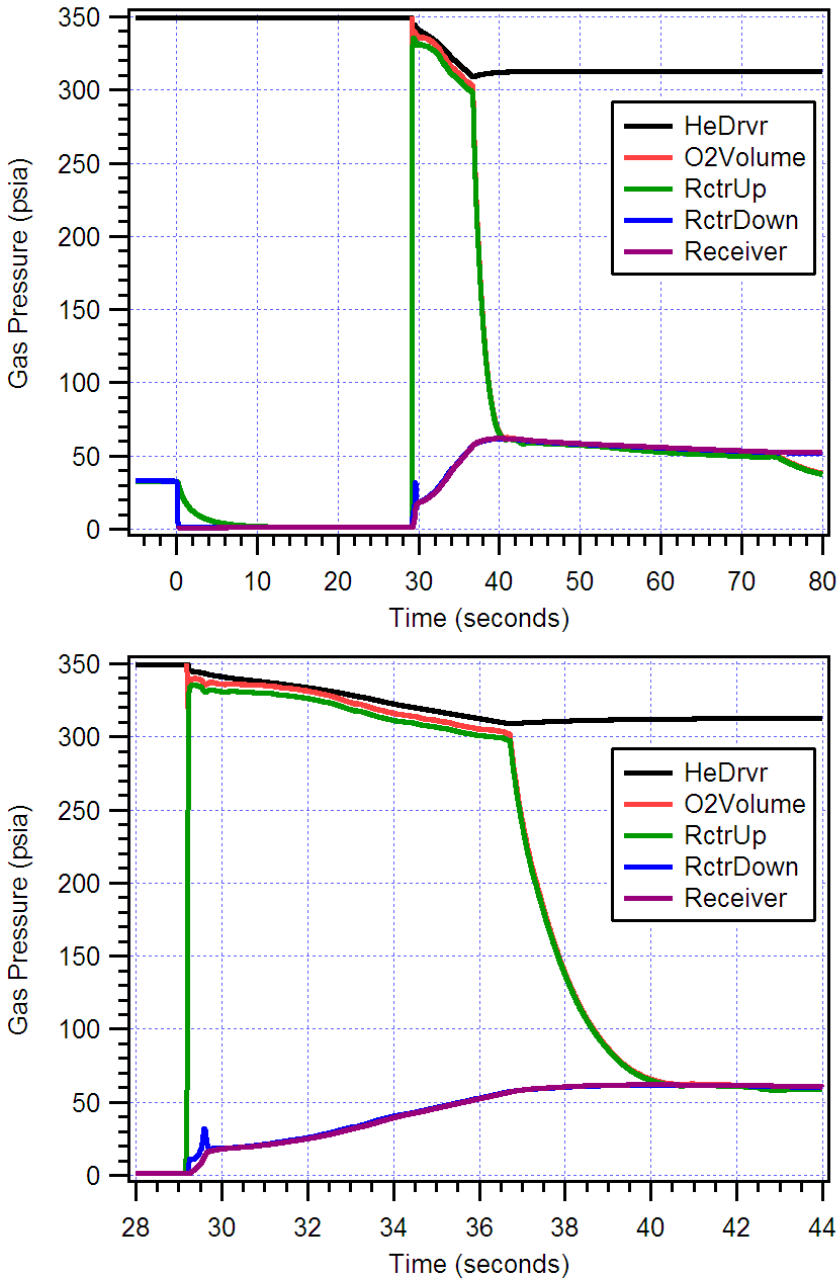

Figure 67: Pressures during Reactor #3 injection-1.

The reactor was radiographed (Figure 68) and it is again clear that significant density non-uniformities had developed; presumably caused by local bed sintering.

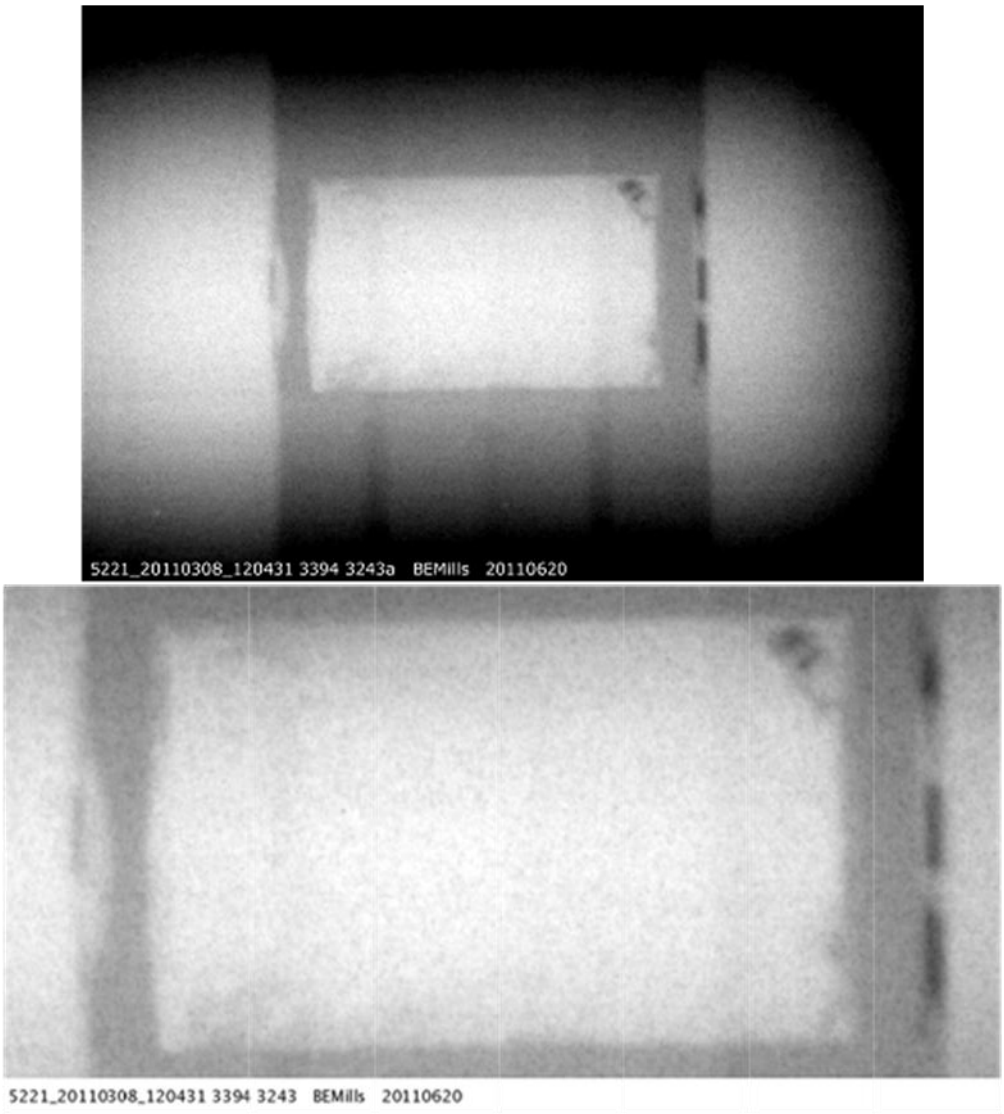

Figure 68: Reactor #3 after injection-1. Flow direction is right to left.

As with reactor #2, not much can be said about the reaction beyond the observation that, at −80 to −60°C initial temperature, O_2 reacts quite promptly with UD_3. As before, after the reaction started, the heat release was high enough to cause local thermal run-away leading to local bed sintering. Close inspection of the pressure traces in Figure 69 gives some indication of the promptness of the reaction.

At 29.6 seconds, about 0.36 s after injection began, there is a sharp increase in the downstream pressure and a sharp decrease in the upstream pressure. This is very similar to reactor #2. Something significant happened in the bed and it was caused by the UD_3+O_2 reaction. Therefore, at −80 to −60°C, the incubation time for the UD_3 + O_2 reaction is, at most 0.36 seconds; comparable to the <1.25 s incubation time observed at 30°C. It therefore appears that the UD_3 + O_2 reaction remains quite prompt at significantly reduced temperatures.

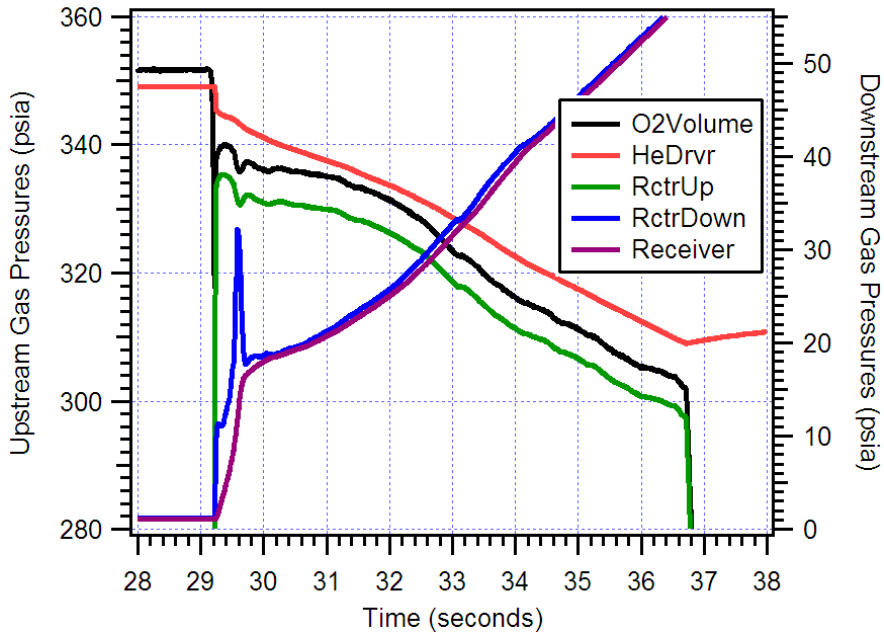

Figure 69: Detail view of pressures during injection-1.

Because the transfer event lasted only 8 seconds, the RGA data are of little use in finding the total quantities of transferred gas. A gas sample was taken and sent to Chris Harvey at LLNL for analysis with results listed in Table 4.

Table 4: Reactor #4 injection-1 gas analysis

Component		Concentration (mole-%)
Hydrogen	H_2	0.80
Hydrogen deuteride	HD	0.10
Deuterium	D_2	33.07
Helium	He	
Nitrogen	N_2	0.45
Oxygen	O_2	66.40
Argon	Ar	

This was combined with PVT measurements to give the receiver contents, 4.90 mmol-D_2 and 9.82 mmol-O_2. A system mass balance indicates that 12.43 mmol-D_2 and 13.78 mmol-O_2 are occluded, presumably in the bed. As before, one may postulate a global reaction (32). It is found that c = 3.45, d = −7.07, and e = 8.28. Similar to Reactor #2, d < 0, which is non-physical, indicating that either: (1) D_2 or O_2 species-closure measurement-errors of ~160%, or, (2) the assumed reaction is incorrect. In this case, unlike Reactor #2, the required measurement error is much larger than the estimated measurement uncertainty. Therefore, it is believed that in this case, the assumed reaction is incorrect; however, an appropriate reaction is currently unknown. This difference between reactors 2 and 3 could be an indicator of significant differences in the UD_3+O_2 reaction at initial reactor temperatures of 30 and -80 °C. However, the difference could

also be reactor-to-reactor variation caused by a highly non-uniform bed-reaction environment. More tests would be needed to confirm either hypothesis.

In any case, the observation that the UD_3+O_2 reaction remains quite prompt even at −80°C is encouraging. It implies that if the heat generation can be managed, then a fast hydrogen generation system could be designed using uranium hydride plus oxygen reactive thermal decomposition.

A possible next step is to investigate oxygen dilution as a reaction management scheme (i.e. injecting a mixture of O_2 diluted with H_2). However, preliminary modeling showed that even with the additional heat transport provided by the flowing H_2 diluent, local heat transport rates are still much smaller than local heat generation rates. Consequently, the diluent will only be effective in managing the heat release if it slows the oxygen to hydride-surface reaction by blanketing the hydride particles. This blanketing effect may be difficult to balance against the desire to retain all injected oxygen in the bed, but we do not yet have a clear concept of its magnitude, so experiments are required, and are recommended for future work.

4.5 Reactor #4 – HD exchange experiments

A set of hydrogen isotope exchange tests were performed on reactor #4. The intent of these tests was to measure uranium hydride H/D isotope exchange kinetics. Hydrogen isotope separation systems based on uranium hydride beds have been proposed by others [16]. However, very little isotope exchange kinetic data is available and therefore it is impossible to design an optimal separation system. The most applicable published work is a set of 1954 measurements made by Bigeleiesen and Kant [17]. In addition to this, a few sparsely documented experiments were performed in the 1980s by Paul Coronado of Sandia National Labs-CA.

The goal of the experiments was to generate data that can be used to infer uranium hydride isotope exchange rates; similar to what Melius and Foltz [18] did with palladium hydride. A fixed-bed reactor configuration is ideally suited for such a study.

4.5.1 Reactor #4 preparation

Reactor #4 was loaded with 2.78 g of uranium (two chunks) and three hydride/dehydride cycles were performed to condition the bed. The bed diameter and length are 0.316 in (0.803 cm) and 0.471 in (1.196 cm), respectively, giving a post-hydride porosity of 0.575. Flow measurements were performed after each hydride cycle. The results were compared and discussed in Section 4.2.1.6.

The reactor housing design was identical to Reactors #1 and #2. Thermocouples were mounted in the reactor wall, similar to Reactor #2 (Figure 61).

4.5.2 RGA calibration

Before the test-series, the RGA was calibrated with a 10.1% H_2, 40.4% HD, 49.4% D_2 gas mixture. The known mole fractions were combined with the measured RGA signals to compute

relative sensitivity factors [23]. The relative sensitivity factors are found by solving the following two equations simultaneously:

$$\chi_{H_2} = \frac{S_{H_2} I_{H_2}}{S_{H_2} I_{H_2} + S_{HD} I_{HD} + S_{D_2} I_{D_2}}, \tag{33}$$

and

$$\chi_{HD} = \frac{S_{HD} I_{HD}}{S_{H_2} I_{H_2} + S_{HD} I_{HD} + S_{D_2} I_{D_2}}, \tag{34}$$

where S_i is the relative sensitivity factor for species i, I_i is the raw RGA signal for species i, and χ_i is the known mole fraction of species i. Only two equations are required, because $\chi_{H_2} + \chi_{HD} + \chi_{D_2} = 1$, so only 2 of the 3 S_i are independent. Consequently, S_{D_2} can be freely defined; we selected $S_{D_2} = 1.0$.

S_i are functions of upstream pressure [23]. Figure 70 shows the measured sensitivity factors for this RGA and capillary system.

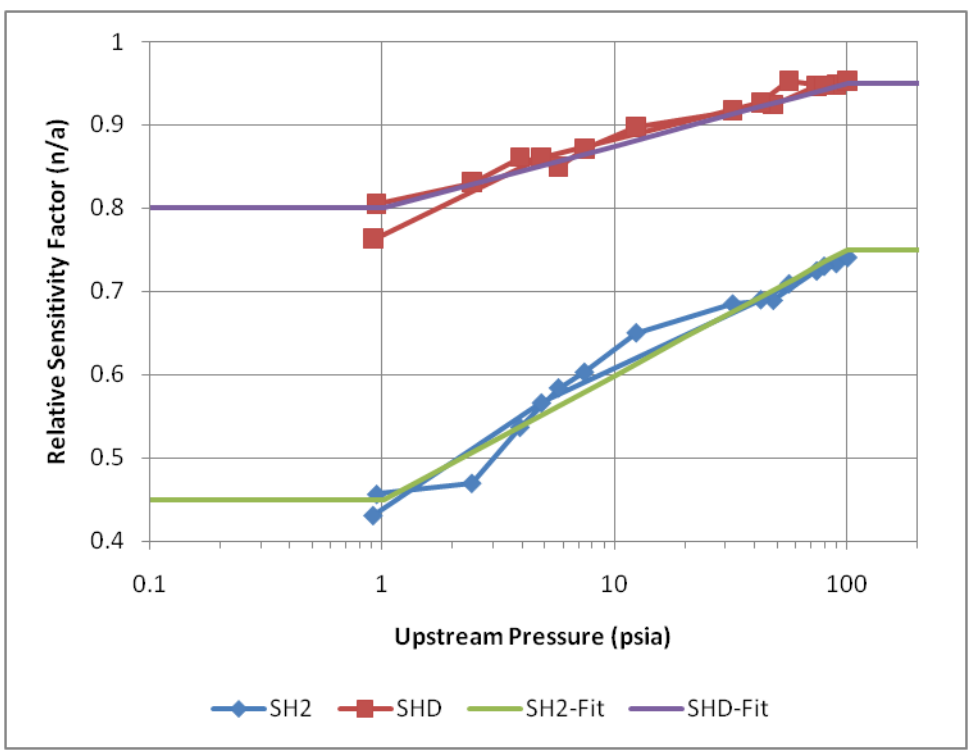

Figure 70: Measured relative sensitivity factors and best-fit curves.

The sensitivity factors were validated with a different, known, H_2+HD+D_2 gas mixture. Figure 71 shows the results.

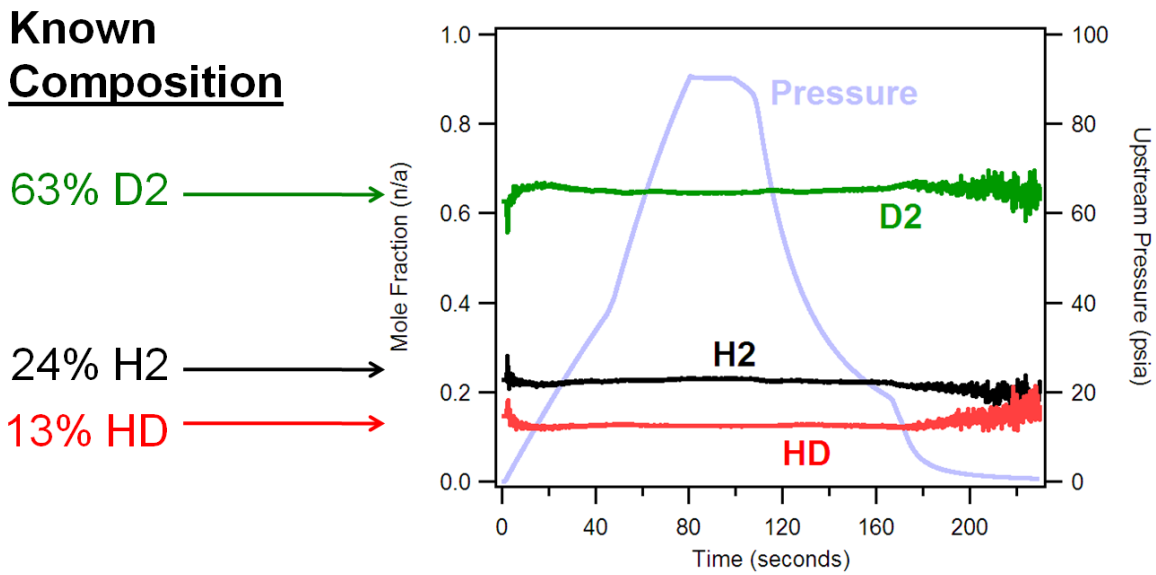

Figure 71: Sensitivity factor validation test

When the upstream pressure is above 5 psia, the RGA error is less than approximately 1%.

4.5.3 Isotope exchange tests at 25, 100, 250°C.

Isotope exchange tests were conducted; in both UD_3 + H_2 and UH_3 + D_2 configurations, and at 25, 100, and 250°C initial temperature. In all tests, the sweep ratio[11] was fixed at 1.4 and the sweep volume was fixed at 45.0 cm^3; giving a sweep time of approximately 60 seconds. In all tests, the sweep volume initial-pressure was 280 psia (1.93 MPa) and the receiver initial-pressure was vacuum, ~100 mtorr.

All of the exchanges were incomplete; i.e. some bed-isotope was not liberated. Therefore, after a test, two or three additional exchange sweeps were performed at 250°C to reset the bed to a single isotope in preparation for the next test. The reactor overpressure gas was sampled after the reset sweeps to confirm that the bed did indeed contain a single isotope.

Between the first test, UD_3 + H_2 at 26°C, and the final test, a repeat of UD_3 + H_2 at 26°C, the bed was swept 39 times. Comparing tests 1 and 39 shows that the global bed exchange rate decreased by about 25%. This observed decrease is small enough compared to temperature-induced rate changes to be neglected[12].

In test-1 some gas-to-solid isotope exchange was observed. Effluent mole fractions and the PVT-derived receiver fill rate are shown in Figure 72.

[11] The ratio of moles-of-gas swept through the bed to moles-of-gas stored in the solid hydride bed.
[12] The global bed exchange rate changes by approximately a factor of 4 between 30 and 100 °C.

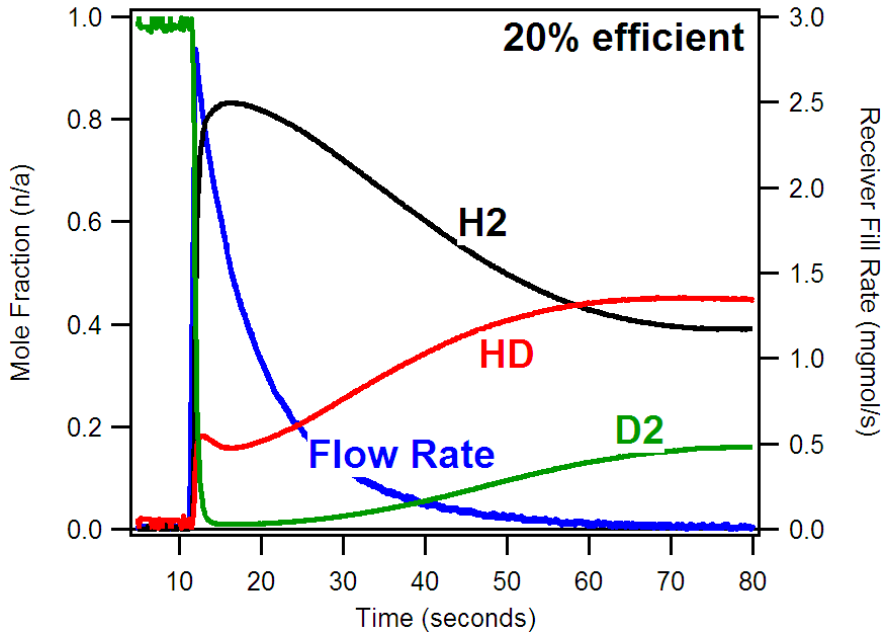

Figure 72: Reactor #4 exchange test-1. Beyond 80 seconds back-mixing affects the RGA data.

At zero seconds AO2 is opened and the reactor overpressure (nearly all D_2) vents into the receiver. At 12 seconds, AO1 opens and the H_2 sweep begins. Because the local exchange rate is much slower than the local flow rate, most of the H_2 passes through the reactor without exchanging. A portion of the H_2 partially exchanges, forming HD, and a smaller fraction exchanges completely, forming D_2. As the flow rate decreases, gas-to-solid exchange has more time to complete and therefore the H_2 mole fraction decreases and HD and D_2 increase. At the end of the test (pressure equilibrium), species mass balances indicate that only 20±1% of the D initially on the bed has been transferred to the receiver[13].

Nearly identical tests were run at initial reactor temperatures of 25, 100, and 250°C; in both $UD_3 + H_2$ and $UH_3 + D_2$ configurations. The gas pre-conditioner, described in Section 2.4.2, was used to pre-heat the sweep gas to the initial reactor temperature. The results are summarized below.

[13] The uncertainty, ±5% of the measured efficiency, is estimated from the overall mass-closure error, 3%, and an estimate of the RGA data interpretation error, 2%.

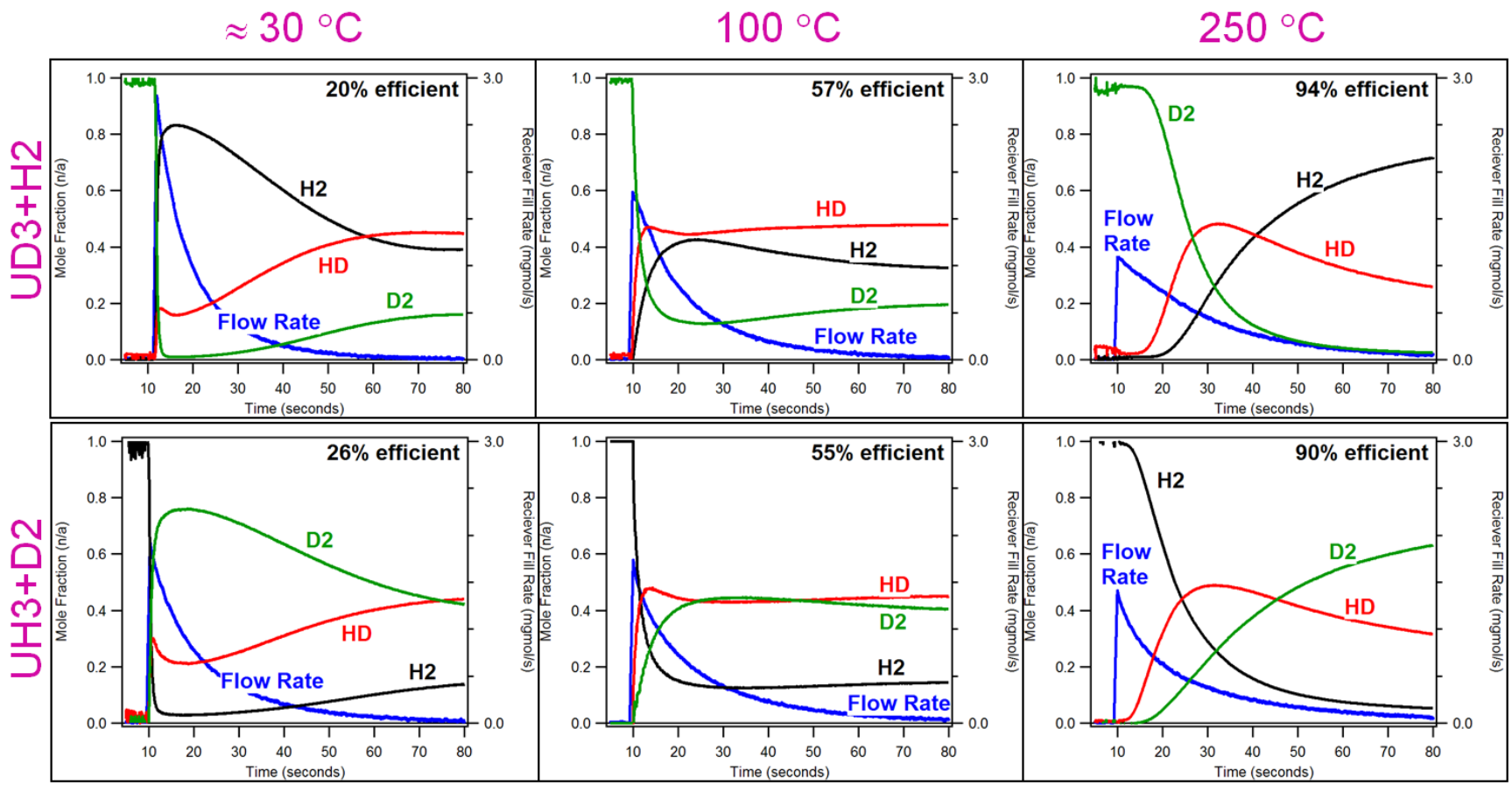

Figure 73: Isotope exchange results. Plots are arranged by temperature (columns) and exchange-direction (rows). Test-1's (UD_3 + H_2) initial temperature was 26°C while test-6's initial temperature was 39°C. In the other cases, the initial temperatures match to within 2°C.

It is apparent that, between 30 and 250°C, the gas-to-solid isotope exchange rate increases with temperature. This is confounded somewhat by the flow rates; which decrease with temperature due to increasing gas viscosity and decreasing gas density in the bed. Nevertheless, close inspection of the mole fraction curves shows that between 30 and 250°C the local exchange rate increased from much slower than the flow rate (30°C), to much faster than the flow rate (250°C). A modeling study is needed to better separate temperature and flow rate effects.

It is also apparent that, between 30 and 250 °C, exchange rates are similar for the $UD_3 + H_2$ and $UH_3 + D_2$ configurations. Gas viscosity differences between H_2, HD, and D_2 alter the flow rates and therefore complicate interpretation somewhat. However, these differences are small at 100°C; because the effluent gas compositions are similar. It is here that one can most directly compare $UD_3 + H_2$ and $UH_3 + D_2$ exchange rates. The data show that the exchange rates are very similar.

The reasonably rapid increase in exchange rate with temperature, the similarity of $UD_3 + H_2$ and $UH_3 + D_2$ rates, and the fact that we did not significantly poison the exchange in 39 exchange-sweeps, all suggest that intra-particle diffusion[14] limits the overall rate of gas-to-solid isotope exchange.

It is understood that gas-to-solid isotope exchange happens in 3 steps, illustrated below.

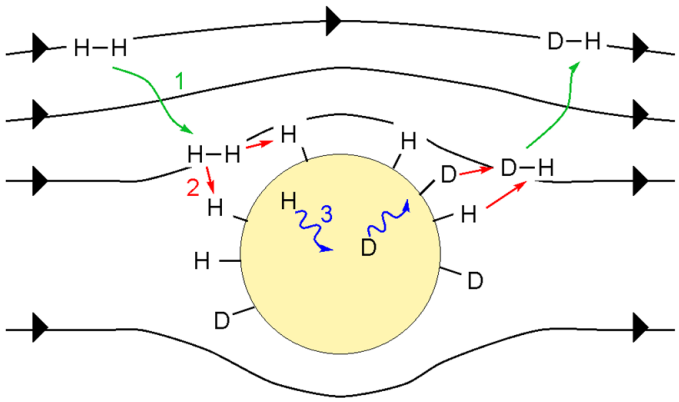

Figure 74: Conceptual picture of gas-to-solid isotope exchange

The steps are:

1) Bulk gas to near-surface-gas transport; a fluid mechanical process, described by a mass transfer coefficient (film coefficient).
2) A chemical reaction between the gas and solid-surface that dissociatively binds H_2.

[14] That is, diffusion of hydrogen/deuterium inside the hydride/deuteride particles.

3) Transport of hydrogen inside a particle; a solid-phase diffusion process. The mechanism may be vacancy-diffusion [44-45], or, possibly a more unusual activated-diffusion process involving exotic uranium-hydrogen compounds that have been identified recently [46-47]. Whatever the mechanism, the transport process can be described by an effective diffusivity and particle diameter.

Rate expressions exist for each step; Refs. [48-49] give examples for comparable processes in palladium hydride and $LaNi_3Al_2$ hydride.

Because the steps happen sequentially and are reasonably independent, one can combine their transport resistances as follows, $R_{eff}^{-1} = R_1^{-1} + R_2^{-1} + R_3^{-1}$, where R_{eff} is the overall exchange rate and R_i is the rate for each step. Hence, if one step is much slower than the others, it will control the overall gas-to-solid exchange rate.

For this system, a clever experiment can isolate steps 1 and 2 from step 3. If a mixture of $H_2 + HD + D_2$ is swept through a bed that is in H/D isotope composition-equilibrium with the gas, then there will be no net gas-to-solid isotope exchange. However, the bed-surface will still catalyze the $H_2 + D_2 \leftrightarrow 2HD$ reaction. This is useful because the rate of the $H_2 + D_2 \leftrightarrow 2HD$ reaction is controlled by steps 1 and 2. Hence, if a sweep gas that is not at $H_2 + D_2 \leftrightarrow 2HD$ equilibrium is used, then by comparing the effluent composition to the predicted $H_2 + D_2 \leftrightarrow 2HD$ equilibrium composition, one can compare the combined rate of steps 1 and 2 with the gas flow rate. The combined rate of steps 1+2 can then be compared to the overall gas-to-particle exchange rate, which includes steps 1+2+3.

It is known already that the overall rate of gas-to-particle exchange (steps 1+2+3) is much lower than the gas flow rate at 25°C. Therefore, if it is found that steps 1+2 are faster than the gas flow rate, it is clear that step 3 (intra-particle diffusion) is rate-limiting.

A mixed isotope sweep experiment was performed at 26°C using a 30%:70% H:D gas mixture purchased from Matheson Tri-Gas. At time of purchase, about 5 years before the test, the mixture was 30%:70% H_2:D_2. A gas-sample was analyzed by LLNL about 2 weeks before the sweep experiment. Analysis indicated that, in storage, the mixture evolved to 23.8%:13.0%:63.2% H_2:HD:D_2. Some HD had formed during storage; however the gas is still far from the equilibrium composition, 10.1%:40.4%:49.5% H_2:HD:D_2 (which can be predicted using a mole-balance and the accepted $H_2 + D_2 \leftrightarrow 2HD$ equilibrium constant, 3.27 at 25 °C [18]).

Three sweeps at 250°C were used to condition the bed. After the sweeps, the bed was in isotope composition-equilibrium with the gas. At 25°C, the reported H/D separation factor for uranium hydride is 1.3 [16], which, for this gas mixture, implies a 36%:64% H:D isotope ratio on the bed. For this experiment, the exact ratio is unimportant; the bed and gas are known to be at isotope-equilibrium so there will be no net gas-to-particle isotope exchange.

Initial conditions were matched to the 30°C isotope exchange tests, ensuring similar flow rates. The effluent mole fractions are shown below and compared to the equilibrium H_2:HD:D_2 composition.

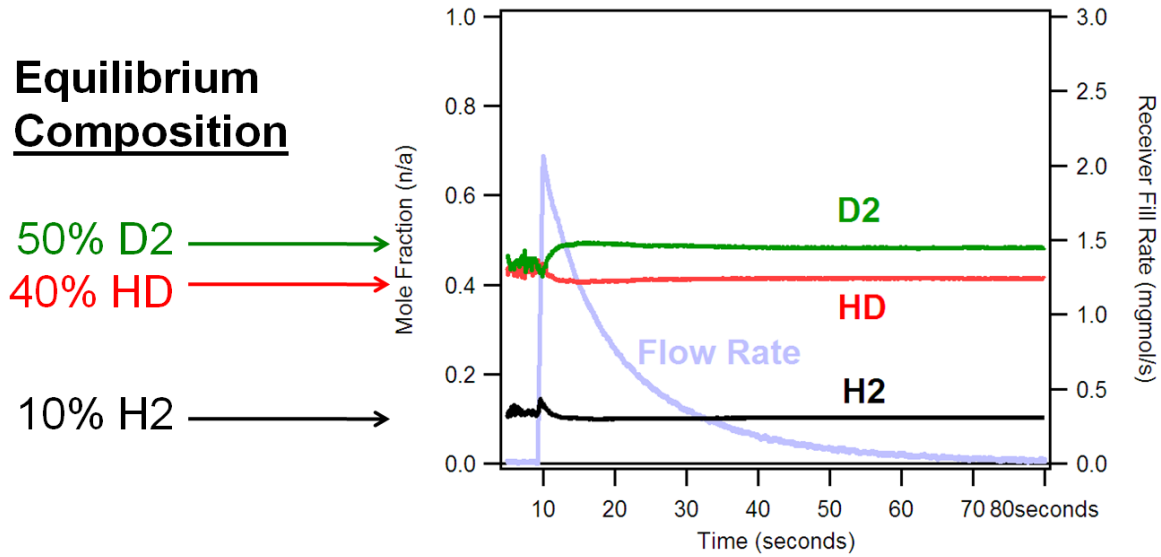

Figure 75: Effluent composition and flow rate during the mixed gas test.

It is clear that, after the sweep starts and the RGA has fully responded (t>15 s), the effluent mole fractions are steady at the predicted $H_2 + D_2 \leftrightarrow 2HD$ equilibrium values. This composition is very different than the input gas composition, 23.8%:13.0%:63.2% H_2:HD:D_2. Therefore substantial conversion of $H_2 + D_2$ to HD was achieved. This indicates, within the bed, local $H_2 + D_2 \leftrightarrow 2HD$ reaction rates are much faster than local flow rates; which therefore implies that gas phase mass transport and gas-surface exchange rates, steps 1+2, are much faster than the flow rates. Consequently, because under these conditions, the overall gas-to-particle isotope exchange rates are much slower than the flow rates, it is clear that step 3, intra-particle diffusion, limits the gas-to-particle exchange rate at 26°C.

Mixed gas sweep tests were not performed at 100 or 250°C. However, it can be shown that at 26, 100, and 250°C, and at all flow rates, the effluent gas is in $H_2 + D_2 \leftrightarrow 2HD$ composition-equilibrium. This observation strongly supports the assumption that intra-particle diffusion limits the gas-to-particle exchange rate at all temperatures between 26 and 250°C.

Having identified the rate-limiting process, the next logical steps are to:

- Confirm these results with a second reactor, including at higher temperatures.
- Simulate these experiments using a system-level exchange and transport model to identify the effective intra-particle diffusion coefficients. These diffusivities can then be compared to NMR-measured values reported in [44-45].
- Develop ways to measure and modify particle size to create conditions where solid-phase transport is more rapid.

5 SUMMARY

This report described initial studies that sought to identify the most appropriate reactant for use in a fast acting, uranium hydride based, hydrogen generation system. For reasons given in Section 2, we began our study with oxygen gas using small-scale (2.9 grams UH_3) fixed-bed reactors.

From numerical simulations and experiments, described in Sections 0 and 0 respectively, it was found that:

- UD_3 powder beds can be prepared precisely enough to make valid reactor-to-reactor comparisons. After conditioning the bed with 3 hydride/dehydride cycles, the bed has uniform density and the UD3 particles may be approximated as ~ 0.5 μm spheres.
- The UD_3+O_2 reaction is significantly faster than literature reports of the U+O_2 reaction near room temperature (30–40 °C).
- UD_3 oxidizes completely with no passivation, forming, under these experimental conditions, U_3O_8 as the major product.
- Under all conditions studied, very little water exits the reactor. Therefore, if the UD_3 + O_2 reaction produces water, it is likely a relatively short-lived intermediate species.
- As a UD_3 bed is oxidized to U_3O_8, $UD_3 \rightarrow U_3O_8$ particle expansion drastically alters the bed properties (porosity and permeability).
- Rapid oxygen injection leads to rapid local heating which, for this bed configuration, leads to local bed sintering and flow channeling.
- The UD_3+O_2 reaction is still prompt at an initial reactor temperature of −80°C; the promptness is comparable to 30°C initial temperature.

All of these findings encourage continued development of a reactive thermal decomposition system. The major challenge for this concept appears to be heat management. Each spatial point in the reactor must exceed the hydride decomposition temperature at some point in time, but not exceed the temperature at which sintering creates channels that allow reactant to bypass the bed. This may be achievable using more moderate reactant doses, dilution of reactants in inert gases, and/or the use of shaped frits or smaller aspect ratio beds that more broadly distribute the reactant gas. Each of these concepts would be worthwhile topics for future study.

In addition to oxygen injection experiments, we performed a set of hydrogen isotope exchange tests on one of the reactors. The intent of these tests was to measure uranium hydride H/D isotope exchange kinetics. The kinetic data is thought to be valuable to designers of uranium hydride based hydrogen isotope separation systems.

The experiments, described in Section 4.5 indicated that, while isotope exchange appears significantly slower in uranium hydride than in palladium hydride, the exchange kinetics are likely fast enough for isotope separation applications if the uranium hydride bed is heated to

temperatures near 250 °C. In the one reactor studied thus far, which contains ~ 0.5 μm diameter uranium hydride particles, it was found that hydrogen transport in the hydride particles is the rate limiting step in the overall gas-to-particle exchange process; for both $UD_3 + H_2$ and $UH_3 + D_2$ exchange, at temperatures between 25 and 250 °C.

The isotope exchange results need to be confirmed with additional reactors. In addition, a system-level exchange and transport model should be used to identify effective intra-particle diffusion coefficients. These findings, should they hold true, significantly advance the understanding of hydrogen isotope exchange in uranium hydride.

6 REFERENCES

1. Manchester, F. and A. San-Martin, *The H-U (Hydrogen-Uranium) System.* Journal of Phase Equilibria, 1995. **16**(3): p. 263.
2. Powell, G.L., *Reaction of Oxygen with Uranium Hydride*. Advanced Materials for Energy Conversion Ii, ed. D.B.R.G.S.L. Chandra. 2004. 249-254.
3. Epstein, M., et al., *On Prediction of the Ignition Potential of Uranium Metal and Hydride.* Nuclear Safety, 1996. **37**(1): p. 12.
4. Longhurst, G.R., et al., *Experimental Evaluation of the Consequences of Uranium Bed Air-Ingress Accidents.* Fusion Technology, 1992. **21**(2): p. 1017.
5. Le Guyadec, F., et al., *Pyrophoric Behaviour of Uranium Hydride and Uranium Powders.* Journal of Nuclear Materials, 2010. **396**(2-3): p. 294.
6. Totemeier, T.C., *Characterization of Uranium Corrosion Products Involved in a Uranium Hydride Pyrophoric Event.* Journal of Nuclear Materials, 2000. **278**(2-3): p. 301.
7. Katz, J.J. and E. Rabinowitch, *The Chemistry of Uranium: The Element, Its Binary and Related Compounds*. National Nuclear Energy Series. Manhattan Project Technical Section. Division Viii: Manhattan Project, V. 5. 1961, New York,: Dover Publications. xxi, 609 p.
8. Mueller, W.M., et al., *Metal Hydrides*. 1968, New York: Academic Press. xii, 791 p.
9. Newton, A.S., et al., *Uranium Hydride .2. Radiochemical and Chemical Properties.* Nucleonics, 1949. **4**(2): p. 17.
10. Agarwala, U., J.B. Hunt, and H. Taube, *Tracer Experiments on the Reaction of Uh3 with Aqueous Acid.* Journal of Chemical Physics, 1960. **32**(5): p. 1567.
11. Hunt, J.B. and H. Taube, *Hydrogen Tracer Studies on Reactions of Uranium Hydride with Aqueous Oxidizing Agents.* Inorganic Chemistry, 1964. **3**(10): p. 1431.
12. Ise, T., et al., *The Surface Structure and the Electrochemical Properties of Hydrogen-Absorbing Alloys Treated with an Hcl Aqueous Solution.* Journal of Alloys and Compounds, 2000. **307**: p. 324.
13. Berthet, J.C., et al., *Synthesis of the Uranium Triflates U(Otf)(3) and U(Otf)(4) - Crystal Structure of U(Otf)(2)(Opph3)(4) Otf.* European Journal of Inorganic Chemistry, 1999(11): p. 2005.
14. Condon, J.B. and E.A. Larson, *Kinetics of the Uranium-Hydrogen System.* The Journal of Chemical Physics, 1973. **59**(2): p. 855.
15. Powell, G.L., W.L. Harper, and J.R. Kirkpatrick. *The Kinetics of the Hydriding of Uranium Metal*. in *International Symp on Metal-Hydrogen Systems, Fundamentals and Applications*. 1990. Banff, Canada: Elsevier Science Sa Lausanne.
16. Imoto, S., T. Tanabe, and K. Utsunomiya, *Separation of Hydrogen Isotopes with Uranium Hydride.* International Journal of Hydrogen Energy, 1982. **7**(7): p. 597.
17. Bigeleisen, J. and A. Kant, *Low Temperature Mobility of Hydrogen in Uranium Hydride. Exchange Equilibrium of Deuterium between Hydrogen and Uranium Hydride1*. Journal of the American Chemical Society, 1954. **76**(23): p. 5957.
18. Foltz, G.W. and C.F. Melius, *Studies of Isotopic Exchange between Gaseous Hydrogen and Palladium Hydride Powder.* Journal of Catalysis, 1987. **108**(2): p. 409.
19. Swansiger, W.A., V.K. Gabrielson, and R.W. Bradshaw, *Summary Abstract: Recovery of Tritium from Tritiated Water by Reaction with Uranium*. Vol. 2. 1984: AVS. 721-722.

20. Aiello, R., J.H. Sharp, and M.A. Matthews, *Production of Hydrogen from Chemical Hydrides Via Hydrolysis with Steam.* International Journal of Hydrogen Energy, 1999. **24**(12): p. 1123.
21. Hunt, J.B. and H. Taube, *Hydrogen Tracer Studies on the Reactions of Uranium Hydride with Aqueous Oxidizing Agents.* Inorganic Chemistry, 1964. **3**(10): p. 1431.
22. Schnaars, D.D., G. Wu, and T.W. Hayton, *Reactivity of Uh(3) with Mild Oxidants.* Dalton Transactions, 2008(44): p. 6121.
23. Bach, H.T., et al. A Real-Time Mass Spectrometer for Characterization of Hydrogen Isotopic Exchange Reactions with Palladium Hydrides. LA-UR-02-2593. (2002).
24. Malinowski, M.E., K.D. Stewart, and A.A. VerBerkmoes. Fastgas: Fast Gas Sampling for Palladium Exchange Tests. SAND91-8220. Sandia National Laboratories. (1991).
25. Vafai, K., *Handbook of Porous Media*. 2005, Boca Raton, FL: Taylor & Francis.
26. Mason, E.A. and A.P. Malinauskas, *Gas Transport in Porous Media: The Dusty Gas Model*. Chemical Engineering Monographs. 1983, Amsterdam: Elsevier.
27. Lindner, D.L., *Isothermal Decomposition of Uranium Hydride.* Journal Of The Less Common Metals, 1990. **157**: p. 139.
28. Robinson, S.L. and G.J. Thomas. Uranium Hydride Formation and Properties: A Review with Commentary on Handling and Disposition. SAND96-8206. Sandia National Labs. (1996).
29. Ritchie, A.G., *A Review of the Rates of Reaction of Uranium with Oxygen and Water Vapour at Temperatures up to 300° C.* Journal of Nuclear Materials, 1981. **102**(1-2): p. 170.
30. Mills, A.F., *Mass Transfer*. 2001: Prentice-Hall. 432.
31. White, F.M., *Viscous Fluid Flow*. 2nd ed. 1991, New York, NY: McGraw-Hill.
32. Young, J.B. and B. Todd, *Modelling of Multi-Component Gas Flows in Capillaries and Porous Solids.* International Journal of Heat and Mass Transfer, 2005. **48**: p. 5338.
33. Heung, L.K., *Tritium Transport Vessel Using Depleted Uranium.* Fusion Technology, 1995. **28**(3): p. 1385.
34. Abraham, B.M. and H.E. Flotow, *The Heats of Formation of Uranium Hydride, Uranium Deuteride and Uranium Tritide at 25 C.* Journal of the American Chemical Society, 1955. **77**(6): p. 1446.
35. Bloch, J. and M.H. Mintz, *Kinetics and Mechanisms of Metal Hydrides Formation - a Review.* Journal of Alloys and Compounds, 1997. **253-254**(1-2): p. 529.
36. Shugard, A. and P.V. Blarigan. Characterization of Gas Flow in a Porous Media Compact. SAND2006-6160. Sandia National Laboratories. (2006).
37. Meyer, B.A. and D.W. Smith, *Flow through Porous Media: Comparison of Consolidated and Unconsolidated Materials.* Industrial and Engineering Chemistry, Fundamentals, 1985. **24**(3): p. 360.
38. Stakebake, J.L., *Kinetics for the Reaction of Hydrogen with Uranium Powder.* Journal of the Electrochemical Society, 1979. **126**(9): p. 1596.
39. Bloch, J., *The Hydriding Kinetics of Activated Uranium Powder under Low (near Equilibrium) Hydrogen Pressure.* Journal of Alloys and Compounds, 2003. **361**(1-2): p. 130.
40. Downs, G.L. and P.A. Tucker, *Sem Facility for Examination of Reactive and Radioactive Materials.* Microstructural Science, 1977. **5**: p. 403.
41. Downs, Tucker, and Jones. "A Review of the Mound Sem Facility for Radioactive and Pyrophoric Materials". Conference presentation. *Unpublished Studies.* Sandia National Labs. (1982).

42. McEachern, R.J. and P. Taylor, *A Review of the Oxidation of Uranium Dioxide at Temperatures Below 400°C.* Journal of Nuclear Materials, 1998. **254**(2-3): p. 87.
43. Costantino, M.S., J.F. Lakner, and R. Bastasz, *Synthesis of Monolithic Uranium Hydride and Uranium Deuteride.* Journal of the Less-Common Metals, 1990. **159**(1-2): p. 97.
44. Grunzweig-Genossar, J., M. Kuznietz, and B. Meerovici, *Nuclear Magnetic Resonance in Uranium Hydride and Deuteride.* Physical Review B, 1970. **1**(5): p. 1958.
45. Peretz, M., et al., *Nmr Study of Hydrogen Diffusion in Uranium Hydride.* Journal of Physics and Chemistry of Solids, 1976. **37**(1): p. 105.
46. Souter, P.F., et al., *Experimental and Theoretical Evidence for the Formation of Several Uranium Hydride Molecules.* Journal of the American Chemical Society, 1997. **119**(7): p. 1682.
47. Raab, J., et al., *A Combined Experimental and Theoretical Study of Uranium Polyhydrides with New Evidence for the Large Complex Uh4(H2)6.* The Journal of Physical Chemistry A, 2007. **111**(28): p. 6383.
48. Charton, S., J.P. Corriou, and D. chweich, *Modeling of Hydrogen Isotopes Separation in a Metal Hydride Bed.* Chemical Engineering Science, 1999. **54**(1): p. 103.
49. Fukada, S., et al., *A Study of Isotopic Exchange of Hydrogen and Deuterium in a Lani3al2 Hydride Bed.* Journal of Nuclear Materials, 1992. **195**(1-2): p. 191.

DISTRIBUTION

1	Los Alamos National Laboratory Attn. Brad A. Meyer P.O. Box 1663 Los Alamos, NM 87545		
1	MS0136	Marsh E. Burfeindt	00214
1	MS1415	Tina M. Nenoff	01114
1	MS0429	Stewart K. Griffiths	02100
1	MS9035	Dorian K. Balch	08224
1	MS9035	Myra Sage Dyer	08224
1	MS9035	Costanzo A. LaJeunesse	08224
1	MS9035	Benjamin Markel	08224
1	MS9025	Brian E. Oden	08224
1	MS9035	Nicholas J. Paradiso	08224
1	MS9035	Scott T. Peterson	08224
1	MS9035	Steven F. Rice	08224
1	MS9035	Ryan B. Sills	08224
1	MS9035	Paul A. Spence	08224
1	MS9035	Linh Thai	08224
1	MS9035	Donald J. Bohrer	08200
1	MS9035	Anton J. West	08200
1	MS9108	Carl W. Pretzel	08221
1	MS9153	Michael F. Hardwick	08220
1	MS9154	William P. Ballard	08200
1	MS9161	George M. Buffleben	08623
1	MS9403	Bernice E. Mills	08223
1	MS9403	Timothy J. Shepodd	08223
1	MS9404	Rion A. Causey	08222
1	MS9404	Donald F. Cowgill	08222
1	MS9404	Thomas E. Felter	08222
1	MS9404	Robert Kolasinski	08222
1	MS9404	Weifang Luo	08222
1	MS9404	Kenneth D. Stewart	08222

1	MS9404	Neville R. Moody	08651
1	MS9291	David Robinson	08651
1	MS9409	Neal R. Fornaciari	08365
1	MS9409	Patricia E. Gharagozloo	08365
1	MS9409	Scott C. James	08365
1	MS9409	Michael P. Kanouff	08365
1	MS9409	Michael T. Leick	08365
1	MS9409	Robert H. Nilson	08365
1	MS9661	Todd G. Felver	08224
1	MS9661	John S. Korellis	08224
4	MS9661	Andrew D. Shugard	08224
1	MS9661	Andrew Van Blarigan	08224
2	MS9661	Peter Van Blarigan	08224
1	MS9661	David V. Zanini	08224
2	MS9960	Technical Library – CA	08944
1	MS0899	Technical Library	09536 (electronic copy)
1	MS0123	D. Chavez, LDRD Office	01011

Sandia National Laboratories